Growth and Study of Optoelectronic Properties of a-Si:H/nc-Si:H Based Superlattice Structures

A thesis submitted

by

Asha Yadav

In partial fulfillment of the requirement for the award of the degree of Doctor of Philosophy

Centre for Energy
Indian Institute of Technology Guwahati
Guwahati-781039, Assam, India

March 2018

Growth and Study of Optoelectronic Properties of a-Si:H/nc-Si:H Based Superlattice Structures

A thesis submitted

by

Asha Yadav

Roll No: 126151002

In partial fulfillment of the requirement for the award of the degree of Doctor of Philosophy

Centre for Energy
Indian Institute of Technology Guwahati
Guwahati-781039, Assam, India

March 2018

DECLARATION

The work contained in this thesis entitled **"Growth and Study of Optoelectronic Properties of a-Si:H/nc-Si:H Based Superlattice Structures"** has been carried out by me under the supervision of Dr. Pratima Agarwal, Professor, Department of Physics, Indian Institute of Technology, Guwahati, Assam, India. This thesis does not contain any materials previously submitted for the award of any degree or diploma.

Date: 13.03.2018

Asha Yadav
Centre for Energy
Indian Institute of Technology, Guwahati
Guwahati-781039, Assam, India

भारतीय प्रौद्योगिकी संस्थान गुवाहाटी
Indian Institute of Technology Guwahati
North Guwahati, Guwahati
PIN- 781 039, Assam State, INDIA
Phone: +91 361 2583000 Extn 2702, 2582702
Fax: +91 361 2690 762 (Institute), 2582749 (Department)

Dr. Pratima Agarwal
Professor
Department of Physics
E-mail:pratima@iitg.ernet.in

Dated: March 13, 2018

Certificate

This is certified that the work contained in this thesis entitled **"Growth and Study of Optoelectronic Properties of a-Si:H/nc-Si:H based Superlattice Structures"** submitted by Ms. Asha Yadav, a Ph. D. student at Centre for Energy, Indian Institute of Technology, Guwahati, Assam, India, for the award of the degree of Doctor of Philosophy has been carried out under my supervision. This work has not been submitted elsewhere for the award of any degree or diploma.

(Dr. Pratima Agarwal)

Dedicated

to

My Parents and My Supervisor

Acknowledgements

I am extremely grateful to my thesis supervisor, Prof. Pratima Agarwal, for her continuous support and guidance throughout my Ph.D work. She taught me a lot on how to approach research problems, how to analyze and understand the results from physicist's perspectives. I am very thankful to her for giving me opportunity to work under her supervision and will remain ever grateful to her.

I am grateful to my doctoral committee members Prof. Alika Khare (Chairperson), Prof. Vimal Katiyar and Prof. Gaurav Trivedi for reviewing my research work regularly and giving valuable suggestions. I extend my sincere gratitude to our earlier Head of Centre for Energy, Prof. P. Goswami and the current Head of Centre for Energy, Prof. V.S. Maholkar, Head of Department of Physics, Prof. P. Poulose as well as all the faculty members of Centre for Energy and Department of Physics for their support. I am also grateful to Prof. S.C. Agarwal, visiting faculty in Department of Physics, for the valuable discussion.

I would like to acknowledge my seniors Dr. Himanshu S. Jha, Dr. Mukesh Singh, Dr. Lalhriatzuala past lab mate Mr. Suman Sarkar and my current lab mates Mr. Ramakrishna Madka, Mr. Venkanna Kannaboina, Mr. Pilik Basumatary, Mr. Manvendra Singh Gangwar, Ms. Juhi Kumari, Ms. Jaishree Bharadwaj, Ms. Shubhangi Bharadwaj, Mr. Vivek Ghrithahre and Ms. Niharika Gogoi for providing an amicable ambience for research in the lab as well as for their help during my research work. I would also like to thank the project students Mr. Bholuram Swami, Mr Adesh Kumar, Mr Jaideep Gupta, Mr. Jitendra Kumar,

Mr Gaurav Singh, Mr. Bhagwat Chauhan and Mr. Rakesh Prasad for their help in different stage of my thesis work.

I would like to express my sincere thanks to all the staff members of Centre for Energy including Dr. Lipakshi Barbora, Mr. Debarshi Baruah, Mr. Dhiren Huzuri and Mr. Paragjyoti Sharma and also the staff members of Department of Physics including Dr. Sidananda Sharma, Mr. Lokesh Chakraborty, Ms. Minakshi chutia, Mr. Atul Deka, Mr. Hemanta Medhi and Mr. Basab B. Purakayastha for their support and cooperation during my research work. I would like to acknowledge CIF, IIT Guwahati for providing me the necessary characterization facilities during my research work. I am also thankful to the technical staff of CIF, IIT Guwahati Mr. Chandan Borgohain, Dr. K.K. Senapati, Mr. Madhurjya Borah and Mr. Kesho Singh.

I am also thankful to all the research scholar of Centre for Energy and Department of Physics for their help and support during my research work.

I am thankful to all my friends Dr. Satchi Kumari, Dr. Indrajeet Kumar, Dr. Nisha Shankhwar, Dr. Onkar Verma, Ms. E. Mal, Mr. R. Kesarwani, Mr. G. Pradhan, Mr P.Kr. Baruah, Dr. P.P Dey, Mr. G.P. Bharti, Mr. R. Kumar, Ms. S. Behera, Ms. S. Kaushik, Mr. J. Kumar, Mr. A. Kumar and other friends for their support and encouragement.

I am grateful to BRFST, IPR and CSIR, New Delhi, India for the financial support during my thesis work.

Last but not the least, I would like to thank my sister, brother, my little nephews (Shourya and Yash) and my parents for their never-ending love and support.

Asha Yadav

IIT Guwahati, India, March 2018

Preface

Hydrogenated a-Si is an extensively studied material for the fabrication of number of optoelectronic devices like solar cells, thin film transistors etc. The optoelectronic properties of the material is controlled by the disorder and defects induced states in the energy gap between the valence band and conduction band which arise due to inherent disorder and over constrained four fold coordinated tetrahedral network. The addition of hydrogen not only relaxes the over constrained tetrahedral network but also passivates the defects state making the material suitable for large area device applications. In recent years, hydrogenated nc-Si has also been the subject of scientific and technological interest because of its outstanding properties such as tunable band gap, higher carrier mobility, higher doping efficiency and higher stability against light induced degradation. By modifying the c-Si environment, it is hoped to induce a more efficient luminescence than is found in indirect gap bulk c-Si and also shift in emission energy from 1.1 eV into the visible region. For this purpose, the precise control of Si nanocrystals size is required since the band gap of a quantum dot is mainly determined by its dimension. Various methods have been employed to produce ultra-fine silicon nanocrystals such as rf-PECVD, laser ablation, rf-magnetron sputtering, microwave CVD, gas phase synthesis etc. Another pathway for synthesis of Si nanocrystals with controlled size and density is the fabrication of multilayer structures of amorphous silicon oxide (a-SiO)/SiO_2 superlattice, nanocrystalline-Si (nc-Si)/SiO_2, Si/SiO_2 with varying stoichiometry followed by subsequent processing. In a-Si/SiO_2 superlattice structures, researchers have succeded in recrystallization of a-Si by annealing it at very high

temperature in ambient environment in order to passivate the dangling bonds. However, SiO_2 is generally not considered to be a good candidate for device application due to its large band offset with respect to silicon. A superlattice structure with lower band offset such as a-Si:H/nc-Si:H is desirable to increase carrier mobility. The a-Si:H/nc-Si:H superlattice structures show many interesting properties such as low thermal conductivity, enhanced carrier mobility and photo conductivity, visible photoluminescence etc. Superlattice structures based on amorphous layers have also been proposed as novel transistors, in which a superlattice of alternating low and high-band gap layers comprises the channel region between the source and drain of thin film transistors. Though a-Si:H/nc-Si:H superlattice structures show many interesting properties which make this material a good candidate for device applications, the main challenge in multilayer/superlattice structures based electronic devices is the interface states between the sublayer which may act as recombination centers thereby controlling the transport mechanism and overall performanance of the devices. Therefore, proper knowledge of these states is very important for device fabrication.

The present thesis focuses on the study of the interface states in a-Si:H/nc-Si:H superlattice structures, which play an important role in tunning the optoelectronic properties of these structures. In addition these superlattice structures may also be used for the growth of silicon nanocrystallities in a-Si:H matrix with tunable optoelectronic properties and visible photoluminescence by controlling the thickness of nc-Si layer sandwiched between the a-Si:H layers. The a-Si:H/nc-Si:H superlattice structures were prepared using both HWCVD and rf-PECVD techniques. For the thin individual layers of a-Si:H and nc-Si:H thin films, rf-PECVD technique has been used whereas, for the thick films HWCVD technique has been used. As the motivation of the work was on the study of interface states in a-Si:H/nc-

Si:H superlattice structures, therefore, at first the optimization of deposition parameters for the fabrication of device quality a-Si:H, nc-Si:H using both HWCVD and rf-PECVD techniques has been conducted and subsequently from the optimized deposition parameters a-Si:H/nc-Si:H superlattice structures were fabricated. These films were studied using various characterization techniques such as X-ray Diffraction (XRD), Raman scattering spectroscopy, Transmission Electron Microscope (TEM), Photoluminescence, Field Emission Scanning Electron Microscope (FESEM), Ultraviolet visible near infrared (UV-Vis-NIR) spectroscopy and *IV* measurements.

Numbers of such superlattice structures were fabricated with the variation in layer thickness and number of periods. The electrical transport properties of these structures were performed in both coplanar as well as transverse geometry, as the electrical transport in these structure is anisotropic. Quite interestingly, room temperature persistent photoconductivity (PPC) has been observed in these a-Si:H/nc-Si:H superlattice structures in coplaner geometry. PPC decay time constant, its dependence on exposure time, applied electric field, number of periods and annealing temperature have been studied in detail. Whereas, transverse geometry has been used to estimate the density of localised states in single layer as well as superlattice structures of a-Si:H and nc-Si:H thin films using space charge current limited (SCLC) measurements. Fabrication of these superlattice structures also help us to grow a controlled size of Si nanocrystal in amorphous matrix. Number of such structures were prepared with the variation in nc-Si layer thickness while keeping a-Si:H layer thickness constant. These superlattice strcutures with thin nc-Si layers (5-30 nm) exhibited room temperature visible photoluminescence without any post deposition processing. The peak position in PL was found to depend upon the thickness of nc-Si layer suggesting the

quantum size effects. The nc-Si/a-Si:H superlattice structures propose a unique pathway for synthsizing Siliocn nanocrystals with controlled size and photonic signature.

The present thesis is divided into eight chapters. Chapter 1 presents a brief introduction of content along with literature review on work reported in the thesis. The motivation and aim of the thesis work are also included in this chapter. Chapter 2 gives the quick review on the description of both rf-PECVD and HWCVD techniques with the details of deposition parameters used for the fabrication of the films. It also contains a brief discussion on the different characterization techniques used for the study of structural, optical and electronic properties of these films. Chapter 3 contains the detail studies of the influence of deposition parameters on the structural and optoelectronics properties of silicon thin films prepared using both HWCVD and rf-PECVD technique. Chapter 4 presents studies on laser induced selective crystallization of a-Si:H thin films using Raman spectroscopy. Chapter 5 presents the studies on persistent photoconductivity (PPC), PPC decay time constant, its dependence on exposure time, electric field, number of periods and annealing temperature. Chapter 6 presents the detail studies on the density of states (DOS) in single layer a-Si:H and nc-Si:H as well as the superlattice structures of a-Si:H and nc-Si:H thin films using SCLC measurements in transverse geometry. Chapter 7 presents a systematic study on visible photoluminescence at room temperature in a-Si:H/nc-Si:H superlattice structures without any post deposition processing. Finally, chapter 8 summarizes the results and presents the future scope of the work.

LIST OF ABBREVIATIONS AND SYMBOLS

a-Si:H	Hydrogenated amorphous silicon
nc-Si:H	Hydrogenated nanocrystalline silicon
HWCVD	Hot wire chemical vapor deposition
rf-PECVD	radio frequency-plasma enhanced chemical vapor deposition
DC-PECVD	Direct current- plasma enhanced chemical vapor deposition
Cat-CVD	Catalytic chemical vapor deposition
CRN	Continuous random network
DOS	Density of states
ITO	Indium tin oxide
c-Si	Crystalline Si
SiC	Silicon Carbide
UV-Vis-NIR	Ultraviolet-visible-near infrared
FESEM	Field emission scanning electron microscopy
XRD	X-ray diffraction
TEM	Transmission electron microscopy
HRTEM	High resolution transmission electron microscopy
SAED	Selected area electron diffraction
PL	Photoluminescence
FWHM	Full width at half maxima
DPSS	Diode pumped solid state
PPC	Persistent photoconductivity
SCLC	Space charge limited current
T_s	Substrate temperature
P.P	Process pressure
t_d	Deposition time
r_d	Deposition rate
t	Thickness

SFR	Silane flow rate
HFR	Hydrogen flow rate
sccm	Standard cubic centimeter per minute
[R]	Hydrogen dilution of Silane
RT	Room temperature
CuK$_\alpha$	Copper K$_\alpha$ radiation
He:Ne	Helium Neon
~	Approximately
θ	Bragg's angle
X_{nc}	Nanocrystalline volume fraction
X_c	Total crystalline volume fraction
TO	Transverse optic
σ_{ph}	Photo conductivity
σ_d	Dark conductivity
I	Current
V	Voltage
E_a	Activation Energy
T	Temperature
K_B	Boltzmann's constant.
℃	Degree Celsius
K	Kelvin
eV	Electron volt
μ	Micro
$\mathring{A}$	Angstrom
τ	Decay time constant
I_{dark}	Dark current
I_{photo}	Photo current
E_{fn}	Fermi energy
ε_s	Semiconductor permittivity
q	Electronic charge
$g(E)$	DOS distribution

E_g	Bandgap
α	Absorption coefficient
v	Frequency
λ	Wavelength
h	Plank's constant

CONTENTS

Declaration *iii*

Certificate *v*

Acknowledgements *ix*

Preface *xi*

List of abbreviations and symbols *xv*

List of Figures *xxiii*

List of Tables *xxix*

1. Introduction **1**

1.1 Structural and optoelectronic properties of hydrogenated amorphous silicon (a-Si:H) and nanocrystalline silicon (nc-Si:H) and a-Si:H/nc-Si:H superlattice structures 2

1.2 Method of preparation of a-Si:H and nc-Si:H thin films and a-Si:H/nc-Si:H superlattice structures 9

1.3 Motivations 13

1.4 Contents of Thesis Chapters 14

1.5 References 16

2. Experimental Details **31**

2.1 Preparation of Si thin films 32

2.1.1 Description of Hot Wire Chemical Vapor Deposition (HWCVD) technique 32

2.1.2 Description of rf-Plasma Enhanced Chemical Vapor Deposition (rf-PECVD) technique 34

2.1.3 Preparation of a-Si:H and nc-Si:H thin films using both HWCVD and rf-PECVD techniques 37

2.1.4 Preparation of a-Si:H/nc-Si:H superlattice structures using both 39

HWCVD and rf-PECVD techniques
2.2 Characterizations techniques 42
2.2.1 X-ray diffraction (XRD) 42
2.2.2 Raman Spectroscopy 43
2.2.3 Transmission electron microscopy 45
2.2.4 Field emission scanning electron microscopy 45
2.2.5 Stylus profilometer 46
2.2.6 UV-Vis NIR transmission Spectroscopy 46
2.2.7 Photoluminescence 47
2.2.8 Electrical transport measurements 47
2.3 References 50

3. Structural and optoelectronic properties of a-Si:H and nc-Si:H thin films prepared by HWCVD and rf-PECVD Techniques 55
3.1 Measurement Details 56
3.2 The effect of variation of H_2 dilution of SiH_4 on silicon thin films prepared using HWCVD technique (Series I) 57
3.2.1 Structural properties 57
3.2.1.1 X-ray Diffraction 57
3.2.1.2 Raman Spectroscopy 57
3.2.1.3 Transmission Electron Microscopy 59
3.2.1.4 Field Emission Scanning Electron Microscopy 60
3.2.2 Optical properties 61
3.2.3 Electrical properties 62
3.3 The effect of variation of rf-power on silicon thin films prepared using rf-PECVD technique (Series II) 64
3.3.1 Structural properties 64
3.3.1.1 X-ray Diffraction 64
3.3.1.2 Raman Spectroscopy 65
3.3.2 Optical properties 65
3.3.3 Electrical properties 66
3.4 The effect of variation of hydrogen dilution of SiH_4 on silicon thin films prepared using rf-PECVD technique (Series III) 67
3.4.1 Structural properties 68

3.4.1.1 X-ray Diffraction 68
3.4.1.2 Raman Spectroscopy 68
3.4.2 Optical properties 69
3.4.3 Electrical properties 70
3.5 The effect of variation of substrate temperature on silicon thin films prepared using rf-PECVD technique (Series IV) 71
3.5.1 Structural properties 71
3.5.1.1 X-ray Diffraction 71
3.5.1.2 Raman Spectroscopy 72
3.5.1.3 Field Emission Electron Microscopy 74
3.5.2 Optical properties 74
3.5.3 Electrical properties 76
3.6 Conclusion 77
3.7 References 78

4. Laser Induced Selective Crystallization of Amorphous Silicon Thin Film for Device Applications 83
4.1 Measurement Details 84
4.2 Results and Discussion 84
4.3 Conclusion 94
4.4 References 95

5. Persistent Photoconductivity studies in a-Si:H/nc-Si:H superlattice structures 99
5.1 Measurement Details 100
5.2 Results and Discussion 102
5.2.1 PPC studies on thick individual layer of a-Si:H and nc-Si:H in a-Si:H/nc-Si:H superlattice structures prepared by HWCVD technique 102
5.2.2 PPC studies on thin individual layer of a-Si:H and nc-Si:H in a-Si:H/nc-Si:H superlattice structures prepared by rf-PECVD technique 109
5.3 Conclusion 111
5.4 References 113

6. Density of states measurement in a-Si:H/nc-Si:H superlattice structures **117**
6.1 Measurement Details 119
6.2 Theory 120
6.3 Results and Discussion 121
6.4 Conclusion 126
6.5 References 128

7. Tunable visible photoluminescence in a-Si:H/nc-Si:H superlattices **133**
7.1 Measurement Details 134
7.2 Results and Discussion 136
7.3 Conclusion 146
7.4 References 147

8. Summary, Conclusion and Future Scope **153**
8.1 Scope for Future work 156

List of Publications **157**

LIST OF FIGURES

1.1	Continuous random network (CRN) allowing the constituent atoms to retain their coordination numbers	5
1.2	Density of states picture for a-Si:H	6
1.3	Schematic of the dissociation processes of SiH_4 and H_2 molecules under the influence of high rf-field	10
1.4	Number density of different film forming radicals in steady state plasma	10
2.1	Schematic diagram of a general HWCVD system.	33
2.2	a) HWCVD system with gas manifold in our lab and b) HWCVD chamber during deposition	34
2.3	Schematic diagram of a general PECVD system	35
2.4	rf-PECVD system in our lab (inset image: rf-PECVD chamber during deposition)	36
2.5	Schematic of the dissociation processes of SiH_4 and H_2 molecules under the influence of high rf-field	37
2.6	Number density of different film forming radicals in steady state plasma	37
2.7	Deconvoluted Raman spectra of Si thin film	44
2.8	Schematic diagram of a-Si:H/nc-Si:H superlattice structure and electrode geometry	49
2.9	Schematic of the electrode geometry used to perform SCLC measurements in a-Si:H/nc-Si:H superlattice structures	49
3.1	The X-ray diffraction pattern of Si thin films prepared at different H_2 dilution of silane	57
3.2	Raman scattering spectra of Si thin films at different H_2 dilution of silane	58

3.3	Deconvoluted Raman spectra of nc-Si:H prepared at (a) [R]= 38% and (b) [R]= 85% H_2 dilution.	59
3.4	SAD pattern of (a) a-Si:H ([R]: 27%) and (b) nc-Si:H ([R]: 85%) thin films	60
3.5	FESEM images of Si thin films at different [R] (a) 23%, (b) 27%, (c) 38% and (d) 85%.	60
3.6	UV-Vis-NIR transmission spectra for the Si thin films prepared at different [R]	61
3.7	$\sqrt{\alpha h\nu}$ vs $h\nu$ curve for Si film prepared at [R]=85%	62
3.8	Dark and photo conductivity of the Si thin films at different [R]	63
3.9	XRD pattern of Si thin films prepared at different rf-power	64
3.10	Raman spectra of Si thin films prepared at different rf power	65
3.11	UV-Vis-NIR transmission spectra of the Si thin films prepared at different rf-power	66
3.12	Dark and photo conductivity of Si thin films prepared at different rf-power	67
3.13	XRD pattern of silicon films prepared at different H_2 dilution	68
3.14	Raman spectra of silicon films prepared at different H_2 dilution	69
3.15	UV-Vis-NIR transmission spectra of the Si thin films prepared at different H_2 dilution	69
3.16	Dark and photo conductivity of Si thin films prepared at different Hydrogen dilution	70
3.17	XRD pattern of silicon thin films prepared at different substrate temperature	72
3.18	Raman spectra of the silicon thin films prepared at different substrate temperature	73
3.19	De-convoluted Raman spectra of silicon thin films prepared at substrate temperature (a) 150 ºC (b) 200 ºC (c) 250 ºC	73
3.20	FESEM images of Si thin films at different deposition parameters a) 40W (Series II) b) 62% (Series III), c) 250° C (Series IV)	74

3.21 UV-Vis-NIR transmission spectra of the Si thin films prepared at different substrate temperature 75

3.22 The Dark and Photo conductivity of silicon thin films prepared at different substrate temperature 76

4.1 (a) Raman spectra at different Laser power density ([R]=50%), (b) Deconvoluted Raman spectra of the film after irradiation with laser power density 222 kW/cm^2 85

4.2 (a) Raman spectra at different Laser power density for the film prepared at ([R]=62%), (b) De-convoluted Raman spectra of the film after irradiation with laser power density 222 kW/cm^2 85

4.3 (a) Raman spectra at different Laser power density for the film prepared at [R]=94%, (b) De-convoluted Raman spectra of the film after irradiation with laser power density 222 kW/cm^2 85

4.4 Variation of a) X_c(%) and b) X_{nc}(%) as a function of laser power density (488 nm laser source) for the films prepared at different [R] 86

4.5 (a) Raman spectra at different laser power density (rf power=20W), (b) De-convoluted Raman spectra of the film after irradiation with laser power density 222 kW/cm^2 87

4.6 (a) Raman spectra at different laser power density (rf power=40W), (b) De-convoluted Raman spectra of the film after irradiation with laser power density 222 kW/cm^2 88

4.7 (a) Raman spectra at different laser power density (rf power=60W), (b) De-convoluted Raman spectra of the film after irradiation with laser power density 222 kW/cm^2 88

4.8 Variation of a) X_c (%) and b) X_{nc} (%) as a function of laser power density (488 nm laser source) for the film prepared at different rf-power 89

4.9 Raman spectra at different H_2 dilution a) 50 %, b) 62 %, c) 94 % and at different laser power density 90

4.10 De-convoluted Raman spectra of the film (at [R]=50%) after irradiation with laser power density a) 343 kW/cm^2 and b) 687 kW/cm^2 90

4.11 De-convoluted Raman spectra of the film (at [R]=62%) after irradiation with laser power density a) 343 kW/cm^2 and b) 687 kW/cm^2 91

4.12 De-convoluted Raman spectra of the film (at [R]=94%) after irradiation with laser power density a) 343 kW/cm^2 and b) 687 kW/cm^2 91

4.13 Variation of a) X_c (%) and b) X_{nc} (%) as a function of laser power density (632.8 nm laser source) for the films prepared at [R] 91

4.14 Variation of X_c(%) as a function of laser power density using two different laser source (488 nm and 632.8 nm) for the film prepared at different [R]; a) 50%, b) 62% and c) 94%. 92

5.1 Schematic diagram of a-Si:H/nc-Si:H superlattice structure and electrode geometry 101

5.2 Rise and decay of photo conductivity of (a) single layer a-Si:H, nc-Si:H thin films and rise and decay of photo current of (b) 5 periods of a-Si:H/nc-Si:H superlattice 103

5.3 Rise and decay of photo current of 5 periods of superlattice structure annealed at (a) 70℃ and (b) 120℃ measured at RT 103

5.4 a) Rise and decay of the photo current with the variation of external applied field, b)Variation of PPC (%) and photo current with the change of external applied field in 5 periods superlattice structures 105

5.5 Schematic band diagram of a-Si:H/nc-Si:H superlattice structure 107

5.6 Direction of current under the applied external field in the superlattice structure 107

5.7 Rise and decay of photo current of 2 periods superlattice structures of individual layer thickness of (a) 175 nm each and (b) 70 nm each 108

5.8 Rise and decay of the photo current across single layer of a-Si:H and nc-Si:H thin films 109

5.9 Rise and decay of the photo current in a-Si:H/nc-Si:H superlattice with nc-Si:H layer thickness of (a) 5 nm, 10 nm, 20 nm (7 layers) and (b) 30 nm (7 layers) and 20 nm (11 layers) structures 110

6.1 Schematic of the electrode geometry used to perform SCLC measurements in a-Si:H/nc-Si:H superlattice structures 120

6.2 I-V across single layer (a) a-Si:H and (b) nc-Si:H in sandwich geometry 122

6.3	I-V across total a-Si:H/nc-Si:H (a) 2 periods and (b) 5 periods superlattice structures in sandwich geometry	122
6.4	I-V across (a) single layer a-Si:H film, (b) 2 periods and (c) 5 periods superlattice structures (across single pair of a-Si:H/nc-Si:H)	123
6.5	(a) Variation of DOS and (b) ΔV verse ΔE_f across single, 2 periods and 5 periods superlattice structures (across single pair of a-Si:H/nc-Si:H)	124
6.6	Schematic band diagram of Ag/nc-Si:H/a-Si:H/ITO superlattice structure. The value of bandgap and activation energies are obtained from transmission spectroscopy and conductivity measurements respectively. The electron affinity of Si is taken as 4.05eV	126
7.1	Schematic of a-Si:H/nc-Si:H superlattice structures (the thickness of nc-Si:H layer was varied in different samples)	135
7.2	The XRD pattern of single layer a-Si:H and nc-Si:H thin films with different [R]	137
7.3	(a) Raman spectra of single layer a-Si:H and nc-Si:H thin films with different [R], (b) Deconvoluted Raman spectra of single layer of nc-Si:H prepared at [R]=96%	137
7.4	SAD pattern of (a) a-Si:H and (b) nc-Si:H single layer thin films	138
7.5	PL spectra of a-Si:H/nc-Si:H superlattice structures on (a) Silicon and (b) glass substrates	138
7.6	PL spectra of single layer a-Si:H and nc-Si:H thin films on silicon substrate and blank Si substrate.	139
7.7	The de-convoluted PL spectra of superlattice structure films (nc-Si:H layer thickness of 5 nm) with peak position on (a) Si and (b) glass substrates	140
7.8	The de-convoluted PL spectra of superlattice structure films (nc-Si:H layer thickness of 10 nm) with peak position on (a) Si and (b) glass substrates	140
7.9	The de-convoluted PL spectra of superlattice structure films (nc-Si:H layer thickness of 20 nm) with peak position on (a) Si and (b) glass substrates	141
7.10	The deconvoluted PL spectra of superlattice structure films (nc-Si:H layer	141

thickness of 30 nm) with peak position on (a) Si and (b) glass substrates

7.11 PL peak position λ *Vs* d^2 on silicon and corning glass substrate 144

7.12 UV-Vis-NIR transmission spectra of single layer a-Si:H and nc-Si:H thin films 144

7.13 Rise and decay of the photo current in a-Si:H/nc-Si:H superlattice with nc-Si:H layer thickness of 30 nm (7 layers) and 20 nm (11 layers) structures 145

LIST OF TABLES

2.1	Deposition parameters of a-Si:H and nc-Si:H thin films prepared using HWCVD technique. (P.P is process pressure, SFR (sccm) and HFR (sccm) refer to silane and hydrogen flow rates in standard cubic centimeter per min) (Series I)	38
2.2	Deposition parameters for silicon thin films prepared with the variation of rf-power using rf-PECVD technique (Series II)	39
2.3	Deposition parameters for silicon thin films prepared with variation of H_2 dilution of silane using rf-PECVD technique (Series III)	39
2.4	Deposition parameters for silicon thin films prepared with variation of T_s using rf-PECVD technique (Series IV)	39
2.5	Thickness of individual layer in a-Si:H/nc-Si:H superlattice structures	40
2.6	Deposition parameters of single layer of a-Si:H and nc-Si:H thin films prepared using rf-PECVD technique	41
2.7	Deposition parameters of a-Si:H/nc-Si:H superlattice structures thin films using rf-PECVD technique	42
3.1	Variation of X_{nc}(%) and X_c(%) with the variation of Hydrogen dilution of Silane	59
3.2	Thickness, deposition rate (r_d) and optical band gap (E_g) for the films as estimated from UV-Vis-NIR transmission spectra along with the films thickness (t) measured using surface profilometer	62
3.3	Thickness, deposition rate (r_d) and optical band gap (E_g) for the films as estimated from UV-Vis-NIR transmission spectra along with the films thickness (t) measured using surface profilometer.	66
3.4	Thickness, deposition rate (r_d) and optical band gap (E_g) for the films as estimated from UV-Vis-NIR transmission spectra along with the films thickness (t) measured using surface profilometer.	70
3.5	Variation of X_{nc}(%) and X_c(%) with the variation in substrate temperature	74

3.6 Thickness, deposition rate (r_d) and optical band gap (E_g) for the films as estimated from UV-Vis-NIR transmission spectra along with the films thickness (t) measured using surface profilometer. 75

5.1 The values of dark current, photo current, PPC and the decay time constant of the thick individual superlattice structures prepared by HWCVD technique 104

5.2 The values of dark current, photo current, PPC and the decay time constant of the thin superlattice structures prepared by rf-PECVD technique 110

7.1 The PL peak position, FWHM and peak intensity of superlattice structures on glass and Si substrates 142

Chapter 1

Introduction

The research on amorphous and nanocrystalline materials has grown over the last 30-40 years to be one of the most active areas in solid state physics. In this field, silicon has been a model material as it can be modified from its purest crystalline state via a two phase microcrystalline or nanocrystalline state to an almost perfectly disordered amorphous state. The technological potential of each form of thin film silicon is tremendous; however, the electronic properties suitable for making devices can be preserved in case of amorphous silicon by incorporating hydrogen into the network with appropriate concentration. Hydrogenated amorphous (a-Si:H) and nanocrystalline (nc-Si:H) silicon are the two allotropes of silicon which show much more potential for the fabrication of large area thin films based solar cells and other optoelectronic devices like thin film transistors, memories, silicon based light emitting structures for display units etc. [1-14]. The disorder in a-Si material, which may results in defects that act as recombination centers impending the transport properties of the photo generated carriers, is the major drawback of a-Si:H thin films [15-19]. In the recent years, nc-Si:H thin films have attracted considerable attention due to the superior electronic properties as compared to a-Si:H along with better stability [20-26]. Different deposition techniques were evaluated in the past for the growth of a-Si:H

and nc-Si:H thin films such as plasma spray [27], thermal spray [28], ion-beam-assisted sputtering[29], surface wave plasma source [30], high density microwave plasma [31-34], photo chemical vapor deposition [35], sputtering [36, 37], expending thermal plasma deposition[38], very high frequency PECVD [39-43], Remote plasma CVD [44-46], DC PECVD [47], electron cyclotron resonance [48-51] and rf-plasma enhanced chemical vapor (rf-PECVD) deposition [52-56], hot wire chemical vapor deposition (HWCVD) [57-62] etc. Among these techniques, HWCVD and rf-PECVD techniques have a number of advantages as compared to other techniques like large area depositions, high deposition rate and less defective films are prepared using these techniques. A new class of materials prepared by depositing alternate layer of thin films of amorphous and nanocrystalline silicon that is, the superlattice/multilayer structures of a-Si:H/nc-Si:H show many interesting features such as enhanced photosensitivity and higher carrier mobility etc [63, 64]. An interesting feature of a-Si:H/nc-Si:H superlattice structures is that with the change in the layer thickness or the number of periods in these superlattice structures, the optoelectronic properties of this structure can be easily tuned. In this introductory chapter, the material properties of hydrogenated amorphous (a-Si:H), nanocrystalline (nc-Si:H) silicon, potential applications, methods of preparation of single layer films and a-Si:H/nc-Si:H superlattice structures, motivation behind the present work and the outline of present thesis are discussed.

1.1 Structural and optoelectronic properties of hydrogenated amorphous silicon (a-Si:H) and nanocrystalline silicon (nc-Si:H) and a-Si:H/nc-Si:H superlattice structures

Sterling and Swann were the first to publish, in 1965 [65], the formation of amorphous silicon films from SiH_4 in a rf-glow discharge; the amorphous silicon film showed a very high resistivity. Using the same technique, Chittick et. al. also deposited amorphous silicon

with the variation in substrate temperature from 25℃-650℃ [66]. These films were also highly resistive ~10^{14} Ωcm with a better photoconductivity as compared to films prepared by sputtering and evaporation [67]. In fact, they were the first group which reported about possibility of doping amorphous silicon. Efforts to chemically dope the pure silicon prepared by evaporation or sputtering had not been successful because the starting materials had too many defects states. The extensive work by Spear and Le-comber on the optical and electrical properties and the distribution of localized density of states had proven that amorphous silicon prepared by PECVD can be doped with phosphine (PH_3) and biborane (B_2H_6) in order to get n-type and p-type doped amorphous silicon [68, 69]. They had also found that the room temperature conductivity could be changed by ten orders of magnitude with doping and further they were able to fabricate the p-n junction with quite good rectification characteristics. Further in the year 1976, W. Paul et al. had reported the doping of amorphous silicon by rf-sputtering using PH_3 and B_2H_6 but they also had to incorporate hydrogen in order to remove the pseudo-gap defect states [70]. The p-n junction fabricated using a-Si:H showed a very good rectification characteristic which suggested the further evaluation of this material for semiconducting devices like solar cells where the cost as well as the performance is very important. In the same year 1976, Carlson and Wronski had achieved similar doping effect and fabricated p-i-n structure based solar cell with the best power conversion efficiency of 2.4% in AM-1 sunlight using glow discharge technique [71]. Until that time, it was generally thought that amorphous silicon could not be doped, as all impurity atoms would be incorporated according to their natural coordination number. In fact, it was quite challenging to explain that amorphous silicon, without translational symmetry or Brillouin zones, could be doped at all.

The incorporation of hydrogen into the tetrahedrally coordinated amorphous semiconductors during their growth by sputtering had shown a dramatic difference in the properties from those of the un-hydrogenated materials. In 1974, Lewis et.al had shown that the addition of hydrogen in amorphous Si reduced the dangling bonds and electronic defect states; it also resulted in reduction of strain in the network and thus making the materials less defective [72]. The localized density of states has decreased from 10^{19} $eV^{-1}cm^{-3}$ to 10^{17} $eV^{-1}cm^{-3}$ with the addition of H_2 in this disordered amorphous semiconductor materials. The photovoltaic conversion efficiency of amorphous silicon had also increased from 2.4% to 6.2% with the addition of H_2 in SiH_4, prepared by glow discharge [73]. Hydrogen was now regarded as essential part of amorphous silicon and research turned from amorphous silicon to hydrogenated amorphous silicon (a-Si:H). The great advantages of hydrogenated amorphous silicon are: a) excellent photoconductivity b) wide spectral photo sensitivity, c) high absorption coefficient d) high electrical resistivity, e) low localized density of states, f) strong optical absorption and g) ability to control the electrical properties. The fact that amorphous silicon could be doped made this material a potential area of research from both physics as well as technological point of view.

The lack of periodicity in the atomic structure in amorphous semiconductor unlike that of crystalline materials is basically responsible for making these materials different from the later in many aspects. However, the presence of disorder in these materials does not mean that these are completely order-less. There exists short range order up to few atomic distances, which eventually fades away with large atomic distances. Short range order and long range disorder have made these materials similar to crystalline material in some aspects while different in some others. The structure of amorphous semiconductors with presence of

short range order and absence of long range order can be modeled by Continuous Random Network (CRN), originally proposed by Zachariasen in 1932 for glasses like silica [74]. In the CRN, one uses the coordination defects when an atom has too few or too many bonds. In this model, as shown in Fig 1.1, each atom has a number of bonds in immediate neighbors, this number is called coordination numbers. The atomic coordination number is given by Mott 8-N rule [75]. The CRN offer the flexibility to incorporate atoms of different coordination numbers. In the ideal CRN model for amorphous silicon each atoms is fourfold coordinated with the bond length similar to that in the crystals. Amorphous silicon lacks the long range order because the bond angle deviates from the tetrahedral value. The average bond angle variation reflects the degree of structural disorder in the random network. The variation in bond length and bond angle leads to the broadening of electronic distribution of states and carriers, electron and hole, localization along with the strong scattering of the carriers. Therefore, a-Si/a-Si:H do not possess a clean band gap as c-Si.

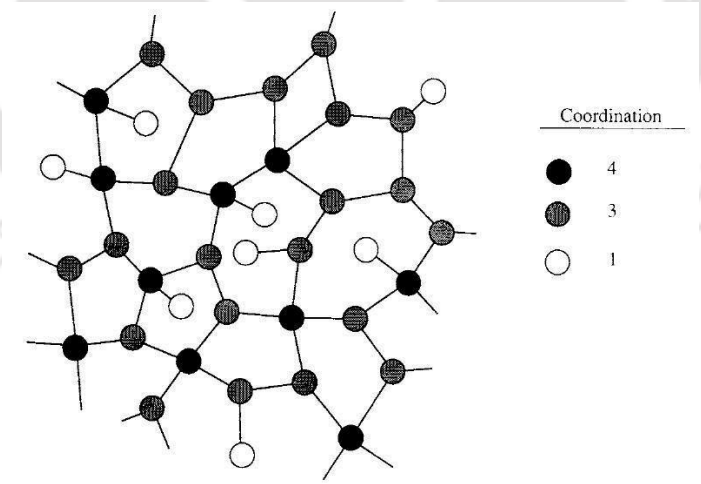

Figure 1.1: Continuous random network (CRN) allowing the constituent atoms to retain their coordination numbers [76].

The information of concentration and distribution of charge carriers in a semiconductor is provided by the energy distribution of states, known as density of state (DOS). In ideal

silicon crystal, the conduction band and the valence band are separated by well-defined band gap (E_g) and no energy states are allowed in the gap. However, in case of a-Si:H, the lack of long range order manifests in the form of band tails along with the coordination defects in the mid gap region as shown in Fig 1.2 The energy states where the charge carriers can be considered as free carriers are called extended state as here the wave function extends over the whole atomic structure, while the tail and defect states are called localized states due to the localized nature of the wave functions. The mobility of the carriers in the localized states is strongly reduced. This feature of a sharp drop in the carrier mobility in the localized states in comparison to the extended states is used to define the band gap in a-Si:H, also called as mobility gap (E_{mob}). As the electronic transport mostly occur at the band edges, the band tails greatly determine the electronic transport properties. The deep defect states determine the electronic properties by controlling the trapping and recombination kinetics.

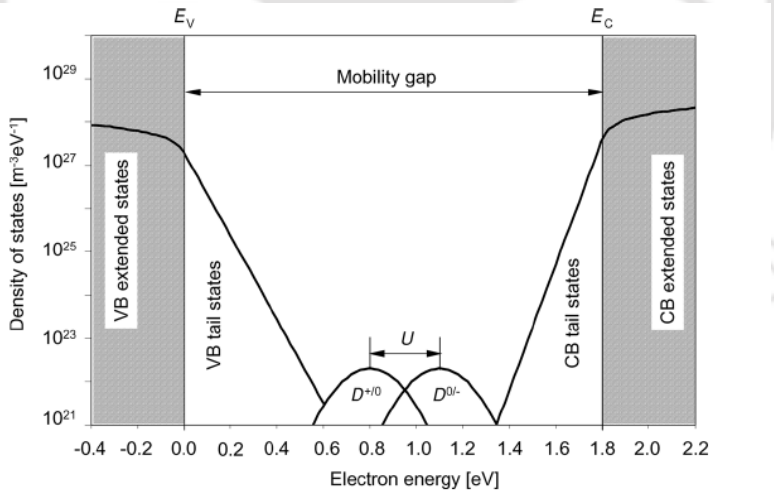

Figure 1.2: Density of states picture for a-Si:H [77].

For the electron transport one can write the following expression for conductivity,

$$\sigma = \sigma_o \exp\left[\frac{-(E_c - E_f)}{K_B T}\right] \text{ ……..1.1}$$

Where E_f is the Fermi Energy, σ_o the pre factor, K_B the Boltzmann constant and T is the temperature. For typical intrinsic materials the Fermi energy, E_f lies at the mid gap and activation energy, E_a defined as E_c-E_f which is used to assess the presence of impurity in the materials. With the addition of impurities, the Fermi level shifts. Due to the presence of either intentional (B or P dopant atom) or unintentional (O or N) impurities, the Fermi level shifts over several tenth of electron volts towards the conduction and valence bands.

The optical properties of a-Si:H are considerably important. In a-Si the potential is not periodic and the weak disorder potential results in a perturbation in the wave function and has the effect of scattering the electron. A loss of *k*-conservation, the conservation of momentum selection rule remains no longer valid in optical transitions. Consequently, the distinction between direct and indirect band gap is lost and optical transitions occur between the states overlapping in real space. Hence, silicon, an indirect band gap semiconductor, behaves as direct band gap material in amorphous state. This leads to the high optical absorption co-efficient in amorphous silicon as compared to c-Si [76].

The successful doping of a-Si triggered a tremendous interest in this material and the research activities in this material grew explosively. Recently the interest has been focused on nanocrystalline silicon (nc-Si:H) [78-82] due to its novel properties like high band gap [58, 83-85], visible photoluminescence[53, 85-87] higher absorption coefficient and electroluminescence etc. [86]. The attention on this nanocrystalline silicon has increased because one wants to use it in highly efficient thin films solar cell instead of a-Si:H against the light induced degradation effect. A significant current enhancement (longer wavelength range of 650-1000 nm region) is obtained in solar cells by implementing nanostructure in multi band gap triple junction solar cell. The material preparation is similar to that of

amorphous and microcrystalline silicon however, a slight variation in deposition parameters is required. These transitions can be achieved with the help of dilution of the precursor gases such as silane (SiH_4), di-silane (Si_2H_6), etc. with different diluents gases like hydrogen and argon as well as varying other deposition parameters. This material is single or multiphase poly-crystals and its crystal size is of the order of a few nanometers. Depending on the deposition conditions, more ordered regions in the amorphous matrix gets transformed into nanocrystallites, which grow in size and may result into nanocrystalline Si thin films [20, 21, 88-90]

As mentioned earlier, a new class of material i.e a-Si:H/nc-Si:H superlattice structures, prepared by depositing alternate layer of thin films of amorphous and nano-crystalline silicon, show many interesting features such as stable photoluminescence and enhanced vertical photosensitivity etc. Superlattice structures based on amorphous layers have also been proposed as novel transistors[91]. Such superlattice structure was proposed to offer considerably higher performance and mobility than a typical a-Si:H thin film transistors. The photonic and plasmonic enhancements in a-Si:H/nc-Si:H superlattice structures have previously been reported by several groups [92-94]. Very recently, S. Pattnaik et. al. [95] measured a large photo current enhancement in (a-Si:H/nc-Si:H) superlattice based solar cells. Even thermal transport properties of these structures were investigated and studied. It was found that thermal conductivity of superlattice structure was 2 $Wm^{-1}K^{-1}$, which is 75 times smaller than room temperature (RT) thermal conductivity of bulk crystalline silicon [96]. Internal interfaces and boundaries in nanostructures creates thermal carriers scattering events and tailoring the periods or structure of these boundaries offers a unique method for

tuning thermal properties, while this aspect of reducing the thermal conductivity alone has resulted in ultralow thermal conductivity and proves useful for thermal barrier applications.

1.2 Method of preparation of a-Si:H and nc-Si:H thin films and a-Si:H/nc-Si:H superlattice structures

Amorphous and nanocrystalline silicon thin films are commonly produced using the method that first resulted in hydrogen incorporation in the materials i.e glow discharge technique also known as Plasma Enhanced Chemical Vapor Deposition (PECVD) [65]. A silicon containing gas usually silane (SiH_4) is admitted to a vacuum reactor chamber. A gas discharge is then initiated and maintained by an electric field between two parallel plates, using either a dc voltage or a voltage in the radio frequency domain (13.65-200 MHz). The initial event for the growth of a-Si, micro-Si and nano-Si is the decomposition process of the source gas i.e SiH_4 and SiH_4/H_2 under the influence of high electric field. Figure 1.3 shows the schematic of the dissociation pathways of SiH_4 and H_2 through electronic excited state of these molecules by inelastic collision with the high energy electron in the plasma [97]. Electronic excited states of the complicated molecules like SiH_4 are usually dissociate to SiH_2, SiH, Si, H_2 and H as shown in Fig 1.3 depending on the stereo chemical structures of the excited states. Figure 1.4 shows the number densities of different radicals in steady state plasma [97]. Among these radicals, SiH_3 is the least reactive one and has the highest concentration, irrespective of the initial formation rate and thus mainly responsible for the growth of micro/nano crystalline as well as a-Si. During the growth process, these radicals so formed undergo secondary gas phase reactions with the parent SiH_4 and H_2 and hence forms a steady state [97].

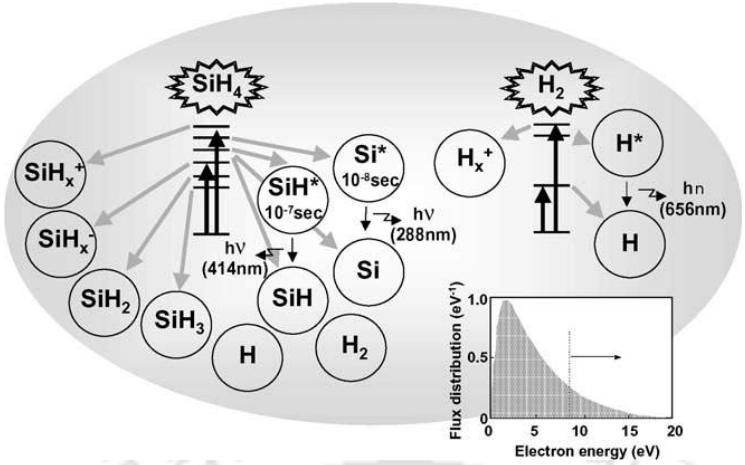

Figure 1.3: Schematic of the dissociation processes of SiH_4 and H_2 molecules under the influence of high rf-field [97].

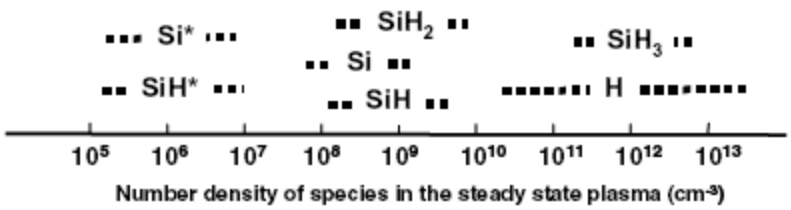

Figure 1.4: Number density of different film forming radicals in steady state plasma [97].

In case of microcrystalline and nanocrysatlline silicon thin films growth, the same radicals are involved. However, in this case abundant hydrogen radicals play a decisive role. In order to explain the specific phenomena in the formation process of micro-Si and nano-Si, three models have been proposed: a) surface diffusion model [55], b) etching model [98], c)chemical annealing model [99] . In the surface diffusion model, a large amount of atomic H_2 flux present in the plasma covers the surface of the growing film by bonding with the Si atom and during this process a local heating also takes place through H exchanging reaction on the film formation surface. As a result SiH_3 absorbed on the surface can find the energetically favorable sites, leading to a formation of atomically ordered structures. In the

etching model with the increase in H_2 dilution, the atomic H reaching the films growing surface breaks the weak Si-Si bonds and forms a strong Si-H bonds resulting in the formation of ordered structures. In chemical annealing model, hydrogen plasma treatment is conducted in a layer by layer growth by alternative sequence of a-Si and H_2 plasma treatment. This process is repeated several times in order to obtain the proper thickness for the evolution of film structure. During the treatment, many H_2 atoms are permeated in the sub surface region giving rise to crystallization of amorphous silicon through the formation of flexible network with sufficient amount of H atom in the sub surface region without removal of any Si atoms.

One of the drawback of this PECVD or the glow discharge technique; the deposition rate is quite low (<3 Å/s) therefore, much efforts has been put in research on compatible methods to increase the deposition rates. Later, very high frequency CVD has attracted much attention of the research, since the use of this technique results slight higher deposition rates as compared to PECVD techniques [39, 40]. Several other techniques were also employed in order to get a device quality a-Si, micro-Si/nc-Si such as reactive sputtering, direct photo CVD technique, hot-wire chemical vapor deposition technique etc [35, 36, 57]. Among these techniques, hot wire chemical vapor deposition (HWCVD) technique is continuously drawing the attention of researchers due to certain advantages such as i) the lack of ion bombardment induced defects in growing films and ii) higher decomposition rate thus better utilization of reactant gases over the conventional plasma enhanced CVD technique. The deposition rate in case of HWCVD is also found to be higher especially for nano and microcrystalline silicon films, where PECVD requires heavy hydrogen dilution causing the deposition rates to drop down significantly. Interestingly, in HWCVD, the microstructure of

the films can be easily changed from amorphous to microcrystalline by just varying any of the process parameter i.e., substrate and filament temperature, process pressure, gas flow rates etc [100-102]. This method was first introduced by Wiesmann in 1979 [103], who has made the foil using carbon or tungsten, which was heated at a temperature of 1400-1600 ^{o}C, in order to thermally decompose the SiH_4 into gaseous mixture of H_2 and silicon atoms. Later in the year 1986, Matsumura had used heated tungsten wire instead of foil for the fabrication of amorphous silicon and named the technique as catalytic chemical vapor deposition [104]. A prominent feature about this technique was realized further by the Doyle et.al [105] and Matsumura in 1989 [106]. This technique has shown a very high deposition rate (>10 Å/sec) as compared to the other techniques. Till 1991, the quality of films prepared by HWCVD was not as good as the films fabricated using PECVD techniques due to the unsuitable deposition parameters. Later in the year 1992 [107], with the proper selection of the deposition parameter, device quality films were fabricated using this technique. This triggered a new interest in the deposition method which was renamed as hot wire chemical vapor deposition (HWCVD). The results stimulated the a-Si research community to work on this upcoming technique for the deposition of amorphous as well as microcrystalline silicon and other semiconductors at reasonably low cost. Dusane et. al in 1993 [84], demonstrated that a microcrystalline-Si thin films could be fabricated using this techniques using pure silane at filament temperature 1400 ^{o}C. Further in 1996, Heintze et al., described the transition from amorphous to nanocrystalline silicon with the increase in H_2 dilution in silane [108]. The hot filament decomposes all the hydrogen molecules into reactive atoms that effectively etch silicon disorder structures leading to a transition from amorphous to nanocrystalline silicon. The a-Si produced by HWCVD has superior

electronic properties as compared to the conventional PECVD technique [109]. Moreover the high deposition rate of ~ 70 Å/sec, the rate that is more than an order of magnitude higher as compared to 13.56 MHz PECVD, made this technique more acceptable [108, 110]. Using HWCVD technique, the first thin film silicon solar cells were made in 1993 at NREL and University of Kaiserslautern, while TFTs were made in 1995 at Utrecht University and JAIST [111]. The solar cell fabricated using this technique, resulted in cell efficiency ~10% in nip based solar cell structure [112] .

1.3 Motivations

As discussed in the previous section, a-Si:H/nc-Si:H superlattice structures show many interesting properties which make this material a good candidate for device applications. However, the main challenges in multilayer structures based electronic devices is the interface states; the interface states between the sublayer may act as recombination centers thereby controlling the transport mechanism and overall performanance of the devices. Therefore, proper knowledge of these states is very important for device fabrication. One of the motivation behind this thesis is to study the interface states in a-Si:H/nc-Si:H superlattice structures, which play an important role in tunning the optoelectronic properties of these structures. Another motivation of the work had been the growth of silicon nanocrystallities in a-Si:H matrix with tunable optoelectronic properties and visble photoluminescence by controlling the thickness of nc-Si layer sandwiched between the a-Si:H layers.

In order to achieve the above mentioned target, the following objectives and work plan have been set.

1. Optimization of deposition parameters for the fabrication of device quality a-Si:H, nc-Si:H using both HWCVD and rf-PECVD techniques and subsequent fabrication of a-Si:H/nc-Si:H superlattice structures.

2. Study of structural and optical properties of these films using various characterization techniques such as X-ray Diffraction (XRD), Raman scattering spectroscopy, Transmission Electron Microscope (TEM) and Field Emission Scanning Electron Microscope (FESEM), Ultraviolet visible near infrared (UV-Vis-NIR) spectroscopy etc.

3. Study of electrical transport properties of superlattice structure in both coplanar as well as transverse geometry as the electrical transport is anisotropic in these structure.

4. Fabrication of nc-Si/a-Si:H superlattice structures with thin nc-Si layer to control the size of Si nanocrystals and Photoluminescence measurements in these structures.

1.4 Contents of Thesis Chapters

The present thesis consists of eight chapters. Chapter 1 is the introduction, where a brief introduction about silicon and its allotropes has been discussed and also motivation behind the present thesis is also presented. Chapter 2, which gives a description of detail of samples preparation techniques such as HWCVD and rf-PECVD as well as the detail of the deposition parameters which have been used for the preparation of a-Si:H, nc-Si:H and a-Si:H/nc-Si:H superlattice structures. This chapter also gives a brief discussion on the different characterization techniques used for the analysis of structural, optical and electrical properties of the Si thin films.

Chapter 3 contains the extensive studies on the influence of different deposition parameters such as H_2 dilution of silane, substrate temperature and rf-power on the structural and optoelectronic properties of Si thin films.

Chapter 4 contains the detail studies on microstructural changes in a-Si:H thin films irradiated with different laser source at different power density using Raman spectroscopy.

Chapter 5 contains the detail studies on persistent photoconductivity (PPC), which was observed for the first time in the a-Si:H/nc-Si:H superlattice structures. PPC decay time constant, its dependence on exposure time, electric field, number of periods and annealing temperature have been discussed in detail.

Chapter 6 contains the detail studies on the density of states (DOS) in single layer a-Si:H and nc-Si:H as well as the superlattice structures of a-Si:H and nc-Si:H thin films using space charge limited current (SCLC) measurements.

Chapter 7 presents a systematic studies on visible photoluminescence which was observed in these a-Si:H/nc-Si:H superlattice structures without any post deposition processing at room temperature.

Chapter 8 is the final chapter of the thesis, which summarizes the content of each chapter and gives the final conclusion based on the work reported in this thesis. The thesis work is concluded with the scope for future work from the present investigation.

1.5 References

[1] S. Tiwari, F. Rana, H. Hanafi, A. Hartstein, E.F. Crabbé, K. Chan, A silicon nanocrystals based memory, Applied Physics Letters, 68 (1996) 1377-1379.

[2] Y.T. Tan, T. Kamiya, Z.A.K. Durrani, H. Ahmed, Room temperature nanocrystalline silicon single-electron transistors, Journal of Applied Physics, 94 (2003) 633-637.

[3] A. Fujiwara, H. Inokawa, K. Yamazaki, H. Namatsu, Y. Takahashi, N.M. Zimmerman, S.B. Martin, Single electron tunneling transistor with tunable barriers using silicon nanowire metal-oxide-semiconductor field-effect transistor, Applied Physics Letters, 88 (2006) 053121.

[4] S.J. Angus, A.J. Ferguson, A.S. Dzurak, R.G. Clark, Gate-Defined Quantum Dots in Intrinsic Silicon, Nano Letters, 7 (2007) 2051.

[5] T. Söderström, F.-J. Haug, V. Terrazzoni-Daudrix, C. Ballif, Optimization of amorphous silicon thin film solar cells for flexible photovoltaics, Journal of Applied Physics, 103 (2008) 114509.

[6] Y. Vygranenko, E. Fathi, A. Sazonov, M. Vieira, A. Nathan, Nanocrystalline p-layer for a-SiH pin solar cells and photodiodes, Solar Energy Materials and Solar Cells, 94 (2010) 1860-1863.

[7] J. Ni, J. Zhang, Y. Cao, X. Wang, X. Chen, X. Geng, Y. Zhao, Low temperature deposition of high open-circuit voltage (>1.0V) p–i–n type amorphous silicon solar cells, Solar Energy Materials and Solar Cells, 95 (2011) 1922-1926.

[8] J. Ma, J. Ni, J. Zhang, Z. Huang, G. Hou, X. Chen, X. Zhang, X. Geng, Y. Zhao, Improvement of solar cells performance by boron doped amorphous silicon carbide/nanocrystalline silicon hybrid window layers, Solar Energy Materials and Solar Cells, 114 (2013) 9-14.

[9] F.T. Si, D.Y. Kim, R. Santbergen, H. Tan, R.A.C.M.M.v. Swaaij, A.H.M. Smets, O. Isabella, M. Zeman, Quadruple-junction thin film silicon based solar cells with high open-circuit voltage, Applied Physics Letters, 105 (2014) 063902.

[10] F. Wang, X. Zhang, L. Wang, J. Fang, C. Wei, X. Chen, G. Wang, Y. Zhao, Boron doped nanocrystalline silicon amorphous silicon hybrid emitter layers used to improve the performance of silicon heterojunction solar cells, Solar Energy, 108 (2014) 308-314.

[11] A.T. Hatzopoulos, I. Pappas, D.H. Tassis, N. Arpatzanis, C.A. Dimitriadis, F. Templier, M. Oudwan, Analytical current voltage model for nanocrystalline silicon thin-film transistors, Applied Physics Letters, 89 (2006) 193504.

[12] I.-C. Cheng, S. Wagner, Hole and electron field effect mobilities in nanocrystalline silicon deposited at 150°C, Applied Physics Letters, 80 (2002) 440-442.

[13] C.S. McCormick, C.E. Weber, J.R. Abelson, S.M. Gates, An amorphous silicon thin film transistor fabricated at 125°C by dc reactive magnetron sputtering, Applied Physics Letters, 70 (1997) 226-227.

[14] C.-H. Lee, A. Sazonov, A. Nathan, High-mobility nanocrystalline silicon thin film transistors fabricated by plasma-enhanced chemical vapor deposition, Applied Physics Letters, 86 (2005) 222106.

[15] D.L. Staebler, C.R. Wronski, Reversible conductivity changes in discharge-produced amorphous Si, Applied Physics Letters, 31 (1977) 292-294.

[16] P. Stradins, S. Shimizu, M. Kondo, A. Matsuda, Less-understood phenomena in the light induced degradation and photocarrier capture in a-Si:H, Journal of Non-Crystalline Solids, 299-302 (2002) 460-465.

[17] J.M. Pearce, J. Deng, R.W. Collins, C.R. Wronski, Light-induced defect states in hydrogenated amorphous silicon centered around 1.0 and 1.2 eV from the conduction band edge, Applied Physics Letters, 83 (2003) 3725-3727.

[18] D. Han, H. Fritzsche, Study of light-induced creation of defects in a-Si:H by means of single and dual-beam photoconductivity, Journal of Non-Crystalline Solids, 59-60 (1983) 397-400.

[19] H. Fritzsche, Photo-induced structural changes associated with the Staebler-Wronski effect in hydrogenated amorphous silicon, Solid State Communications, 94 (1995) 953-955.

[20] C. Longeaud, J.P. Kleider, P. Roca i Cabarrocas, S. Hamma, R. Meaudre, M. Meaudre, Properties of a new a-Si:H-like material: hydrogenated polymorphous silicon, Journal of Non-Crystalline Solids, 227-230 (1998) 96-99.

[21] P. Roca i Cabarrocas, Plasma enhanced chemical vapor deposition of amorphous, polymorphous and microcrystalline silicon films, Journal of Non-Crystalline Solids, 266-269 (2000) 31-37.

[22] M. Meaudre, R. Meaudre, R. Butté, S. Vignoli, C. Longeaud, J.P. Kleider, P.R.i. Cabarrocas, Midgap density of states in hydrogenated polymorphous silicon, Journal of Applied Physics, 86 (1999) 946-950.

[23] D. Stieler, V.L. Dalal, K. Muthukrishnan, M. Noack, E. Schares, Electron mobility in nanocrystalline silicon devices, Journal of Applied Physics, 100 (2006) 036106.

[24] T. Su, T. Ju, B. Yan, J. Yang, S. Guha, P.C. Taylor, ESR study of the hydrogenated nanocrystalline silicon thin films, Journal of Non-Crystalline Solids, 354 (2008) 2231-2234.

[25] J. Meier, R. Flückiger, H. Keppner, A. Shah, Complete microcrystalline pin solar cell Crystalline or amorphous cell behavior?, Applied Physics Letters, 65 (1994) 860-862.

[26] O. Vetterl, F. Finger, R. Carius, P. Hapke, L. Houben, O. Kluth, A. Lambertz, A. Mück, B. Rech, H. Wagner, Intrinsic microcrystalline silicon: A new material for photovoltaics, Solar Energy Materials and Solar Cells, 62 (2000) 97-108.

[27] H.C. Dickey, T.T. Meek, Active electronic devices fabricated by DC plasma arc spray process, Vacuum, 59 (2000) 179-184.

[28] R. Goswami, S. Sampath, H. Herman, J.B. Parise, Shock synthesis of nanocrystalline Si by thermal spraying, Journal of Materials Research, 14 (2011) 3489-3492.

[29] S.-W. Fu, H.-J. Chen, H.-T. Wu, C.-F. Shih, Enhancing crystallization of silicon nanocrystal embedded in silicon-rich oxide by ion beam-assisted sputtering, Materials Science in Semiconductor Processing, 56 (2016) 1-4.

[30] J.A. Peck, P. Zonooz, D. Curreli, G.A. Panici, B.E. Jurczyk, D.N. Ruzic, High deposition rate nanocrystalline and amorphous silicon thin film production via surface wave plasma source, Surface and Coatings Technology, 325 (2017) 370-376.

[31] K. Yoshino, G. Ohkawara, H. Ueyama, H. Shirai, Fast deposition of microcrystalline silicon films with preferred (220) crystallographic texture using the high-density microwave plasma, Solar Energy Materials and Solar Cells, 74 (2002) 505-511.

[32] G. Ohkawara, M. Nakajima, H. Ueyama, H. Shirai, Relationship between microstructure and photovoltaic performance in microcrystalline silicon film solar cells fabricated by a high-density microwave plasma, Thin Solid Films, 427 (2003) 27-32.

[33] J. Haijun, K.S. Jhantu, O. Naoyuki, S. Hajime, Effect of substrate bias on high-rate synthesis of microcrystalline silicon films using a high-density microwave SiH 4 /H 2 plasma, Journal of Physics D: Applied Physics, 39 (2006) 3844.

[34] H. Shirai, K. Yoshino, G. Ohkawara, H. Ueyama, Novel high-density microwave plasma utilizing an internal spoke antenna for fast deposition of microcrystalline silicon films, Japanese Journal of Applied Physics, Part 2: Letters, 40 (2001) L701-L704.

[35] N. Saxena, D.E. Albright, C.M. Fortmann, T.W. Fraser Russell, P.M. Fauchet, I.H. Campbell, Temperature dependence of H radical etching in the deposition of microcrystalline silicon alloy thin films by HG-sensitized photo-CVD, Journal of Non-Crystalline Solids, 114 (1989) 801-803.

[36] R. Baghdad, D. Benlakehal, X. Portier, K. Zellama, S. Charvet, J.D. Sib, M. Clin, L. Chahed, Deposition of nanocryctalline silicon thin films: Effect of total pressure and substrate temperature, Thin Solid Films, 516 (2008) 3965-3970.

[37] G. Morell, R.S. Katiyar, S.Z. Weisz, H. Jia, J. Shinar, I. Balberg, Raman study of the network disorder in sputtered and glow discharge a-Si:H films, Journal of Applied Physics, 78 (1995) 5120-5125.

[38] W.M.M. Kessels, R.J. Severens, A.H.M. Smets, B.A. Korevaar, G.J. Adriaenssens, D.C. Schram, M.C.M.v.d. Sanden, Hydrogenated amorphous silicon deposited at very high growth rates by an expanding Ar–H2–SiH4 plasma, Journal of Applied Physics, 89 (2001) 2404-2413.

[39] J. Gope, S. Kumar, S. Sudhakar, K. Lodhi, C.M.S. Rauthan, P.C. Srivastava, Influence of argon dilution on the growth of amorphous to ultra nanocrystalline

silicon films using VHF PECVD process, Journal of Alloys and Compounds, 577 (2013) 710-716.

[40] A.V. Shah, J. Meier, E. Vallat-Sauvain, N. Wyrsch, U. Kroll, C. Droz, U. Graf, Material and solar cell research in microcrystalline silicon, Solar Energy Materials and Solar Cells, 78 (2003) 469-491.

[41] S. Hitoshi, M. Keigo, M. Takuya, K. Takashi, K. Michio, N. Sachiko, T. Yoshiaki, K. Hirotaka, Y. Isao, High-efficiency microcrystalline silicon solar cells on honeycomb textured substrates grown with high-rate VHF plasma-enhanced chemical vapor deposition, Japanese Journal of Applied Physics, 54 (2015) 08KB05.

[42] G. Bugnon, A. Feltrin, F. Meillaud, J. Bailat, C. Ballif, Influence of pressure and silane depletion on microcrystalline silicon material quality and solar cell performance, Journal of Applied Physics, 105 (2009) 064507.

[43] H. Takatsuka, M. Noda, Y. Yonekura, Y. Takeuchi, Y. Yamauchi, Development of high efficiency large area silicon thin film modules using VHF-PECVD, Solar Energy, 77 (2004) 951-960.

[44] S.C. Kim, M.H. Jung, J. Jang, Growth of microcrystal silicon by remote plasma chemical vapor deposition, Applied Physics Letters, 58 (1991) 281-283.

[45] S.C. Kim, J.T. Hwang, S.K. Lee, C.Y. Jung, S.M. Soe, S.O. Koh, K.S. Chung, J. Jang, Microcrystal Si Films Prepared by Remote Plasma CVD, MRS Proceedings, 164 (2011) 171.

[46] G.N. Parsons, D.V. Tsu, G. Lucovsky, Properties of intrinsic and doped a-Si:H deposited by remote plasma enhanced chemical vapor deposition, Journal of Vacuum Science & Technology A: Vacuum, Surfaces, and Films, 6 (1988) 1912-1916.

[47] R.R. Arya, D.E. Carlson, Amorphous silicon PV module manufacturing at BP solar, Progress in Photovoltaics: Research and Applications, 10 (2002) 69-76.

[48] R. Nozawa, H. Takeda, M. Ito, M. Hori, T. Goto, In situ observation of hydrogenated amorphous silicon surfaces in electron cyclotron resonance hydrogen plasma annealing, Journal of Applied Physics, 85 (1999) 1172-1177.

[49] R. Nozawa, H. Takeda, M. Ito, M. Hori, T. Goto, Substrate bias effects on low temperature polycrystalline silicon formation using electron cyclotron resonance SiH4/H2 plasma, Journal of Applied Physics, 81 (1997) 8035-8039.

[50] K.C. Wang, H.L. Hwang, P.T. Leong, T.R. Yew, Microstructures of low-temperature-deposited polycrystalline silicon with micrometer grains, Journal of Applied Physics, 77 (1995) 6542-6548.

[51] H.S. Tae, S.H. Hwang, S.J. Park, E. Yoon, K.W. Whang, Effects of process parameters on low-temperature silicon homoepitaxy by ultrahigh-vacuum electron-cyclotron-resonance chemical-vapor deposition, Journal of Applied Physics, 78 (1995) 4112-4117.

[52] S.J. Jones, Y. Chen, D.L. Williamson, U. Kroll, P. Roca i Cabarrocas, The effects of Ar and He dilution of silane plasmas on the microstructure of a-Si:H detected by small-angle X-ray scattering, Journal of Non-Crystalline Solids, 164-166 (1993) 131-134.

[53] J.H. Shim, S. Im, N.H. Cho, Nanostructural features of nc-Si:H thin films prepared by PECVD, Applied Surface Science, 234 (2004) 268-273.

[54] M.B. Park, N.H. Cho, Structural, chemical and optical features of nanocrystalline Si films prepared by PECVD techniques, Applied Surface Science, 190 (2002) 151-156.

[55] A. Matsuda, Growth mechanism of microcrystalline silicon obtained from reactive plasmas, Thin Solid Films, 337 (1999) 1-6.

[56] S. Samanta, D. Das, Nanocrystalline silicon thin films from SiH4 plasma diluted by H2 and He in RF-PECVD, Journal of Physics and Chemistry of Solids, 105 (2017) 90-98.

[57] P. Gogoi, H.S. Jha, P. Agarwal, Effect of Silane flow rate on microstructure of Silicon films deposited by HWCVD, Journal of Non-Crystalline Solids, 358 (2012) 1990-1994.

[58] P. Gogoi, H.S. Jha, P. Agarwal, High band gap nanocrystallite embedded amorphous silicon prepared by hotwire chemical vapour deposition, Thin Solid Films, 518 (2010) 6818-6828.

[59] A.H. Mahan, J. Carapella, B.P. Nelson, R.S. Crandall, I. Balberg, Deposition of device quality, low H content amorphous silicon, Journal of Applied Physics, 69 (1991) 6728-6730.

[60] B.P. Swain, B.S. Swain, N.M. Hwang, A comparative chemical network study of HWCVD deposited amorphous silicon and carbon based alloys thin films, Journal of Alloys and Compounds, 588 (2014) 343-347.

[61] M. Agarwal, A. Pawar, N. Wadibhasme, R. Dusane, Controlling the c-Si/a-Si:H interface in silicon heterojunction solar cells fabricated by HWCVD, Solar Energy, 144 (2017) 417-423.

[62] S.K. Chong, B.T. Goh, Z. Aspanut, M.R. Muhamad, C.F. Dee, S.A. Rahman, Effect of substrate temperature on gold-catalyzed silicon nanostructures growth by hot-wire

chemical vapor deposition (HWCVD), Applied Surface Science, 257 (2011) 3320-3324.

[63] K.H. Jun, K.S. Lim, Enhanced vertical photo-sensitivity in μc-Si:H/a-Si:H superlattices, Journal of Non-Crystalline Solids, 261 (2000) 268-272.

[64] V.L. Dalal, A. Madhavan, Alternative designs for nanocrystalline silicon solar cells, Journal of Non-Crystalline Solids, 354 (2008) 2403-2406.

[65] H.F. Sterling, R.C.G. Swann, Chemical vapour deposition promoted by r.f. discharge, Solid-State Electronics, 8 (1965) 653-654.

[66] J.H.A.a.H.F.S. R.C. Chittick, The preparation and properties of amorphous silicon, Journal of the electrochemical society, 116 (1969) 77-81.

[67] R.C. Chittick, J.H. Alexander, H.F. Sterling, The Preparation and Properties of Amorphous Silicon, Journal of The Electrochemical Society, 116 (1969) 77-81.

[68] W.E. Spear, P.G. Le Comber, Substitutional doping of amorphous silicon, Solid State Communications, 17 (1975) 1193-1196.

[69] W.E. Spear, P.G.L. Comber, Electronic properties of substitutionally doped amorphous Si and Ge, The Philosophical Magazine: A Journal of Theoretical Experimental and Applied Physics, 33 (1976) 935-949.

[70] W. Paul, A.J. Lewis, G.A.N. Connell, T.D. Moustakas, Doping, Schottky barrier and p□n junction formation in amorphous germanium and silicon by rf sputtering, Solid State Communications, 20 (1976) 969-972.

[71] D.E. Carlson, C.R. Wronski, Amorphous silicon solar cell, Applied Physics Letters, 28 (1976) 671-673.

[72] J. A. J. Lewis, G.A.N. Connel, W. Paul, J. R. Pawlik and R.J. Temkin, Tetrahedrally bonded amorphous semiconductors, AIP Conf. Proceeding, 20 (1974) 27.

[73] A. Madan, J. McGill, W. Czubatyj, J. Yang, S.R. Ovshinsky, Metal-insulator-semiconductor solar cells using amorphous Si:F:H alloys, Applied Physics Letters, 37 (1980) 826-828.

[74] W.H. Zachariasen, The atomic arrangement in glass, Journal of the American Chemical Society, 54 (1932) 3841-3851.

[75] N.F. Mott, Conduction in non-crystalline materials, Philosophical Magazine, 19 (1969) 835-852.

[76] R.A. Street, Hydrogenated Amorphous Silicon, Cambridge University Press, , (1992).

[77] M. Zemen, Advanced amorphous silicon solar cell technologies, Thin Film Solar Cells: Fabication, Characterisation and applications, John Wiley and Sons 2006, Ed. J. Poortmans and V. Arkhipov, , ((2006)).

[78] C. Song, G.R. Chen, J. Xu, T. Wang, H.C. Sun, Y. Liu, W. Li, Z.Y. Ma, L. Xu, X.F. Huang, K.J. Chen, Evaluation of microstructures and carrier transport behaviors during the transition process from amorphous to nanocrystalline silicon thin films, Journal of Applied Physics, 105 (2009) 054901.

[79] S. Klein, F. Finger, R. Carius, M. Stutzmann, Deposition of microcrystalline silicon prepared by hot-wire chemical-vapor deposition: The influence of the deposition parameters on the material properties and solar cell performance, Journal of Applied Physics, 98 (2005) 024905.

[80] S. Liu, X. Zeng, W. Peng, H. Xiao, W. Yao, X. Xie, C. Wang, Z. Wang, Improvement of amorphous silicon n-i-p solar cells by incorporating double-layer hydrogenated

nanocrystalline silicon structure, Journal of Non-Crystalline Solids, 357 (2011) 121-125.

[81] J. Bailat, E. Vallat-Sauvain, L. Feitknecht, C. Droz, A. Shah, Microstructure and open-circuit voltage of n-i-p microcrystalline silicon solar cells, Journal of Applied Physics, 93 (2003) 5727-5732.

[82] D. Benlakehal, A. Belfedal, Y. Bouizem, J.D. Sib, L. Chahed, K. Zellama, Electronic transport mechanism in intrinsic and doped nanocrystalline silicon films deposited by RF-magnetron sputtering at low temperature, Superlattices and Microstructures, 100 (2016) 228-236.

[83] G. Viera, M. Mikikian, E. Bertran, P.R.i. Cabarrocas, L. Boufendi, Atomic structure of the nanocrystalline Si particles appearing in nanostructured Si thin films produced in low-temperature radiofrequency plasmas, Journal of Applied Physics, 92 (2002) 4684-4694.

[84] R.O. Dusane, S.R. Dusane, V.G. Bhide, S.T. Kshirsagar, Hydrogenated microcrystalline silicon films produced at low temperature by the hot wire deposition method, Applied Physics Letters, 63 (1993) 2201-2203.

[85] H. Takagi, H. Ogawa, Y. Yamazaki, A. Ishizaki, T. Nakagiri, Quantum size effects on photoluminescence in ultrafine Si particles, Applied Physics Letters, 56 (1990) 2379-2380.

[86] D. Han, K. Wang, Photo- and electro-luminescence of a-Si:H and mixed-phase alloys, Solar Energy Materials and Solar Cells, 78 (2003) 181-233.

[87] D. Han, G. Yue, J.D. Lorentzen, J. Lin, H. Habuchi, Q. Wang, Optical and electronic properties of microcrystalline silicon as a function of microcrystallinity, Journal of Applied Physics, 87 (2000) 1882-1888.

[88] P.R.i. Cabarrocas, Plasma Deposition of Silicon Clusters: A Way to Produce Silicon Thin Films With Medium Range Order ?, MRS Proceedings, 507 (2011) 375.

[89] M. Meaudre, R. Meaudre, R. Butté, S. Vignoli, C. Longeaud, J.P. Kleider, P. Roca i Cabarrocas, Midgap density of states in hydrogenated polymorphous silicon, Journal of Applied Physics, 86 (1999) 946-950.

[90] D. Gracin, A. Gajović, K. Juraić, M. Čeh, Z. Remeš, A. Poruba, M. Vaněček, Spectral response of amorphous–nano-crystalline silicon thin films, Journal of Non-Crystalline Solids, 354 (2008) 2286-2290.

[91] J. Dresner, Transistor having a superlattice, U. S Patent DOI (1987) 4,697,197

[92] C. Battaglia, J. Escarré, K. Söderström, L. Erni, L. Ding, G. Bugnon, A. Billet, M. Boccard, L. Barraud, S. De Wolf, F.-J. Haug, M. Despeisse, C. Ballif, Nanoimprint Lithography for High-Efficiency Thin-Film Silicon Solar Cells, Nano Letters, 11 (2011) 661-665.

[93] B. Curtin, R. Biswas, V. Dalal, Photonic crystal based back reflectors for light management and enhanced absorption in amorphous silicon solar cells, Applied Physics Letters, 95 (2009) 231102.

[94] O. Isabella, J. Krč, M. Zeman, Modulated surface textures for enhanced light trapping in thin-film silicon solar cells, Applied Physics Letters, 97 (2010) 101106.

[95] S. Pattnaik, N. Chakravarty, R. Biswas, V. Dalal, D. Slafer, Nano-photonic and nano-plasmonic enhancements in thin film silicon solar cells, Solar Energy Materials and Solar Cells, 129 (2014) 115-123.

[96] F.-L. Arthur, M. Samy, A. Tristan, L. David, T. Konstantinos, Thermal properties of amorphous/crystalline silicon superlattices, Journal of Physics: Condensed Matter, 26 (2014) 355801.

[97] A. Matsuda, Microcrystalline silicon.: Growth and device application, Journal of Non-Crystalline Solids, 338-340 (2004) 1-12.

[98] C.C. Tsai, G.B. Anderson, R. Thompson, B. Wacker, Control of silicon network structure in plasma deposition, Journal of Non-Crystalline Solids, 114 (1989) 151-153.

[99] K. Nakamura, K. Yoshino, S. Takeoka, I. Shimizu, Roles of atomic hydrogen in chemical annealing, Japanese Journal of Applied Physics, 34 (1995) 442-449.

[100] A.H. Mahan, Status of Cat CVD (Hot Wire CVD) research in the United States, Thin Solid Films, 395 (2001) 12-16.

[101] H. Matsumura, Summary of research in NEDO Cat CVD project in Japan, Thin Solid Films, 395 (2001) 1-11.

[102] Y. Wang, X. Geng, H. Stiebig, F. Finger, Stability of microcrystalline silicon solar cells with HWCVD buffer layer, Thin Solid Films, 516 (2008) 733-735.

[103] H. Wiesmann, A.K. Ghosh, T. McMahon, M. Strongin, a-Si : H produced by high-temperature thermal decomposition of silane, Journal of Applied Physics, 50 (1979) 3752-3754.

[104] M. Hideki, Catalytic Chemical Vapor Deposition (CTC–CVD) Method Producing High Quality Hydrogenated Amorphous Silicon, Japanese Journal of Applied Physics, 25 (1986) L949.

[105] J. Doyle, R. Robertson, G.H. Lin, M.Z. He, A. Gallagher, Production of high quality amorphous silicon films by evaporative silane surface decomposition, Journal of Applied Physics, 64 (1988) 3215-3223.

[106] H. Matsumura, Study on catalytic chemical vapor deposition method to prepare hydrogenated amorphous silicon, Journal of Applied Physics, 65 (1989) 4396-4402.

[107] R.S. Crandall, A.H. Mahan, B. Nelson, M. Vanecek, I. Balberg, Properties of hydrogenated amorphous silicon produced at high temperature, AIP Conference Proceedings, 268 (1992) 81-87.

[108] M. Heintze, R. Zedlitz, H.N. Wanka, M.B. Schubert, Amorphous and microcrystalline silicon by hot wire chemical vapor deposition, Journal of Applied Physics, 79 (1996) 2699-2706.

[109] P. Papadopulos, A. Scholz, S. Bauer, B. Schröder, H. Oechsner, Deposition of device quality a-Si:H films with the hot-wire technique, Journal of Non-Crystalline Solids, 164-166 (1993) 87-90.

[110] E.C. Molenbroek, A.H. Mahan, A. Gallagher, Mechanisms influencing "hot-wire" deposition of hydrogenated amorphous silicon, Journal of Applied Physics, 82 (1997) 1909-1917.

[111] R.E.I. Schropp, Present status of micro- and polycrystalline silicon solar cells made by hot-wire chemical vapor deposition, Thin Solid Films, 451-452 (2004) 455-465.

[112] A.H. Mahan, R.C. Reedy, E. Iwaniczko, Q. Wang, B.P. Nelson, Y. Xu, A.C. Gallagher, H.M. Branz, R.S. Crandall, J. Yang, S. Guha, H Out-Diffusion and Device Performance in n-i-p Solar Cells Utilizing High Temperature Hot Wire a-Si:H i-Layers, MRS Proceedings, 507 (1998) 119.

Chapter 2

Experimental Details

In general hot wire chemical vapor deposition (HWCVD) and radio frequency plasma enhanced chemical vapor deposition (rf-PECVD) are most commonly used techniques for the preparation of amorphous (a-Si:H) and nanocrystalline (nc-Si:H) silicon thin films [1-9]. In the present thesis work also, these techniques have been used for the preparation of a-Si:H and nc-Si:H as well as a-Si:H/nc-Si:H superlattice structures. The microstructure of silicon thin film can be easily tuned using these techniques by varying the various deposition parameters such as substrate temperature (T_s), filament temperature (T_f), gas flow rates, rf power, process pressure (PP), etc. [10-13]. In the present chapter, the description of HWCVD and rf-PECVD techniques have been presented followed by details of the deposition parameters used for the deposition of single layer a-Si:H, nc-Si:H films and a-Si:H/nc-Si:H superlattice structures. A brief discussion of different characterization techniques, used for the study of structural and optoelectronic properties of the single and superlattice structures of Si thin films, is also presented.

2.1 Preparation of Si thin films

2.1.1 Description of Hot Wire Chemical Vapor Deposition (HWCVD) technique

In this method, the precursor gases are decomposed thermally and catalytically into different radicals with the help of a filament heated at high temperatures, generally in the range of 1600-2500 ^{o}C [4, 14-16]. As the precursor gas undergoes catalytically cracking reaction, this technique is also known as catalytic CVD or CAT-CVD [5, 14]. Various metals such as tungsten, tantalum, rhenium, molybdenum etc. can be used as filament materials [17, 18]. Of these, tungsten is the most commonly used filament [19, 20]. Using this technique, it is possible to vary the microstructures of silicon thin films ranging from pure amorphous to microcrystalline and nanocrystalline by tuning the deposition parameters such as substrate temperature, filament temperature, substrate to filament distance, gas flow rates, etc. This technique has number of advantages compared to other CVD techniques such as high deposition rates, absence of ion bombardment on the growing film surface, large area deposition and low substrate temperature, etc. [21-24].

In our lab, we have a indigenously-designed HWCVD system for the preparation of a-Si:H and nc-Si:H thin films. Different substrates including corning 1737 glass, indium tin oxide (ITO) coated glass and un-doped silicon were used for the film preparation. The substrates were heated using radiative heater placed ~5 mm above the substrate holder and the substrate temperature was measured using K-type thermocouple attached with substrate holder. Tungsten wire of 0.5 mm diameter was used as filament. Prior to deposition, chamber was evacuated to a pressure less than 10^{-6} mbar using turbo molecular pump for 4-5 hours. Highly pure (>99.99%) semiconductor grade Silane (SiH_4) and Hydrogen (H_2) were used as precursor gases for the deposition of amorphous and nanocrystalline Si thin films.

The schematic diagram of a HWCVD system is shown in the Fig 2.1 while, Fig 2.2(a) and (b) show the photograph of the whole HWCVD system and the HWCVD chamber during deposition, respectively. The system consists of two cylindrical chambers made of stainless steel (SS 304 grade) separated by a gate valve. A double wavelength pyrometer from IRCON (model MR-OR05-240) was used for the measurement of filament temperature during the deposition. The filament as well as the gas inlets are surrounded by SS gas confinement cup which facilitates the efficient dissociation of the gases. This system has also been used for the preparation of other semiconductor materials such as SiC thin films, different allotropes of carbon such as graphene, diamond like carbon and carbon nanoflakes.

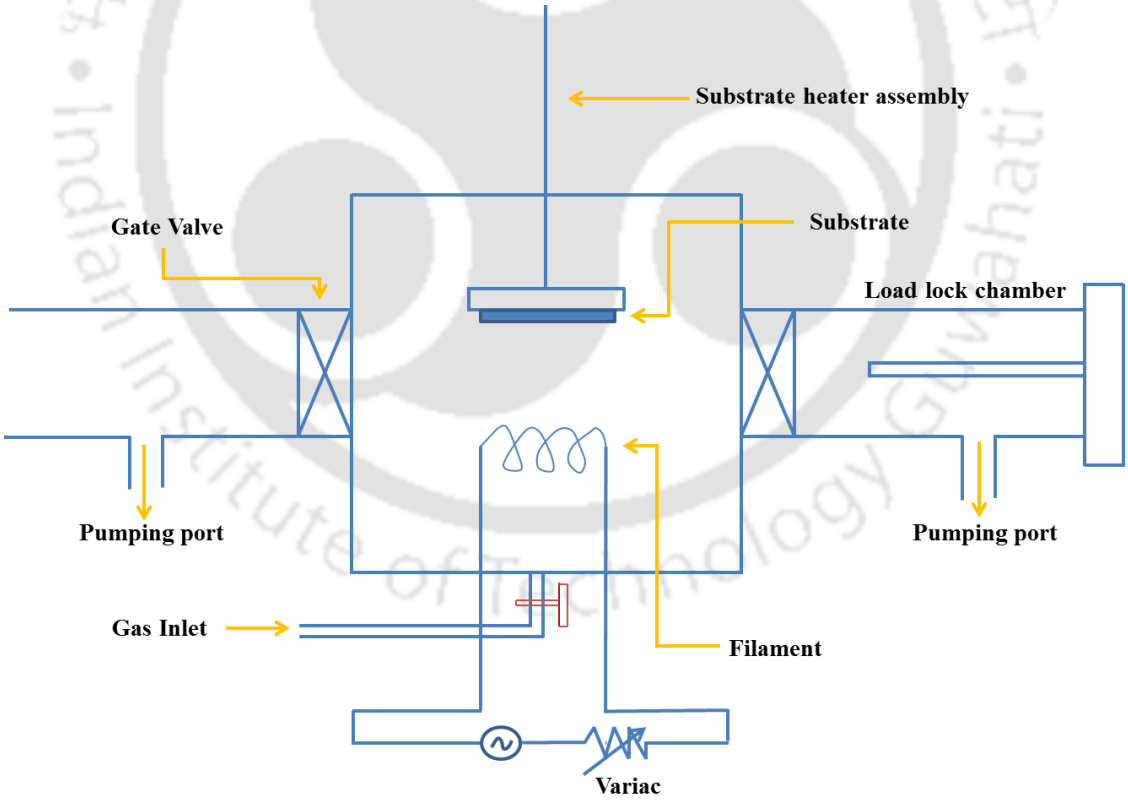

Figure 2.1: Schematic diagram of a general HWCVD system.

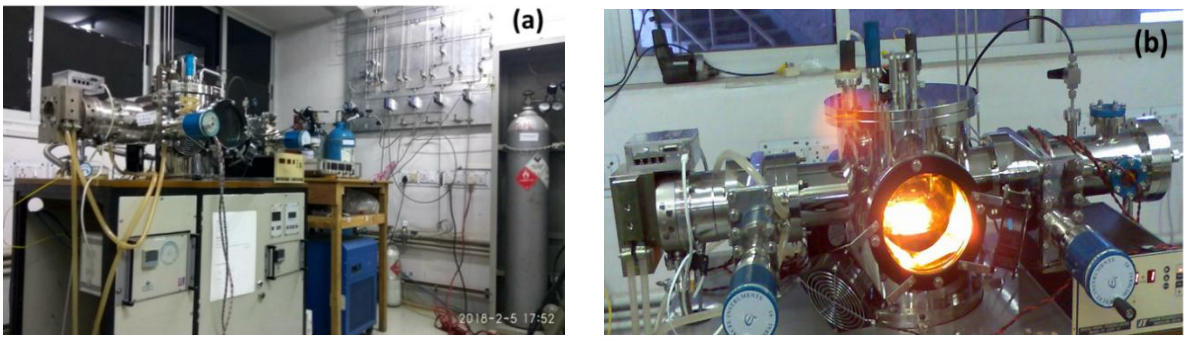

Figure 2.2: a) HWCVD system with gas manifold in our lab and b) HWCVD chamber during deposition.

Unlike, PECVD technique, where SiH_3 is the main film forming radical, in HWCVD, Si and H are the primary radicals released from the filament surface [25, 26]. The number density of SiH is two orders of magnitude lower than Si [26]. At very low chamber pressure (10^{-4} Torr), as studied by Weismann *et al.* [4], radical gas reactions are prevented resulting in poor quality films. At moderate pressure (tens of mtorr), the radical-gas reactions yield other film forming radicals like SiH_3 through the following reactions [25].

$$H + SiH_4 \rightarrow H_2 + SiH_3$$
$$Si + SiH_4 \rightarrow Si_2H_4 \rightarrow 2SiH_2$$
$$\rightarrow SiH + SiH_3$$
$$\rightarrow Si_2H_2 + H_2$$

At much higher pressure, radical-radical reaction becomes dominant and desired SiH_3 radicals are consumed before they reach the substrate.

2.1.2 Description of rf-Plasma Enhanced Chemical Vapor Deposition (rf-PECVD) technique

Plasma enhanced chemical vapor deposition (PECVD) is a widely used technique for the preparation of amorphous, nano and microcrystalline Si thin films [27]. In this technique, a silicon containing gas such as silane is dissociated into SiH_n (Si-H, Si-H_2, Si-H_3…) under

the influence of high electric field between two parallel plates, using either dc voltage or a voltage in the radio frequency domain (13.56-200 MHz). Capacitatively coupled PECVD method with radio frequency 13.56 MHz is widely opted by scientific community for preparation of device quality films and also used in industrial applications [28-31]. Figure 2.3 shows the schematic of the rf-PECVD system that we have in our lab while, Fig 2.4 shows the photograph of rf-PECVD system and the inset image shows the PECVD chamber during deposition. The system consists of high vacuum chamber connected to a gas inlet and the source for the discharge.

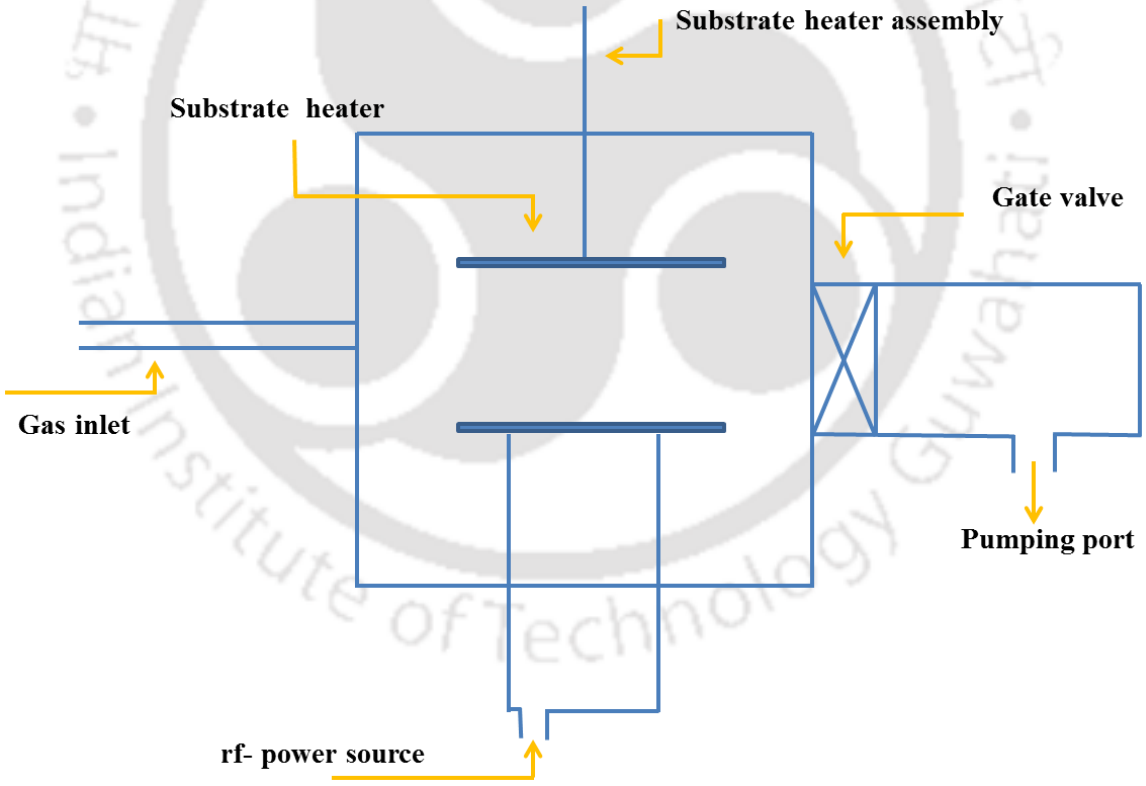

Figure 2.3: Schematic diagram of a general PECVD system.

Figure 2.4: rf-PECVD system in our lab (inset image: rf-PECVD chamber during deposition).

Highly pure (>99.99%) semiconductor grade Silane (SiH_4) and Hydrogen (H_2) were used as precursor gases for the preparation of silicon thin films. The initial event for the growth of micro, nano and amorphous silicon is the decomposition of the source gas by glow discharge plasma. These gases are dissociated into different film forming radicals by inelastic collision with the high energy electrons (about several ten electron volts) present in the plasma, followed by subsequent gas phase reactions. SiH_4 is dissociated into SiH_n ($n \leq 3$, such as SiH_3, SiH_2, SiH and H) as well as H_2 and H as shown in Fig 2.5 [32]. Hydrogen molecule is also decomposed into atomic hydrogen. Figure 2.6 shows the number densities of different radicals in steady state plasma. Among these radicals, SiH_3 is the least reactive one and has the highest concentration, irrespective of the initial formation rate and thus mainly responsible for the growth of micro and nano crystalline as well as a-Si thin films. Further, excitation of the ground state electron to the vacuum state gives rise to ionization events,

generating new electrons and ions to maintain the plasma. The plasma is confined between two parallel plates, one of which also holds the substrate. The radicals so formed undergo secondary gas phase reactions, mostly with parent SiH_4 and H_2 and form a steady state. The radicals formed in secondary gas phase reactions then get deposited on the substrate, yielding the Si thin film.

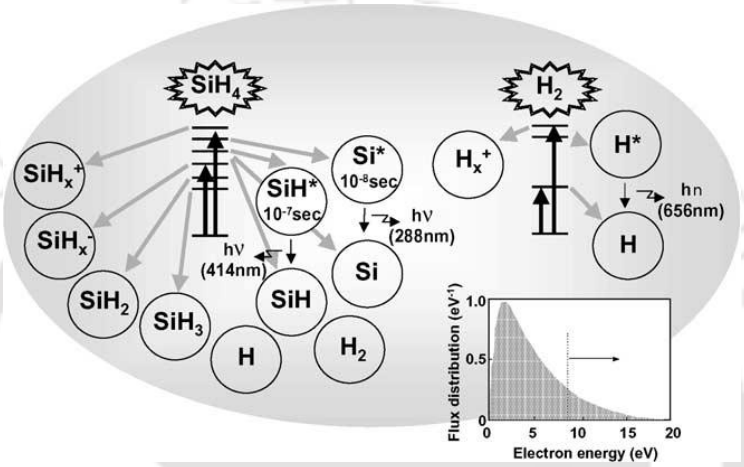

Figure 2.5: Schematic of the dissociation processes of SiH_4 and H_2 molecules under the influence of high rf-field[32] (also shown in chapter 1).

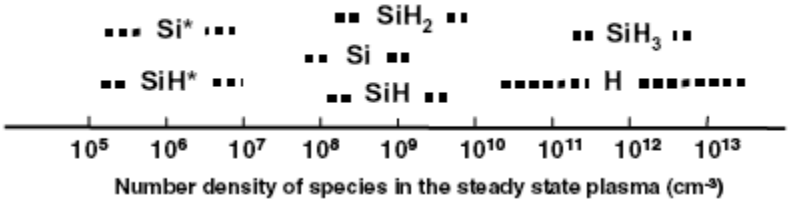

Figure 2.6: Number density of different film forming radicals in steady state plasma [32](also shown in chapter 1).

2.1.3 Preparation of a-Si:H and nc-Si:H thin films using both HWCVD and rf-PECVD techniques

As discussed in the previous chapter, the motivation behind the present thesis has been to get device quality a-Si:H and nc-Si:H films and subsequent preparation of a-Si:H/nc-Si:H

superlattice structures for various device applications. In order to achieve that, four different series of samples were prepared (using HWCVD and rf-PECVD techniques) by varying one deposition parameter at a time while keeping all the other parameter fixed; Series I: the variation of H_2 dilution (23-85%) of SiH_4 on silicon thin films prepared by HWCVD technique, Series II: the variation of rf-power (20-60 W) on silicon thin films prepared by rf-PECVD technique, Series III: the variation of H_2 dilution (50-94%) of SiH_4 on silicon thin films prepared by rf-PECVD technique, Series IV: the variation of substrate temperature (150 ºC-250 ºC) on silicon thin films prepared by rf-PECVD technique.

For series I, hydrogenated amorphous (a-Si:H) and nanocrystalline (nc-Si:H) silicon films were prepared using HWCVD technique on corning 1737 glass and ITO coated glass substrates. The films were deposited by varying the hydrogen and silane flow rates and thus hydrogen dilution [R] of silane. The hydrogen dilution [R] is defined as $[H_2]/\{[H_2] + [SiH_4]\}$, where $[H_2]$ and $[SiH_4]$ represent the flow rate of these gases. The deposition parameters like filament temperature (T_f) and substrate temperature (T_s) were kept constant at 1900 ºC and 200 ºC respectively. The other deposition parameters are listed in Table 2.1. For the TEM studies, thin films of thickness < 40 nm were also deposited on carbon coated Cu grid (Mesh 400).

Table 2.1: Deposition parameters of a-Si:H and nc-Si:H thin films prepared using HWCVD technique. (P.P is process pressure, SFR (sccm) and HFR (sccm) refer to silane and hydrogen flow rates in standard cubic centimeter per min) (Series I)

Sample No.	P.P (mbar)	SFR (sccm)	HFR (sccm)	H_2 dilution (%)[R]
HW212	0.15	10	3	23
HW219	0.02	2.7	1	27
HW211	0.10	4.8	3	38
HW214	0.19	2.6	15	85

Other series (II-IV) of samples were prepared on Corning 1737 glass and ITO coated glass substrates using rf-PECVD techniques under different deposition conditions. The deposition parameters for Si films of series (II-IV) are listed in Table 2.2-2.4, respectively.

Table 2.2: Deposition parameters for silicon thin films prepared with the variation of rf-power using rf-PECVD technique (Series II)

Sample No.	**rf power (W)**	SFR (10% in H_2) (sccm)	P.P (mbar)	t_d (mins.)	T_s (^oC)
PE81	**20**	12	0.24	45	400
PE79	**40**		0.21		
PE80	**60**		0.26		

Where, t_d=Deposition time and PP = process pressure.

Table 2.3: Deposition parameters for silicon thin films prepared with variation of H_2 dilution of silane using rf-PECVD technique (Series III)

Sample No.	**H_2 dilution (%)**	SFR (sccm)	HFR (sccm)	P.P (mbar)	t_d (mins)	rf-power (W)	T_s (^oC)
PE 59	**50**	3	3	0.21	45	50	300
PE 62	**62**		5	0.23			
PE 61	**94**		55	0.21			

Table 2.4: Deposition parameters for silicon thin films prepared with variation of T_s using rf-PECVD technique (Series IV)

Sample No.	**T_s (^oC)**	P.P (mbar)	t_d (min)	rf power (W)	SFR (sccm)	HFR (sccm)	H_2 dilution (%)
PE101	**150**	0.64	60	80	4	96	96
PE100	**200**	0.64					
PE97	**250**	0.62					

2.1.4 Preparation of a-Si:H/nc-Si:H superlattice structures using both HWCVD and rf-PECVD techniques

From the optimized deposition parameters as mentioned (Table 2.1-2.4) above, a-Si:H/nc-Si:H multilayer/superlattice structures were prepared using both HWCVD and rf-PECVD techniques. For the thick individual layers of a-Si:H and nc-Si:H in these superlattice (a-

Si:H/nc-Si:H) structures, HWCVD technique has been used whereas, for thin individual layers, rf-PECVD technique has been used.

A superlattice structure consisting of 2 and 5 periods (pair of a-Si:H and nc-Si:H together is defined as one period) of alternating a-Si:H and nc-Si:H thin films were deposited by Hot wire chemical vapor deposition technique on Corning 1737 glass and ITO coated glass substrates (thickness of both layers is kept same). The 5 periods structure had a total thickness of 700 nm (keeping the individual layer thickness equal at 70 nm) and two different 2 periods superlattice structures had thickness of individual layers as 70 nm and 175 nm respectively. In these superlattice structures, bottom layer was a-Si:H and the top layer was nc-Si:H. Pure silane (SiH_4) and hydrogen (H_2) were used as a precursor gases. The difference in the deposition parameters between the nc-Si:H and a-Si:H sub-layers are as follows: higher [R] of 85% for nc-Si:H and low [R] of 27% for a-Si:H, which resulted in different chamber pressure during deposition of two layers. The substrate and filament temperature were kept constant at 200 °C and 1900 °C respectively and other deposition parameters are same as listed in Table 2.1 (Sample no. HW214 and HW219). The deposition time for the desired thickness of individual layer was estimated from deposition rate of corresponding single layer films. The individual layer thickness of a-Si:H and nc-Si:H in the superlattice structures are listed in Table 2.5.

Table 2.5: Thickness of individual layer in a-Si:H/nc-Si:H superlattice structures

Type	nc-Si:H layer thickness (nm)	a-Si:H layer thickness (nm)	Total thickness (nm)
2 periods	175	175	700
2 periods	70	70	280
5 periods	70	70	700

As discussed in our previous chapter, one of motivations of the present thesis is the growth of silicon nanocrystallites in a-Si:H matrix with tunable optoelectronic properties and visible photoluminescence by controlling the thickness of nc-Si layer sandwiched between the a-Si:H layers. In order to achieve the above mentioned target, it was needed to prepare a very thin individual layers of a-Si:H and nc-Si:H in these superlattice structures. Since the deposition rate for the films prepared by rf-PECVD is low, therefore this technique has been used for the preparation of thin sub-layers of a-Si:H and nc-Si:H in these superlattice structures.

The superlattice structures consisting of 7 and 11 layers of alternating nc-Si:H and a-Si:H thin film were deposited on Corning 1737 glass, ITO coated glass and undoped c-Si substrates using rf-PECVD technique. In the superlattice structures, the thickness of a-Si:H layer was kept constant at 10 nm whereas, the thickness of the nc-Si:H layer was varied from 5-30 nm. The bottom and top layers were retained to be nc-Si:H in these superlattice structures. The a-Si:H and nc-Si:H sublayers were prepared by varying the hydrogen dilution [R] in silane. Higher [R] of 96% for nc-Si:H thin film and low [R] of 55% for a-Si:H thin film were used. The deposition time for the desired thickness of individual layer was estimated from deposition rate of corresponding single layer films. The deposition parameters for single layer films are listed in Table 2.6 and the deposition parameters with the layer thickness for the superlattice structures are mentioned in Table 2.7.

TABLE 2.6: Deposition parameters of single layer of a-Si:H and nc-Si:H thin films prepared using rf-PECVD technique

Type	P.P(mbar)	SFR (sccm)	HFR (sccm)	[R] (%)	rf power (W)	T_s (ºC)
a-Si:H	0.76	8	10	55	80	250
nc-Si:H	0.68	4	96	96		

Table 2.7: Deposition parameters of a-Si:H/nc-Si:H superlattice structures thin films using rf-PECVD technique

Sample No	P.P (mbar) nc-Si/a-Si	SFR (sccm) nc-Si/a-Si	HFR (sccm) nc-Si/a-Si	H_2 Dilution (%) nc-Si/a-Si	rf-power (W)	T_s (ºC)	Thickness (nm) nc-Si/a-Si (total)	No. of individual layers
PE99	0.68/0.76	4/8	96/10	96/55	80	250	5/10 (50 nm)	4 (nc-Si:H) 3 (a-Si:H)
PE115	0.68/0.76	4/8	96/10	96/55			10/10 (70 nm)	4 (nc-Si:H) 3 (a-Si:H)
PE137	0.68/0.76	4/8	96/10	96/55			20/10 (110 nm)	4 (nc-Si:H) 3 (a-Si:H)
PE138	0.68/0.76	4/8	96/10	96/55			30/10 (150 nm)	4 (nc-Si:H) 3 (a-Si:H)
PE93	0.68/0.76	4/8	96/10	96/55			20/10 (170 nm)	6 (nc-Si:H) 5 (a-Si:H)

2.2 Characterizations techniques

2.2.1 X-ray diffraction (XRD)

X-ray diffraction (XRD) is an efficient non-destructive technique used to investigate the structural properties of materials. This technique is based on the principle of diffraction (scattering) of x-ray radiation by the crystal planes. This technique is used to analyze a material for the determination of:

a) Micro-structural nature of the samples (amorphous or crystalline) and their phase identification (cubic, hexagonal etc.).

b) Mean crystallite size and unit cell parameters

c) Strain and dislocation density analysis

d) Phase transition, phase diagrams, defects etc.

In the present thesis, XRD measurements were performed using "Rigaku TTRAX-III" diffractometer with CuK_α (λ=1.54 Å) radiation in 2θ range 10-70° on the silicon thin films deposited on corning glass substrate. In this range, crystalline Si shows a sharp peaks

corresponding to (111), (220) and (311) planes near 28^o, 47^o and 56^o respectively. Whereas, in case of amorphous Si, the peak broadens and gives the characteristic amorphous hump in the XRD pattern. When the films contain nanocrystallites embedded in amorphous matrix, peaks corresponding to crystalline silicon appear superimposed on the broad amorphous pattern.

2.2.2 Raman Spectroscopy

Raman spectroscopy is a powerful tool to study the vibrational modes in the material for understanding the crystal structures, composition and many other fundamental properties. In the present thesis, Raman spectra of all the samples were recorded using "Horiba JY LabRam HR800", with an excitation wavelength of 488 nm with the Ar laser source and 632.8 nm with the He-Ne laser source for the films deposited on corning 1737 glass substrate. While recording the Raman spectra, the excitation laser radiation was tightly focused on the surface of the sample to a spot size of $\leq 1\mu m$. With the change in laser power density, the structural properties of Si thin changes [33], therefore, keeping that in mind all the Raman spectra were recorded at the lowest laser power density. For 488 nm laser source, the laser power density was kept at 127 kW/cm^2 whereas, for 632.8 nm laser source, the laser power density was kept at 171 kW/cm^2. The resolution and the recorded spectral range of Raman shifts were 1 and 300-600 cm^{-1} respectively.

In Raman spectra, transverse optic (TO) mode of phonon vibration for a-Si and c-Si appear at 480 cm^{-1} and at 520 cm^{-1} respectively. For nanocrystallites embedded amorphous Si, another peak centered at 495 cm^{-1} appears due to the bond dilation at the grain boundaries as a results of partial crystallization/improved ordering in these films. The crystalline peak also shifts from 520 cm^{-1} towards lower value in case of nanocrystallites embedded amorphous

Si due to the size limitation of the crystallites, smaller the crystallite size, larger is the shift. Hence the crystallite size was calculated from the shift of crystalline peak from 520 cm^{-1}. He *et al.* [34] have suggested the relation between the shift and crystallite size as

$$d_{\text{Raman}} = 2\pi\sqrt{\frac{B}{\Delta\omega}} \qquad \ldots\ldots\ldots \quad (2.1)$$

where, Δ ω is the peak shift for the nanocrystalline Si as compared to that of c-Si and B= 2.0 cm^{-1} nm^2 [31].

For the calculation of total crystalline (X_c) and nanocrystalline (X_{nc}) volume fraction in nc-Si thin films, the Raman spectra was deconvoluted into three different components: two Gaussian (480 cm^{-1} and 495 cm^{-1}) and one lorentzian (511-520 cm^{-1}). One such deconvoluted Raman spectra is shown in Fig 2.7.

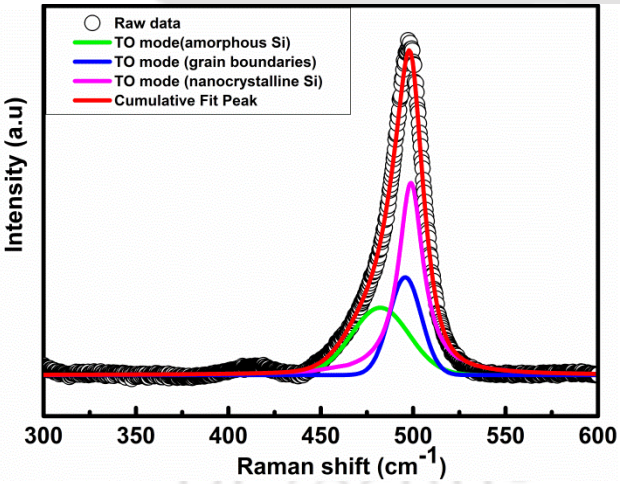

Figure 2.7: Deconvoluted Raman spectra of Si thin film.

The total crystalline volume fraction *(X_c)* was estimated as the fraction of integrated intensity under grain boundary peak and nanocrystalline peak with respect to the total intensity under all the TO peaks[34].

$$X_c = \frac{I_{nc} + I_{int}}{I_{nc} + I_{int} + I_{am}} \quad \ldots\ldots\ldots\ldots \quad (2.2)$$

Where I_{am}, I_{int} and I_{nc} are the integrated intensities under amorphous, grain boundaries and nanocrystalline TO peaks respectively and the nanocrystalline volume fraction (X_{nc}) was estimated by the following relation:

$$X_{nc} = \frac{I_{nc}}{I_{nc} + I_{int} + I_{am}} \quad \ldots\ldots\ldots\ldots \quad (2.3)$$

2.2.3 Transmission electron microscopy

Transmission electron microscopy, "JEOL JEM 2100" was used to study the microstructure properties of silicon thin films. For these measurements, the samples were prepared on carbon coated Cu mesh TEM grid (Mesh 400). The thickness of the films was kept below 40 nm. In this measurement, the electron beam was accelerated with the voltage of 200 KV. In case of HRTEM, spot size was varied from 20-200 nm and the image was taken at a magnification of 10^5 to 10^6 X. During the observation of selected area electron diffraction (SAED) pattern, a field limited aperture was inserted. From the SAED pattern, the inter-planar spacing was calculated using "Gatan digital micrograph" software.

2.2.4 Field emission scanning electron microscopy

Field emission scanning electron microscopy (FESEM, model: ∑IGMA ZEISS) was used for the study of surface morphology of silicon thin films. Before mounting the sample for the analysis, the thin films were coated with thin layer of gold of thickness ~2-5 nm via sputtering in order to avoid the charging effect during the measurements. FESEM was operated with an accelerating voltage of 2 to 4 KeV.

2.2.5 Stylus profilometer

For the thickness measurement of the silicon thin films, stylus profilometer (model: Veeco, Dektak 150) has been used. It is capable to scan area of tens of millimeter with vertical range starting from a few nanometers up to hundreds of microns. It is used to measure height difference on the sample surface. Therefore before deposition of Si films, a part of the substrate was covered with a mask and the difference between the height of covered and uncovered surfaces were measured as the thickness of the films.

2.2.6 UV-Vis NIR transmission Spectroscopy

Ultraviolet-Visible Near-Infrared (UV-Vis-NIR) spectroscopy is one of the important techniques to measure the transmission and absorbance of the materials. The transmission spectra of the silicon thin films were performed using "Shimadzu UV3101PC" dual beam spectrometer in the transmission mode in the range of 200-3000 nm for the films deposited corning 1737 glass substrate. The recorded spectrum indicates the fraction of light transmitted by the films and the absorption due to electronic transition from the ground state to an excited state. Interference fringes are observed in the transparent to medium absorbing range due to multiple reflections from the different layers of the films. Using Swanepoel's method [35], thickness and the other optical constant like bandgap, absorption coefficient and refractive index etc. of the films were deduced. For the estimation of the band gap following Eq. has been used:

$$\alpha h\nu = C(h\nu - E_g)^p \qquad \ldots\ldots\ldots\ldots\ldots \quad 2.4$$

where $h\nu$ is the energy of the incident light photon, α is the absorption coefficient, E_g is the energy band gap and C is a constant independent of ν. The value of the exponent p is 1/2 and 2 for a direct gap and indirect gap transition, respectively.

2.2.7 Photoluminescence

Photoluminescence spectroscopy is a non-destructive method to probe the electronic structure of materials. The intensity and spectral content of the emitted radiation is a direct measure of various important material properties, including band gap, defects, and impurity and recombination mechanisms. It is a phenomenon in which a photon having energy greater than band gap energy is absorbed thereby raising an electron from valence band to conduction band. In this process of photo excitation, the electron return to the lower energy states accompanied by emission of photons in the energy range of visible or near infrared. In the present work, a standard set-up was used for photoluminescence measurements with which PL spectra were recorded using a diode pumped solid state (DPSS) laser at an excitation wavelength of 405 nm and at laser power of 30 mW.

2.2.8 Electrical transport measurements

Dark and photo conductivity of single layer silicon thin films were measured by two probe method in a diffusion pump based high (10^{-5} mbar) vacuum system. The samples were mounted on stainless steel sample holder which was attached to the heater for measuring the temperature dependent conductivity. The temperature of the films was measured with the help of a platinum resistance thermometer (PT-100) and a 6 ½ digit multimeter (Agilent, model: 34401A). Keithley 2450 source meter was used for the *IV* measurements.

Dark and photo conductivity measurements were conducted in coplanar geometry using silver paste (high purity of 99.99%) as an electrode for the films deposited on corning 1737 glass substrate. For the transverse geometry, the thin films deposited on ITO coated glass substrate have been used.

In case of coplanar geometry, the conductivity of the thin film is given by,

$$\sigma = \frac{Iw}{Vlt} \quad \ldots\ldots\ldots\ldots\ldots\ldots \quad 2.5$$

where, I is the measured current, V is the applied voltage, w is the separation between the electrodes, l is the length of the electrodes and t is the thickness of the thin films. Whereas, for the transverse geometry the conductivity of the films is given by,

$$\sigma = \frac{Iw}{VA} \quad \ldots\ldots\ldots\ldots\ldots\ldots\ldots\ldots\ldots\ldots \quad 2.6$$

where, I is the measured current, V is the applied voltage, w is the separation between the electrode which will be the thickness of the film for this geometry and A is the area of the electrode. Using the above two equations the conductivity of silicon thin films in both the geometry has been estimated.

The activation energy (E_a) of the dark conductivity is a good measure of the energy difference between the Fermi level and the conduction band edge for the electron transport. The E_a was determined from temperature dependent conductivity measurements using Arrhenius plot. The relation between dark conductivity and E_a is given by,

$$\sigma = \sigma_o \exp\left(\frac{-E_a}{K_B T}\right) \quad \ldots\ldots\ldots\ldots\ldots\ldots\ldots \quad 2.7$$

where, σ_o is conductivity pre-factor, T is absolute temperature (in Kelvin) and K_B is the Boltzmann's constant.

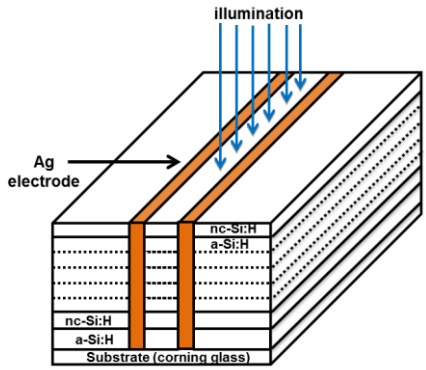

Figure. 2.8: Schematic diagram of a-Si:H/nc-Si:H superlattice structure and electrode geometry.

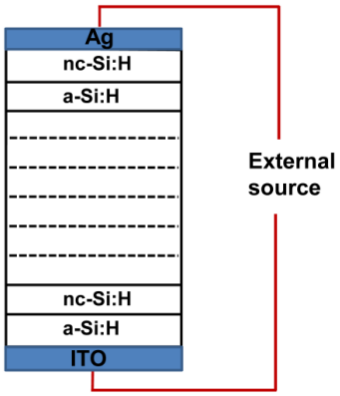

Figure 2.9: Schematic of the electrode geometry used to perform SCLC measurements in a-Si:H/nc-Si:H superlattice structures.

The electrical transport properties across the superlattice structures of a-Si:H and nc-Si:H thin films was measured in both coplanar and transverse geometry. To ensure the contact of the electrode with all the layers, the superlattice structures were scratched before making the electrode. Figure 2.8 and 2.9 show the sample structure and contact electrodes in both coplanar and transverse geometry respectively. For the transient measurements, the current was measured as a function of time both during illumination ON and after illumination was turned OFF.

2.3 References

[1] B.P. Swain, B.S. Swain, N.M. Hwang, A comparative chemical network study of HWCVD deposited amorphous silicon and carbon based alloys thin films, Journal of Alloys and Compounds, 588 (2014) 343-347.

[2] D. Soler, M. Fonrodona, C. Voz, J. Bertomeu, J. Andreu, Thin silicon films ranging from amorphous to nanocrystalline obtained by hot-wire CVD, Thin Solid Films, 383 (2001) 189-191.

[3] A.H. Mahan, J. Carapella, B.P. Nelson, R.S. Crandall, I. Balberg, Deposition of device quality, low H content amorphous silicon, Journal of Applied Physics, 69 (1991) 6728-6730.

[4] H. Wiesmann, A.K. Ghosh, T. McMahon, M. Strongin, a-Si : H produced by high-temperature thermal decomposition of silane, Journal of Applied Physics, 50 (1979) 3752-3754.

[5] H. Matsumura, Study on catalytic chemical vapor deposition method to prepare hydrogenated amorphous silicon, Journal of Applied Physics, 65 (1989) 4396-4402.

[6] G. Dushaq, A. Nayfeh, M. Rasras, Tuning the optical properties of RF-PECVD grown μc-Si:H thin films using different hydrogen flow rate, Superlattices and Microstructures, 107 (2017) 172-177.

[7] P. Roca i Cabarrocas, A. Fontcuberta i Morral, Y. Poissant, Growth and optoelectronic properties of polymorphous silicon thin films, Thin Solid Films, 403-404 (2002) 39-46.

[8] M. Kondo, A. Matsuda, Novel aspects in thin film silicon solar cells–amorphous, microcrystalline and nanocrystalline silicon, Thin Solid Films, 457 (2004) 97-102.

[9] U. Kroll, J. Meier, A. Shah, S. Mikhailov, J. Weber, Hydrogen in amorphous and microcrystalline silicon films prepared by hydrogen dilution, Journal of Applied Physics, 80 (1996) 4971-4975.

[10] J. Gope, S. Kumar, A. Parashar, P.N. Dixit, C.M.S. Rauthan, O.S. Panwar, D.N. Patel, S.C. Agarwal, Amorphous and nanocrystalline silicon made by varying deposition pressure in PECVD process, Journal of Non-Crystalline Solids, 355 (2009) 2228-2232.

[11] P. Chaudhuri, R. Meaudre, C. Longeaud, Argon dilution of silane as an alternative to hydrogen dilution for stable and high efficiency silicon thin films solar cells, Journal of Non-Crystalline Solids, 338-340 (2004) 690-693.

[12] S. Kumar, P.N. Dixit, C.M.S. Rauthan, A. Parashar, J. Gope, Effect of Power on the Growth of Nanocrystalline Silicon films., 20 (2008) 335215.

[13] R. Ambrosio, M. Moreno, A. Torres, A. Carrillo, I. Vivaldo, I. Cosme, A. Heredia, Deposition and characterization of amorphous silicon with embedded nanocrystals and microcrystalline silicon for thin film solar cells, Journal of Alloys and Compounds, 643 (2015) S27-S32.

[14] H. Matsumura, H. Tachibana, Amorphous silicon produced by a new thermal chemical vapor deposition method using intermediate species SiF2, Applied Physics Letters, 47 (1985) 833-835.

[15] P. Gogoi, H.S. Jha, P. Agarwal, Variation of microstructure and transport properties with filament temperature of HWCVD prepared silicon thin films, Thin Solid Films, 519 (2011) 4506-4510.

[16] P. Brogueira, J.P. Conde, S. Arekat, V. Chu, Amorphous and microcrystalline silicon films deposited by hot-wire chemical vapor deposition at filament temperatures between 1500 and 1900°C, Journal of Applied Physics, 79 (1996) 8748-8760.

[17] H.L. Duan, S.F. Bent, The influence of filament material on radical production in hot wire chemical vapor deposition of a-Si:H, Thin Solid Films, 485 (2005) 126-134.

[18] K. Brühne, M.B. Schubert, C. Köhler, J.H. Werner, Nanocrystalline silicon from hot-wire deposition — a photovoltaic material?, Thin Solid Films, 395 (2001) 163-168.

[19] J. Doyle, R. Robertson, G.H. Lin, M.Z. He, A. Gallagher, Production of high-quality amorphous silicon films by evaporative silane surface decomposition, Journal of Applied Physics, 64 (1988) 3215-3223.

[20] C. Horbach, W. Beyer, H. Wagner, Investigation of the precursors of a-Si:H films produced by decomposition of silane on hot tungsten surfaces, Journal of Non-Crystalline Solids, 137-138 (1991) 661-664.

[21] A.H. Mahan, Y. Xu, B.P. Nelson, R.S. Crandall, J.D. Cohen, K.C. Palinginis, A.C. Gallagher, Saturated defect densities of hydrogenated amorphous silicon grown by hot-wire chemical vapor deposition at rates up to 150 Å/s, Applied Physics Letters, 78 (2001) 3788-3790.

[22] B.P. Nelson, Y. Xu, A.H. Mahan, D.L. Williamson, R.S. Crandal, Hydrogenated Amorphous Silicon Grown by Hot-Wire CVD at Deposition Rates up to 1 μm/minute, MRS Proceedings, 609 (2011) A22.28.

[23] A.H. Mahan, Y. Xu, D.L. Williamson, W. Beyer, J.D. Perkins, M. Vanecek, L.M. Gedvilas, B.P. Nelson, Structural properties of hot wire a-Si:H films deposited at rates in excess of 100 Å/s, Journal of Applied Physics, 90 (2001) 5038-5047.

[24] B.P. Nelson, R.S. Crandall, E. Iwaniczko, A.H. Mahan, Q. Wang, Y. Xu, W. Gao, Low Hydrogen Content, High Quality Hydrogenated Amorphous Silicon Grown by Hot-Wire CVD, MRS Proceedings, 557 (2011) 97.

[25] A. Gallagher, Some physics and chemistry of hot-wire deposition, Thin Solid Films, 395 (2001) 25-28.

[26] Y. Nozaki, K. Kongo, T. Miyazaki, M. Kitazoe, K. Horii, H. Umemoto, A. Masuda, H. Matsumura, Identification of Si and SiH in catalytic chemical vapor deposition of SiH4 by laser induced fluorescence spectroscopy, Journal of Applied Physics, 88 (2000) 5437-5443.

[27] R.A. Street, Hydrogenated Amorphous Silicon, Cambridge University Press, , (1992).

[28] J.H. Yoon, Argon-plasma-induced growth of crystalline grains in microcrystalline silicon: Formation mechanism of grains, Journal of Non-Crystalline Solids, 353 (2007) 4223-4226.

[29] S. Alexandrova, P. Danesh, I.A. Maslyanitsyn, SHG and AFM study of PECVD a-Si:H films, Vacuum, 69 (2002) 391-394.

[30] P.P. Ray, N. Dutta Gupta, P. Chaudhuri, D.L. Williamson, S. Vignoli, C. Longeaud, Properties of Si:H thin films deposited by rf-PECVD of silane–argon mixtures with variation of the plasma condition, Journal of Non-Crystalline Solids, 299-302 (2002) 123-127.

[31] Y. He, C. Yin, G. Cheng, L. Wang, X. Liu, G.Y. Hu, The structure and properties of nanosize crystalline silicon films, Journal of Applied Physics, 75 (1994) 797-803.

[32] A. Matsuda, Microcrystalline silicon.: Growth and device application, Journal of Non-Crystalline Solids, 338-340 (2004) 1-12.

[33] A. Yadav, P. Agarwal, Laser Induced Selective Crystallization of Amorphous Silicon Thin Film for Device Applications, Materials Today: Proceedings, 4 (2017) 12722-12725.

[34] S. Veprek, F.A. Sarott, Z. Iqbal, Effect of grain boundaries on the Raman spectra, optical absorption, and elastic light scattering in nanometer-sized crystalline silicon, Physical Review B, 36 (1987) 3344-3350.

[35] R. Swanepoel, Determination of the thickness and optical constants of amorphous silicon, Journal of Physics E: Scientific Instruments, 16 (1983) 1214.

Chapter 3

Structural and optoelectronic properties of a-Si:H and nc-Si:H thin films prepared by HWCVD and rf-PECVD Techniques

Among the various semiconductor thin films, hydrogenated amorphous (a-Si:H) and nanocrystalline silicon (nc-Si:H) films have much more potential for fabrication of large area thin film based solar cell, thin film transistors and other optoelectronics devices [1-8]. The disorder in a-Si:H material, which results in defects that act as recombination centers impending the transport of photo-generated carrier is the major drawback of a-Si:H thin films [9]. In recent years, nc-Si:H thin film have attracted considerable attention because of its superior electronic properties compared to a-Si:H along with better stability [10-14]. Over the last few years, chemical vapour deposition (CVD) techniques like plasma spray [15], thermal spray [16, 17], very high frequency plasma enhanced CVD [18-20], radio frequency plasma enhanced CVD (rf-PECVD) [21-23], electron cyclotron resonance plasma CVD [24, 25] and hot wire CVD (HWCVD) [26-29] are most widely used techniques for the preparation of silicon thin films. Among these techniques, HWCVD and rf-PECVD become the most fascinating techniques for the preparation of silicon thin films as compared

to other CVD techniques. The advantage of these techniques are; high quality films deposited uniformly over large area, low operation temperatures, high deposition rates and the optoelectronic properties of Si thin films can be easily tuned by varying various deposition parameters. In this Chapter, detail studies on the influence of deposition parameters on the structural and optoelectronics properties of silicon thin films prepared using both HWCVD and rf-PECVD techniques have been presented. The motivation behind this Chapter is to optimize the deposition parameter in order to get a device quality a-Si:H and nc-Si:H thin films using both the techniques.

3.1 Measurement Details

Four different series of samples were prepared using HWCVD and rf-PECVD techniques by varying one deposition parameter at a time while keeping all the other deposition parameter fixed. For series I, Si thin films were prepared using HWCVD technique with the variation of H_2 dilution of silane on corning 1737 glass and ITO coated glass substrates. Whereas, the other three series of samples were prepared using rf-PECVD technique with the variation of rf-power (Series II), variation of H_2 dilution of silane (Series III) and variation of substrate temperature (Series IV) on corning 1737 glass and ITO coated glass substrates. The other deposition parameters for these films of Series I-IV are mentioned in detail in Table 2.1-2.4 of Chapter 2, respectively. The microstructural properties of silicon thin films were studied using Field Emission Scanning Electron Microscopy (FESEM), X-ray diffraction (XRD), Raman scattering spectroscopy and transmission electron microscopy (TEM). The optoelectronic properties of these films were studied using UV-Vis-NIR transmission spectroscopy and *IV* measurement in coplanar geometry using silver paste as electrodes.

3.2 The effect of variation of H_2 dilution of SiH_4 on silicon thin films prepared using HWCVD technique (Series I)

3.2.1 Structural properties

3.2.1.1 X-ray Diffraction

Figure 3.1 shows the XRD pattern of Si thin films prepared at different hydrogen dilution of silane [R] using CuKα radiation (λ=1.54 Å) in scanning range from 10º to 70º. It has been observed that at low [R], the films were amorphous in nature with broad peak around 28º, while nanocrystallinity developed with high H_2 dilution, as sharp peaks corresponding to (111), (220) and (311) planes of crystalline silicon appeared. We observed a strong peak occurring at 2Θ=28º and less intense peak at 2Θ=45º and 2Θ=56º. This results indicate that the crystallites in the films have preferable orientation in <111> direction at higher [R].

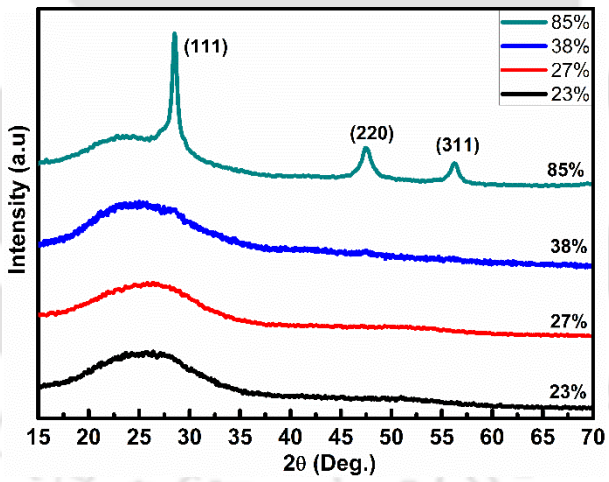

Figure 3.1: The X-ray diffraction pattern of Si thin films prepared at different H_2 dilution of silane.

3.2.1.2 Raman Spectroscopy

Figure 3.2 shows the Raman scattering spectra of the Si thin films prepared at different [R]. The Raman spectra were recorded using "Ar-ion laser" with excitation wavelength, 488 nm, in the scanning range of 300-600 cm^{-1} and at laser power density of 127 kW/cm^2. The films

prepared at low [R] ([R] ≤ 27%) show the broad peak centered at 480 cm^{-1} corresponding to the transverse optic mode (TO) of amorphous silicon, whereas films prepared at higher [R] (>27%) show sharp peak near about 520 cm^{-1} corresponding to TO mode of phonon vibration of c-Si. In order to determine the nanocrystalline (X_{nc}) and total crystalline (X_c) volume fraction of the films prepared at higher [R], the Raman peaks were de-convoluted in three components two Gaussian (480 cm^{-1} and 495 cm^{-1} corresponding to TO mode of a-Si:H and grain boundaries respectively) and one Lorentzian (511 cm^{-1} corresponding to nc-Si) [30]. The de-convoluted spectra of the films prepared at [R] = 38% and [R] = 85% are shown in Fig. 3.3 (a,b). The integrated intensity for all the three peaks was considered and using Eq. 2.2 & 2.3 as mentioned in Chapter 2, the values of X_c(%) and X_{nc}(%) were estimated.

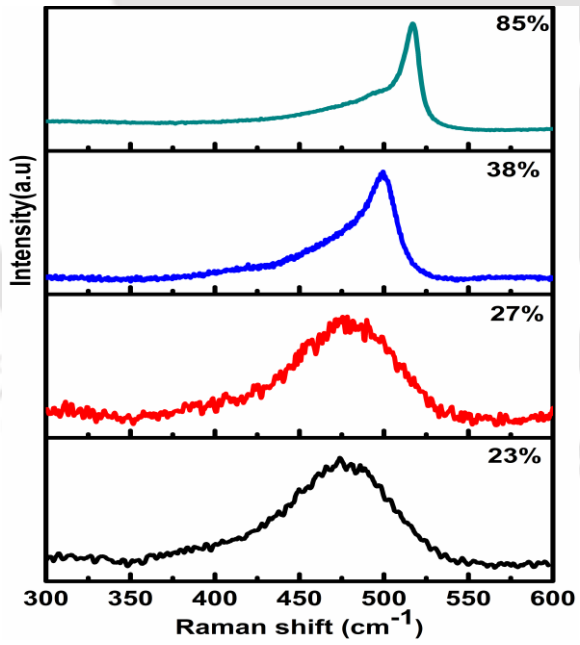

Figure 3.2: Raman scattering spectra of Si thin films at different H_2 dilution of silane.

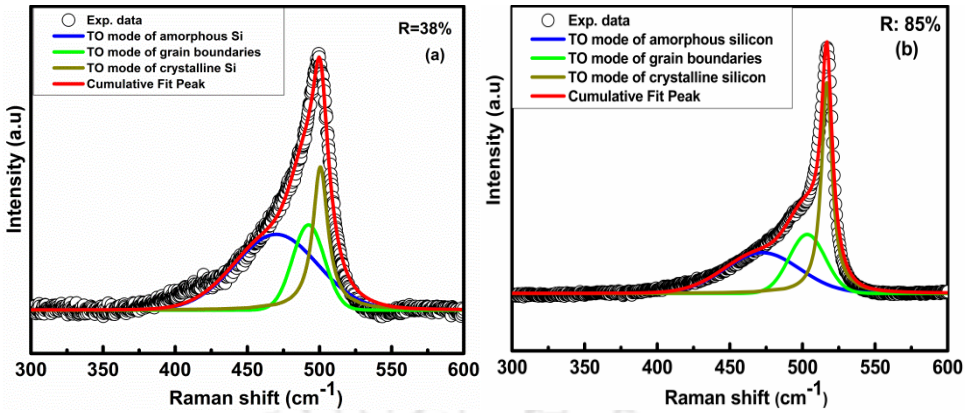

Figure 3.3: Deconvoluted Raman spectra of nc-Si:H prepared at (a) [R]= 38% and (b) [R]= 85% H_2 dilution.

The values of X_c(%) and X_{nc}(%) are listed in Table 3.1, it was observed that with increase in [R], X_c(%) and X_{nc}(%) were increased. The crystallite size for these films was also estimated using Eq. 2.1 as mentioned in Chapter 2. For [R]=38% and [R]=85% the size of the Si nanocrystals was found to be ~2 nm and ~4 nm respectively. The observed shift in the Raman peak position from 480 cm^{-1} towards 520 cm^{-1} for the sample prepared at [R]= 38% could also be due to laser induced crystallization while doing the Raman measurement as discussed in Chapter 4, since in XRD no peak corresponding to c-Si appeared for this film prepared at [R]=38%.

Table 3.1: Variation of X_{nc}(%) and X_c(%) with the variation of Hydrogen dilution of Silane.

Sample No.	H_2 dilution (%)	X_{nc} (%)	X_c (%)
HW 212	23	0	0
HW219	27	0	0
HW211	38	26	48
HW214	85	39	64

3.2.1.3 Transmission Electron Microscopy

Figure 3.4 (a) and 3.4 (b) show the selected area diffraction (SAD) pattern of a-Si:H and nc-Si:H thin films prepared at [R]= 27% and [R]= 85% respectively. The diffused ring

confirms the amorphous nature at low [R] of 27% (Fig 3.4(a)). Whereas, at higher [R] of 85%, the diffraction pattern becomes sharper with the appearance of bright spots on the rings (Fig 3.4(b)).

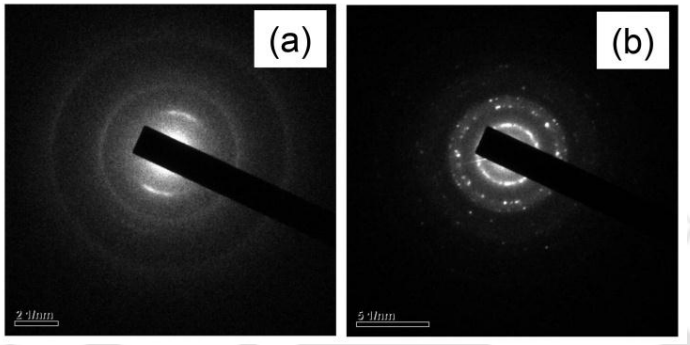

Figure 3.4: SAD pattern of (a) a-Si:H ([R]: 27%) and (b) nc-Si:H ([R]: 85%) thin films

3.2.1.4 Field Emission Scanning Electron Microscopy

Figure 3.5 (a-d) shows the FESEM image of all the films prepared at different [R]. It was observe that the thin film prepared at low [R] show smooth surface with the small grains whereas, the thin films prepared at higher [R] of 85%, the film show the presence of dispersed as well as packed grains.

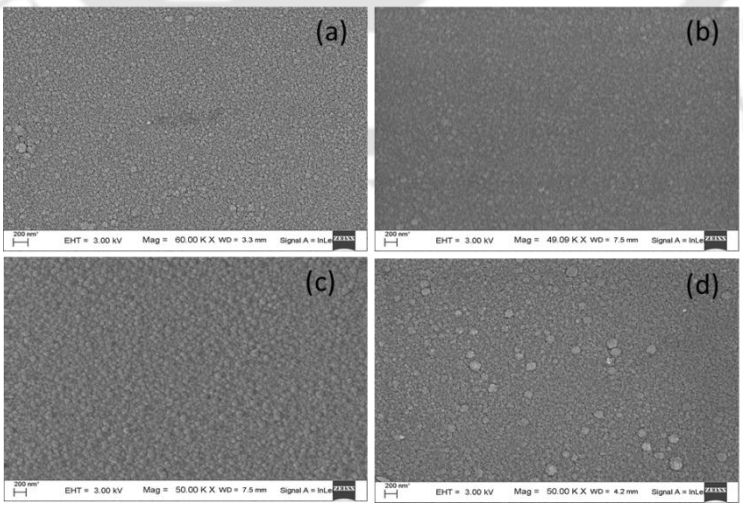

Figure 3.5: FESEM images of Si thin films at different [R] (a) 23%, (b) 27%, (c) 38% and (d) 85%.

3.2.2 Optical properties

The UV-Vis-NIR transmission spectra of these films are shown in Fig 3.6. The thickness of these films was estimated using both UV-Vis-NIR transmission spectra [31] and surface profilometer. The estimated thickness from UV-Vis-NIR transmission spectra and surface profilometer are listed in Table 3.2. The deposition rates for these films is quite high on an average 10 Å/sec, however it did not follow any trend with the variation in [R]. The band gap (E_g) of these films was calculated by plotting $\sqrt{\alpha h\nu}$ vs $h\nu$ (Fig. 3.7) and the estimated band gap for these films are listed in Table 3.2. There is not much variation in band gap of these films prepared at different [R], however with increase in [R] the band gap of these films was found to increase. The higher band gap for the films prepared at higher [R] could be due to quantum size effect, as the size of the Si nanocrytals for these films was found to be ~4 nm as estimated from Raman spectra.

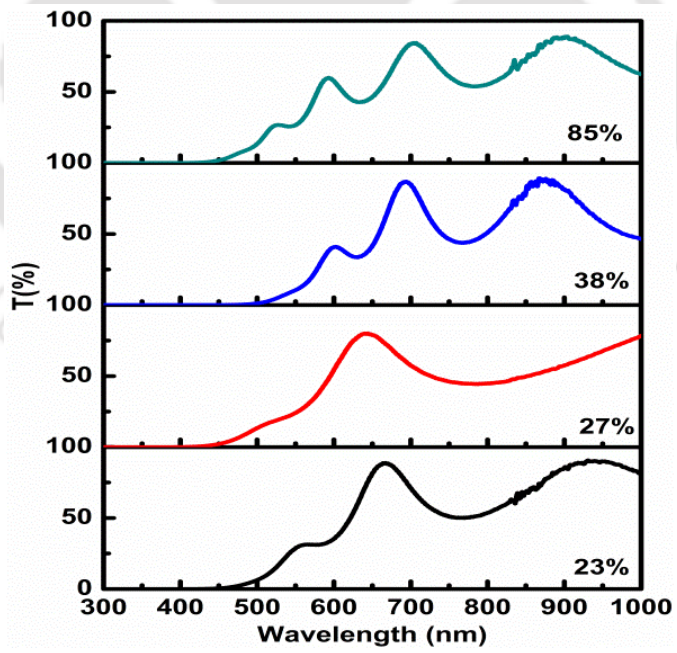

Figure 3.6: UV-Vis-NIR transmission spectra for the Si thin films prepared at different [R].

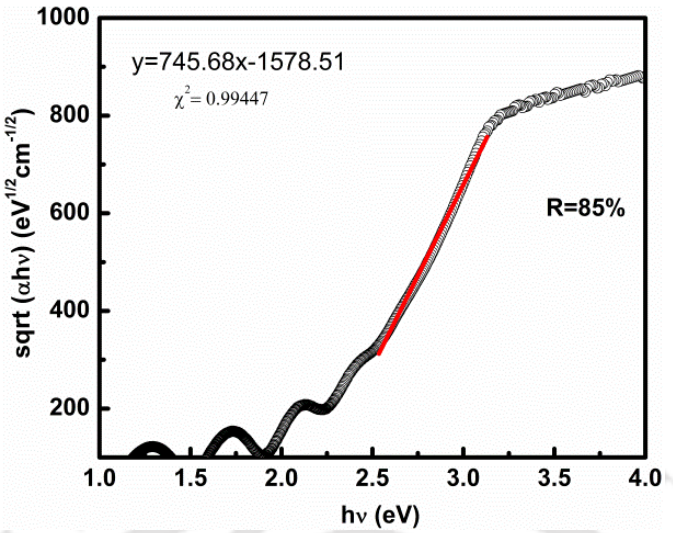

Figure 3.7: $\sqrt{\alpha h\nu}$ *vs* $h\nu$ *curve for Si film prepared at [R]=85%.*

Table 3.2: Thickness, deposition rate (r_d) and optical band gap (E_g) for the films as estimated from UV-Vis-NIR transmission spectra along with the films thickness (t) measured using surface profilometer.

Sample No.	[R] (%)	t (nm) (UV-Vis-NIR Transmission spectra)	t (nm) (Surface profilometer)	E_g (eV)	r_d (Å/s)
HW212	23	-	180	1.89	6.0
HW219	27	-	160	1.90	5.3
HW211	38	280	250	1.95	8.3
HW214	85	445	410	2.10	13.6

3.2.3 Electrical properties

The electrical characterization of these films was performed in coplanar geometry using Ag paste as electrodes. Keithley 2450 source meter was used for *I-V* measurements. For the measurements of photocurrent, 100 W halogen bulb was used. Figure 3.8 shows the dark (σ_d) and photo conductivity (σ_{ph}) of the films prepared at different [R] at room temperature (RT) after annealing these films at 200ºC. The films prepared at low [R] show high photosensitivity (σ_{ph}/σ_d) of ~4 orders of magnitude, whereas with increase in [R], the photosensitivity decreases to less than 1 order of magnitude. These results indicate that the

films deposited at higher [R] get structurally modified which might have resulted in change of dark as well as photoconductivity. These observations further strengthen our XRD and Raman results.

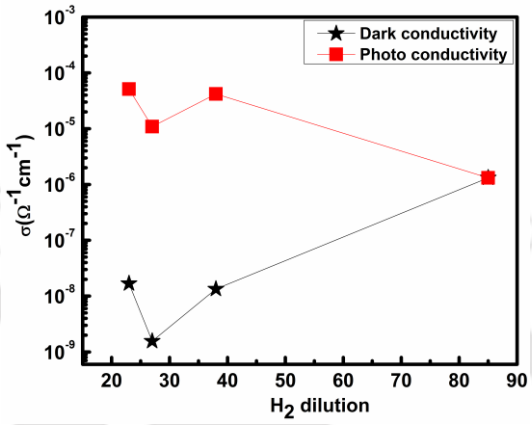

Figure 3.8: Dark and photo conductivity of the Si thin films at different [R].

These results indicate that with increase in H_2 dilution of silane the crystallite size as well as total crystalline volume fraction of Si thin films increases, which may result in change of structural and optoelectronic properties of these films. As H_2 dilution increases the number of atomic H_2 increases in the gas mixture which helps in the full surface coverage and thus facilitates the surface diffusion of the film forming precursors like SiH_3, SiH_2, SiH and Si. These absorbed radicals find energetically favorable sites leading to improvement in order and also the growth of crystallites. The excess atomic hydrogen also helps in etching and breaking of weak Si-Si bonds and hence resulting in the formation of strong Si-Si bonds. These atomic hydrogen not only acts on the top surface of the films but it also penetrate deeper into film surface where it helps in the formation of ordered structure by compensation of dangling bonds, breaking of the weak bonds as well as the reconstruction of strong bonds and the strain relaxation which may further result in structural ordering of silicon thin films.

3.3 The effect of variation of rf-power on silicon thin films prepared using rf-PECVD technique (Series II)

Deposition parameter is an important factor affecting the microstructure of the silicon thin films. Therefore, in the following sections, we have studied in detail the effect of variation of deposition parameters; rf-power, H_2 dilution and substrate temperature, on the microstructural properties of silicon thin films prepared using rf-PECVD technique. In this section, the silicon thin films were prepared with the variation of rf-power from 20-60W (series II), while keeping the other deposition parameter fixed.

3.3.1 Structural properties

3.3.1.1 X-ray Diffraction

Figure 3.9 shows the XRD pattern of all the films prepared at different rf power, recorded using CuKα radiation (λ= 1.54 Å) in scanning range from 10º to 70º. All the films show broad peak at 28º which indicate that the films are amorphous in nature.

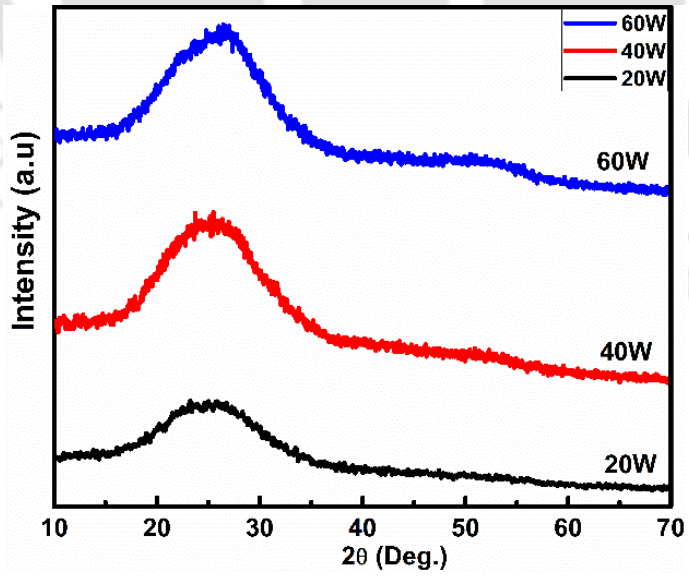

Figure 3.9: XRD pattern of Si thin films prepared at different rf-power.

3.3.1.2 Raman Spectroscopy

Figure 3.10 shows the Raman spectra of the Si thin films prepared at different rf-power. The Raman spectra were recorded using "Ar-ion laser" with an excitation wavelength, 488 nm, in the scanning range of 300-600 cm^{-1} and at laser power density of 127 kW/cm^2. A broad peak centered at 480 cm^{-1} corresponding to the transverse optic mode (TO) of amorphous silicon is observed for all the films prepared at different rf-power.

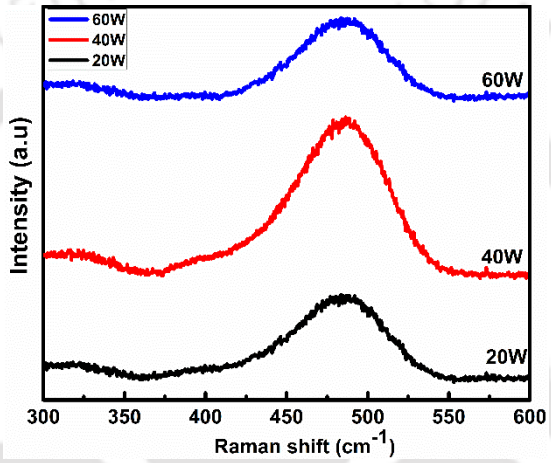

Figure 3.10: Raman spectra of Si thin films prepared at different rf power.

3.3.2 Optical properties

The UV-Vis-NIR transmission spectra of these films are shown in Fig 3.11. The thickness of these films was measured using both UV-Vis-NIR transmission spectra and surface profilometer. The estimated thickness of these films using both the techniques are listed in Table 3.3. The deposition rate do not follow any trend with the variation in rf-power, however the deposition rate is low as compared to Si thin films prepared using HWCVD technique. The band gap of these films was calculated by plotting $\sqrt{\alpha h\nu}$ vs $h\nu$ and is estimated to be in the range 1.7-1.8 eV. These results are summarized in Table 3.3.

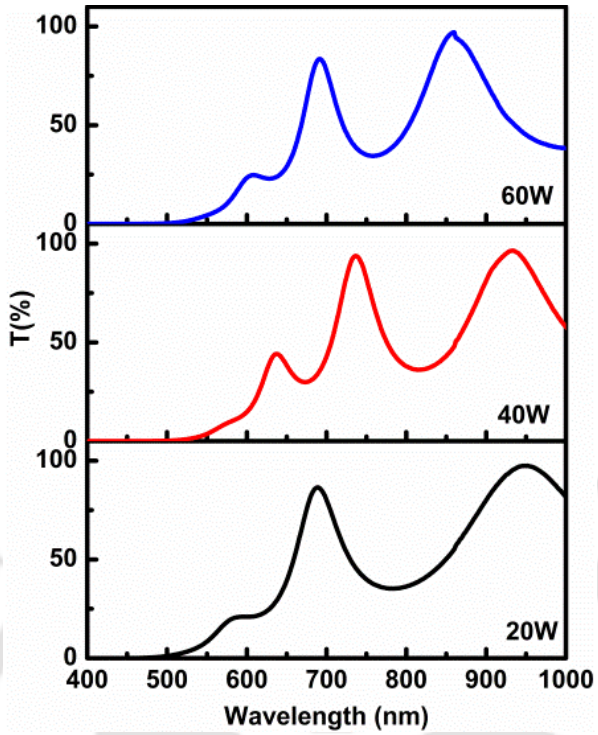

Figure 3.11: UV-Vis-NIR transmission spectra of the Si thin films prepared at different rf-power.

Table 3.3: Thickness, deposition rate (r_d) and optical band gap (E_g) for the films as estimated from UV-Vis-NIR transmission spectra along with the films thickness (t) measured using surface profilometer.

Sample No.	rf-power (W)	E_g (eV)	t (nm) (surface profilometer)	t (nm) (UV-Vis-NIR Transmission spectra)	r_d (Å/sec)
PE81	20	1.79	180	-	0.66
PE79	40	1.84	352	379	1.40
PE80	60	1.77	345	358	1.32

3.3.3 Electrical properties

Electrical characterization of the films was conducted in coplanar geometry using Ag paste as electrodes about 1 mm apart. Figure 3.12 shows the dark (σ_d) as well as photo (σ_{ph}) conductivity of the films measured at RT after annealing these films at 200 ºC. All the films are highly photosensitive (σ_{ph}/σ_d of an order of ~4 in magnitudes), however the films prepared at high rf power of 60 W show a slight decrease in photosensitivity.

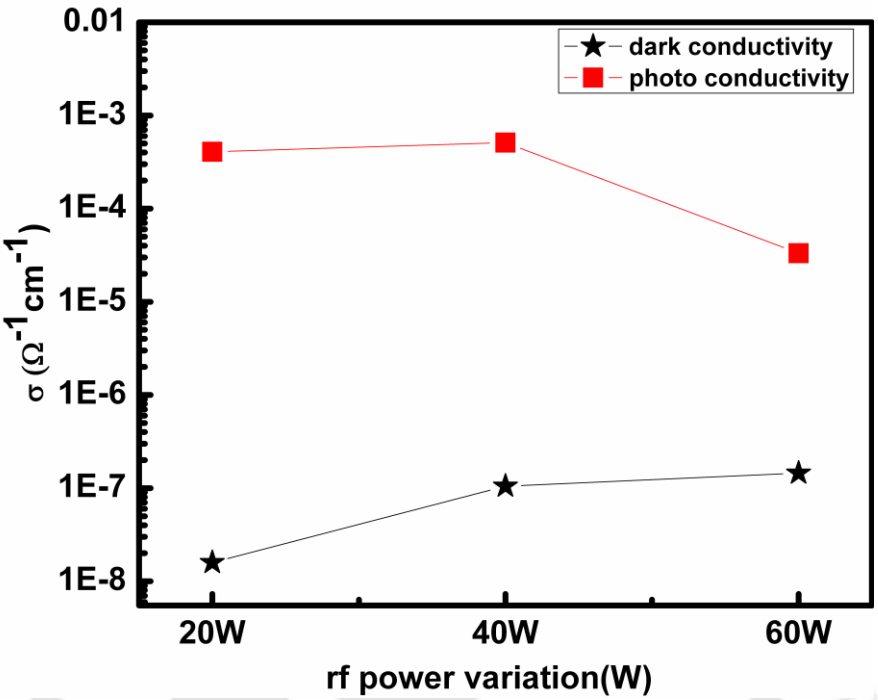

Figure 3.12: Dark and photo conductivity of Si thin films prepared at different rf-power.

These results show that even at high substrate temperature of 400º C and with H_2 dilution of 90%, the films were all amorphous in nature when rf power was low to moderate. Though all these films were amorphous in nature, a decrease in photosensitivity of the films with increasing rf power is an indication of improvement in structural ordering of the films.

3.4 The effect of variation of hydrogen dilution of SiH_4 on silicon thin films prepared using rf-PECVD technique (Series III)

As observed from our above studies that even a high substrate temperature (400℃) did not result in any structural change in silicon thin films. Therefore, in this section, silicon thin films were prepared with the variation of H_2 dilution of silane (50%-95%); as H_2 helps in breaking the weak Si-Si bonds and form a strong Si-Si, which may result in transition from amorphous to nanocrystalline silicon.

3.4.1 Structural Properties

3.4.1.1 X-ray Diffraction

Figure 3.13 shows the XRD pattern of all the films, prepared at different hydrogen dilution of silane, recorded using CuKα radiation (λ= 1.54 Å) in scanning range from 10º to 70º. All the films show broad peak at 28º which indicate that the films are amorphous in nature.

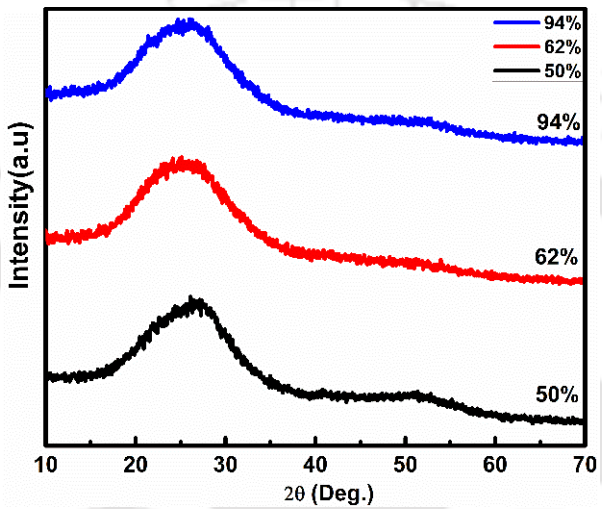

Figure 3.13: XRD pattern of silicon films prepared at different H_2 dilution.

3.4.1.2 Raman Spectroscopy

Figure 3.14 show the Raman spectra of the Si thin films prepared at different hydrogen dilution of silane. The Raman spectra were recorded using "Ar-ion laser" with excitation wavelength, 488 nm, in the scanning range of 300-600 cm^{-1} and at laser power density of 127 kW/cm^2. A broad peak centered at 480 cm^{-1} corresponding to the transverse optic mode (TO) of amorphous silicon is observed for the film prepared at low H_2 dilution (50%), however the films prepared at higher hydrogen dilution (>50%) show a small hump at ~515 cm^{-1} superimposed on broad peak centered at 480 cm^{-1}. This observed small hump at 515 cm^{-1} could also be due to laser induced crystallization while doing the Raman measurements as discussed in Chapter 4, since in XRD no peaks corresponding to c-Si appeared.

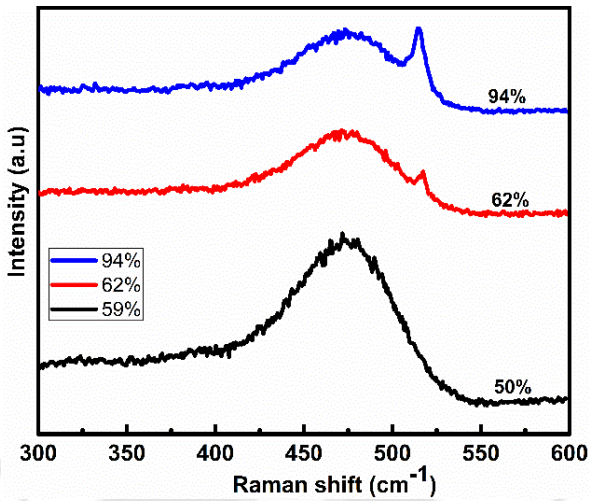

Figure 3.14: Raman spectra of silicon films prepared at different H_2 dilution.

3.4.2 Optical properties

The UV-Vis-NIR transmission spectra of these films are shown in Fig 3.15. The estimated thickness of these films from UV-Vis-NIR transmission spectra and surface profilometer are listed in Table 3.4. The band gap of these films was calculated by plotting $\sqrt{\alpha h\nu}$ vs $h\nu$ and is estimated to be in the range 1.7-1.8 eV. These results are summarized in Table 3.4.

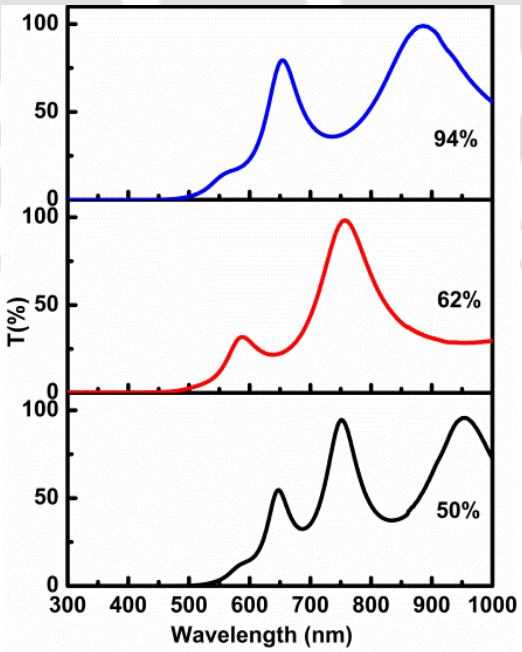

Figure 3.15: UV-Vis-NIR transmission spectra of the Si thin films prepared at different H_2 dilution.

Table 3.4: Thickness, deposition rate (r_d) and optical band gap (E_g) for the films as estimated from UV-Vis-NIR transmission spectra along with the films thickness (t) measured using surface profilometer.

Sample No.	H_2 dilution (%)	E_g (eV)	t (nm) surface profilometer	t (nm) UV-Vis-NIR Transmission spectra	r_d (Å/sec)
PE59	50	1.84	392	403	1.49
PE62	62	1.72	120	-	0.44
PE61	94	1.82	180	-	0.66

3.4.3 Electrical properties

Electrical characterization of these films was performed in coplanar geometry using Ag paste as electrodes. Figure 3.16 shows the dark (σ_d) as well as photo (σ_{ph}) conductivity of the films measured at RT after annealing these films at 200 ºC. All these films prepared at different hydrogen dilution are highly photosensitive (σ_{ph}/σ_d of an order of ~4 in magnitudes) even when the hydrogen dilution was as high as 94%.

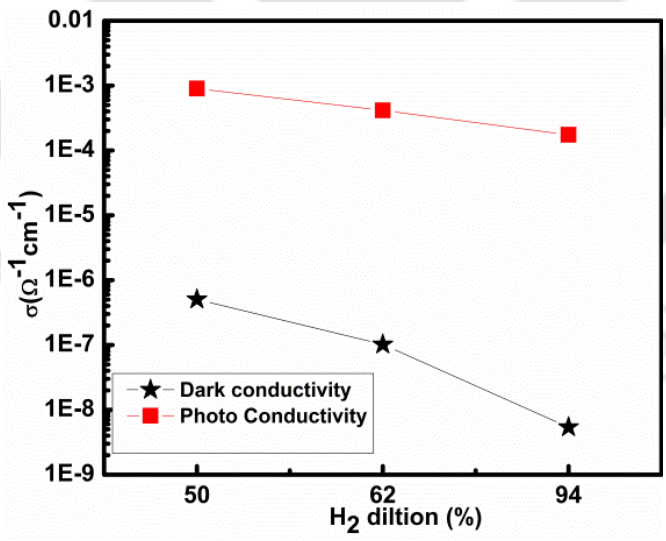

Figure 3.16: Dark and photo conductivity of Si thin films prepared at different Hydrogen dilution.

These results indicate that there was no change in structural and optoelectronic properties of Si thin films prepared at different H_2 dilution; this could be due to relatively low rf power of 50 W which has been used while depositing these films.

3.5 The effect of variation of substrate temperature on silicon thin films prepared using rf-PECVD technique (Series IV)

From the above studies, it has been observed that even high substrate temperature (400℃) as well as high H_2 dilution (94%) could not result in any microstructural change in silicon thin films, however as the rf-power was increased in series II, the photosensitivity was decreased resulting in slight change in structural properties of silicon thin films (Fig. 3.12). Therefore in this series IV, Si thin films were prepared with the variation of substrate temperature from 150℃ to 250℃ at high H_2 dilution of 96% while keeping the rf power high at 80 W.

3.5.1 Structural Properties

3.5.1.1 X-ray Diffraction

Figure 3.17, shows the XRD pattern of all the films prepared at different substrate (T_s) recorded using CuKα radiation (λ= 1.54 Å) in scanning range from 10º to 70º. Interestingly, all the films show small hump at 28º, 48º and 56º which corresponds to (111), (220) and (311) planes of crystalline silicon, respectively.

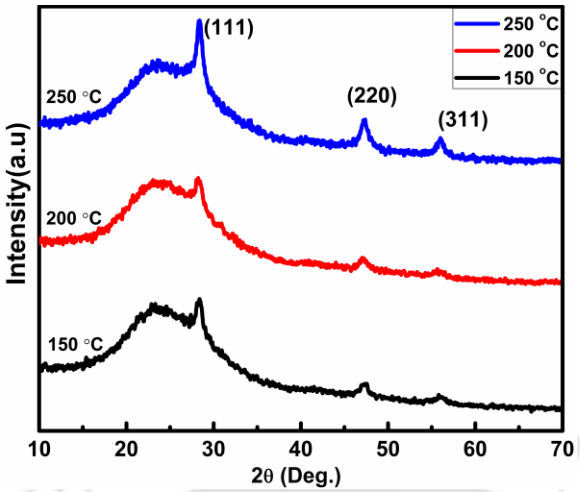

Figure 3.17: XRD pattern of silicon thin films prepared at different substrate temperature.

3.5.1.2 Raman Spectroscopy

Figure 3.18, shows the Raman scattering spectra for the films prepared at different substrate temperature. The Raman spectra were recorded using "Ar-ion laser" with excitation wavelength, 488 nm, in the scanning range of 300-600 cm^{-1} at laser power density of 127 kW/cm^2. A sharp peak near about 520 cm^{-1} corresponding to TO mode of phonon vibration of c-Si appears in all the films prepared at different substrate temperature this results further strengthen the XRD results. Further, in order to determine the nanocrystalline (X_{nc}) and total crystalline (X_c) volume fraction for these films, the Raman peaks were de-convoluted in three components: two Gaussian (480 cm^{-1} and 500 cm^{-1}) and one Lorentzian (511 cm^{-1}). The de-convoluted spectra of these films prepared at different substrate temperature are shown in Fig. 3.19 (a-c). Further for the estimation of X_{nc}(%) and X_c(%), the integrated intensity of all three peaks were considered and the percentage of X_{nc}(%) and X_c(%) were estimated using Eq. 2.2 & 2.3 as mentioned in Chapter 2. The values of X_{nc}(%) and X_c(%) are listed in Table 3.5. With the increase in substrate temperature the X_{nc}(%) and X_c(%) increases. The crystallite size of Si nanocrystals was also estimated using Eq. 2.1 (Chapter 2). For all the films of this series the crystallite size was found to be ~8 nm.

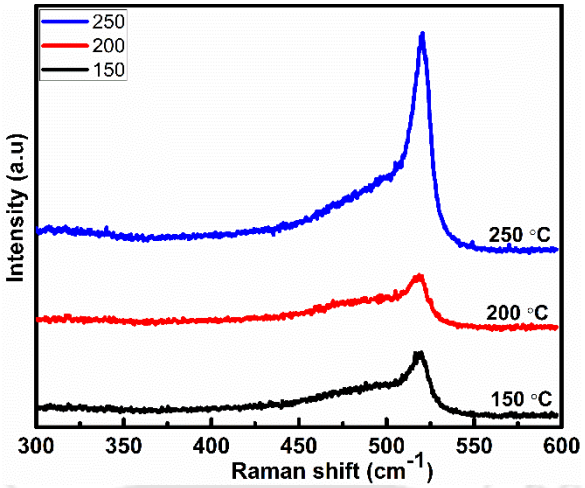

Figure 3.18: Raman spectra of the silicon thin films prepared at different substrate temperature.

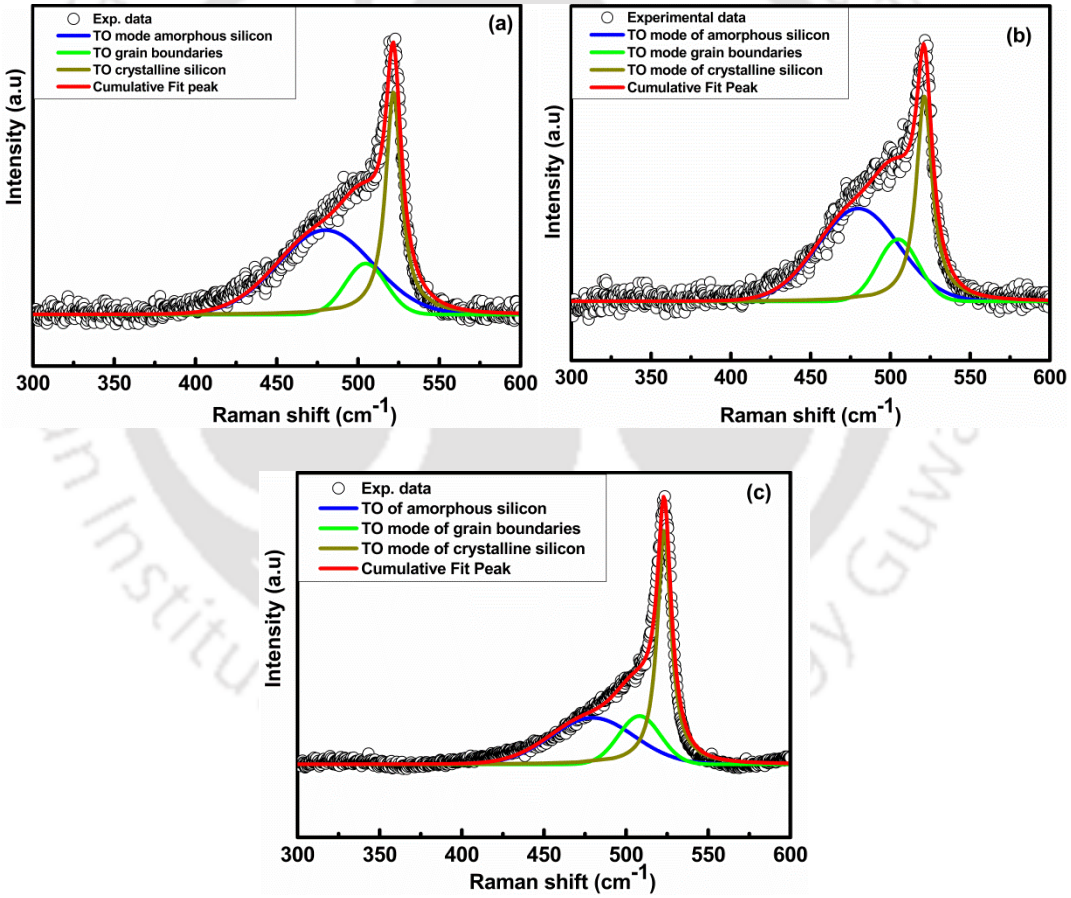

Figure 3.19: De-convoluted Raman spectra of silicon thin films prepared at substrate temperature (a) 150 ºC (b) 200 ºC (c) 250 ºC.

Table 3.5: Variation of X_{nc}(%) and X_c(%) with the variation in substrate temperature.

T_s (°C)	X_{nc} (%)	X_c (%)
150	34	48
200	33	49
250	45	64

3.5.1.3 Field Emission Electron Microscopy

Figure 3.20 (a-c) shows the FESEM images of silicon thin films (one samples of each series (II-IV)) prepared under different deposition conditions using rf-PECVD technique. The a-Si:H (Fig 3.20 (a,b)) films show the smooth surface with the small grains whereas, the nc-Si:H film (Fig 3.20 (c)) shows small nanocrystals with the presence of dispersed as well as packed grains.

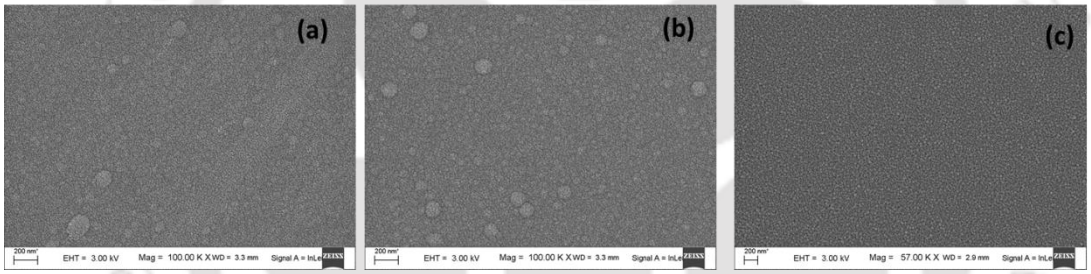

Figure 3.20: FESEM images of Si thin films at different deposition parameters a) 40W (Series II) b) 62% (Series III), c) 250°C (Series IV).

3.5.2 Optical properties

The UV-Vis-NIR transmission spectra of the films of this series are shown in Fig 3.21. The estimated thickness from surface profilometer for these films is listed in Table 3.6. The deposition rate for these films is low as compared to the films of previous Series II and Series III prepared using rf-PECVD technique. The low deposition is expected as the high H_2 dilution results in higher number of atomic H_2 which etch out the growing film surface and also the presence of more H_2 in the gas mixture dilutes the film forming radicals, which

may results in decrease in deposition rates of these films. Further the band gap of these films was calculated by plotting $\sqrt{\alpha h\nu}$ vs $h\nu$ and is estimated to be in the range 2.0-2.1 eV. The results are summarized in Table 3.6. The estimated band gap of these films is quite high, and this seems to be due to quantum confinement of the Si nanocrystals as the size of Si nanocrystals for these films was ~8 nm as estimated from Raman spectra .

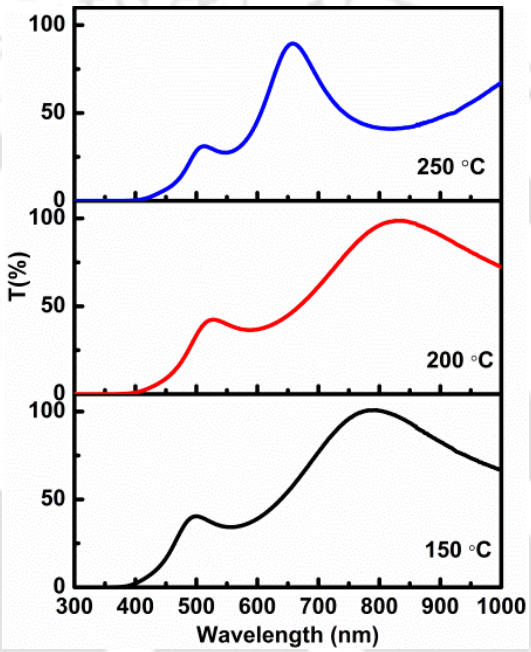

Figure 3.21: UV-Vis-NIR transmission spectra of the Si thin films prepared at different substrate temperature.

Table 3.6: Thickness, deposition rate (r_d) and optical band gap (E_g) for the films as estimated from UV-Vis-NIR transmission spectra along with the films thickness (t) measured using surface profilometer.

Sample No.	T_s (℃)	E_g (eV)	t (nm) (surface profilometer)	t (nm) (UV-Vis-NIR Transmission spectra)	r_d (Å/sec)
PE101	150	2.10	94	-	0.34
PE100	200	2.02	104	-	0.28
PE97	250	2.09	160	-	0.59

3.5.3 Electrical properties

Figure 3.22 shows, the dark (σ_d) and photoconductivity (σ_{ph}) of the films prepared at different substrate temperature in coplanar geometry after annealing at 200 ºC and measured at RT. The photosensitivity (σ_{ph}/σ_d) of all the films have reduced from 4 orders to ~1-2 orders of magnitude with the increase in dark conductivity.

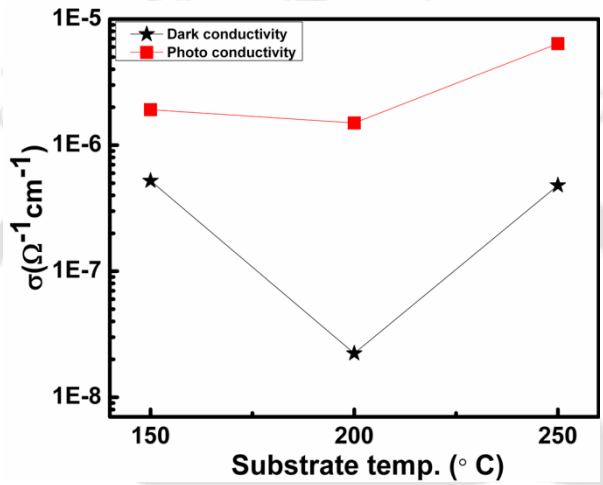

Figure 3.22: The Dark and Photo conductivity of silicon thin films prepared at different substrate temperature.

From the above results, it is evident that the deposition parameters play an important role in determining the microstructure and optoelectronic properties of Si thin films prepared using both HWCVD and rf-PECVD techniques. Therefore, it may be concluded that high H_2 dilution and high rf-power support the growth of nc-Si:H thin films even at low substrate temperature, whereas if hydrogen dilution is low and rf power is moderate, even at high substrate temperature, films are amorphous in nature. At high H_2 dilution, higher concentration of H atoms covers the growing surface and helps the diffusion of radicals having longer lifetime to seek energetically favorable sites, which results in the formation of dense network. Further H atoms also help in etching the weak Si bonds, leaving behind the stable configuration of high quality Si thin films. The ion flux impinging on the growing

film surface and ion energy are important parameter for the growth of nanocrystalline silicon. Therefore, when the rf power is high, it causes more ions and radicals impinge on growing film surface with higher energies resulting in formation of nanocrystalline silicon films even at low substrate temperature of 150℃.

3.6 Conclusion

Silicon thin films ranging from amorphous to nanocrystalline were prepared using both HWCVD and rf-PECVD techniques under different deposition parameters. Films prepared at low H_2 dilution by HWCVD technique were amorphous in nature whereas, nanocrystallinity developed with the increase in H_2 dilution. The deposition rate for the films prepared by HWCVD technique is found to be quite high (~ 10 Å/sec) as compared to films prepared rf-PECVD technique [32, 33]. Films prepared at low [R] are highly photosensitive (~4 orders of magnitude) whereas, photosensitivity decreases (less than 1 order in magnitude) with increase in [R]. The a-Si:H films are more photosensitive due to their low dark carrier concentration and higher absorption coefficient as compared to nc-Si films. The total crystalline volume fraction (as estimated from Raman spectra) increases from 0 to 64% with increase in [R]. This trend is similar to that reported in literature [34, 35]. Using rf-PECVD technique, highly crystalline Si films were obtained at high H_2 dilution $\geq$ 95% and at high rf-power, this observation is also consistent with the results reported in literature [36, 37]. These results suggest that the deposition parameters are important factors affecting the structural and optoelectronic properties of silicon thin films [38-41]. These highly crystalline films could be very useful for various device applications.

3.7 References

[1] S.J. Angus, A.J. Ferguson, A.S. Dzurak, R.G. Clark, Gate-Defined Quantum Dots in Intrinsic Silicon, Nano Letters, 7 (2007) 2051.

[2] A. Fujiwara, H. Inokawa, K. Yamazaki, H. Namatsu, Y. Takahashi, N.M. Zimmerman, S.B. Martin, Single electron tunneling transistor with tunable barriers using silicon nanowire metal-oxide-semiconductor field-effect transistor, Applied Physics Letters, 88 (2006) 053121.

[3] S. Tiwari, F. Rana, H. Hanafi, A. Hartstein, E.F. Crabbé, K. Chan, A silicon nanocrystals based memory, Applied Physics Letters, 68 (1996) 1377-1379.

[4] Y.T. Tan, T. Kamiya, Z.A.K. Durrani, H. Ahmed, Room temperature nanocrystalline silicon single-electron transistors, Journal of Applied Physics, 94 (2003) 633-637.

[5] S. Klein, F. Finger, R. Carius, M. Stutzmann, Deposition of microcrystalline silicon prepared by hot-wire chemical-vapor deposition: The influence of the deposition parameters on the material properties and solar cell performance, Journal of Applied Physics, 98 (2005) 024905.

[6] B. Rech, H. Wagner, Potential of amorphous silicon for solar cells, Applied Physics A, 69 (1999) 155-167.

[7] S. Guha, J. Yang, B. Yan, Amorphous and Nanocrystalline Silicon Solar Cells and Modules, Reference Module in Materials Science and Materials Engineering, Elsevier2016.

[8] J. Ma, J. Ni, J. Zhang, Z. Huang, G. Hou, X. Chen, X. Zhang, X. Geng, Y. Zhao, Improvement of solar cells performance by boron doped amorphous silicon carbide/nanocrystalline silicon hybrid window layers, Solar Energy Materials and Solar Cells, 114 (2013) 9-14.

[9] D.L. Staebler, C.R. Wronski, Reversible conductivity changes in discharge-produced amorphous Si, Applied Physics Letters, 31 (1977) 292-294.

[10] P. Roca i Cabarrocas, Plasma enhanced chemical vapor deposition of amorphous, polymorphous and microcrystalline silicon films, Journal of Non-Crystalline Solids, 266-269 (2000) 31-37.

[11] A. Matsuda, Growth mechanism of microcrystalline silicon obtained from reactive plasmas, Thin Solid Films, 337 (1999) 1-6.

[12] D. Stieler, V.L. Dalal, K. Muthukrishnan, M. Noack, E. Schares, Electron mobility in nanocrystalline silicon devices, Journal of Applied Physics, 100 (2006) 036106.

[13] A.V. Shah, J. Meier, E. Vallat-Sauvain, N. Wyrsch, U. Kroll, C. Droz, U. Graf, Material and solar cell research in microcrystalline silicon, Solar Energy Materials and Solar Cells, 78 (2003) 469-491.

[14] B. Sain, D. Das, Tunable photoluminescence from nc-Si/a-SiNx:H quantum dot thin films prepared by ICP-CVD, Physical Chemistry Chemical Physics, 15 (2013) 3881-3888.

[15] H.C. Dickey, T.T. Meek, Active electronic devices fabricated by DC plasma arc spray process, Vacuum, 59 (2000) 179-184.

[16] R. Goswami, S. Sampath, H. Herman, J.B. Parise, Shock synthesis of nanocrystalline Si by thermal spraying, Journal of Materials Research, 14 (2011) 3489-3492.

[17] S.Y. Tan, R.J. Gambino, S. Sampath, H. Herman, Electrical properties of pressure quenched silicon by thermal spraying, Thin Solid Films, 515 (2007) 7744-7750.

[18] S. Hitoshi, M. Keigo, M. Takuya, K. Takashi, K. Michio, N. Sachiko, T. Yoshiaki, K. Hirotaka, Y. Isao, High-efficiency microcrystalline silicon solar cells on honeycomb

textured substrates grown with high-rate VHF plasma-enhanced chemical vapor deposition, Japanese Journal of Applied Physics, 54 (2015) 08KB05.

[19] H. Takatsuka, M. Noda, Y. Yonekura, Y. Takeuchi, Y. Yamauchi, Development of high efficiency large area silicon thin film modules using VHF-PECVD, Solar Energy, 77 (2004) 951-960.

[20] K. Saito, M. Sano, S. Okabe, S. Sugiyama, K. Ogawa, Microcrystalline silicon solar cells fabricated by VHF plasma CVD method, Solar Energy Materials and Solar Cells, 86 (2005) 565-575.

[21] S. Samanta, D. Das, Nanocrystalline silicon thin films from SiH4 plasma diluted by H2 and He in RF-PECVD, Journal of Physics and Chemistry of Solids, 105 (2017) 90-98.

[22] A. Matsuda, Formation kinetics and control of microcrystallite in μc-Si:H from glow discharge plasma, Journal of Non-Crystalline Solids, 59-60 (1983) 767-774.

[23] S. Guha, J. Yang, B. Yan, High efficiency multi-junction thin film silicon cells incorporating nanocrystalline silicon, Solar Energy Materials and Solar Cells, 119 (2013) 1-11.

[24] R. Nozawa, H. Takeda, M. Ito, M. Hori, T. Goto, In situ observation of hydrogenated amorphous silicon surfaces in electron cyclotron resonance hydrogen plasma annealing, Journal of Applied Physics, 85 (1999) 1172-1177.

[25] R. Nozawa, H. Takeda, M. Ito, M. Hori, T. Goto, Substrate bias effects on low temperature polycrystalline silicon formation using electron cyclotron resonance SiH4/H2 plasma, Journal of Applied Physics, 81 (1997) 8035-8039.

[26] M. Agarwal, A. Pawar, N. Wadibhasme, R. Dusane, Controlling the c-Si/a-Si:H interface in silicon heterojunction solar cells fabricated by HWCVD, Solar Energy, 144 (2017) 417-423.

[27] M. Heintze, R. Zedlitz, H.N. Wanka, M.B. Schubert, Amorphous and microcrystalline silicon by hot wire chemical vapor deposition, Journal of Applied Physics, 79 (1996) 2699-2706.

[28] P. Gogoi, H.S. Jha, P. Agarwal, Effect of Silane flow rate on microstructure of Silicon films deposited by HWCVD, Journal of Non-Crystalline Solids, 358 (2012) 1990-1994.

[29] B.P. Swain, N.M. Hwang, Effect of negative substrate bias on HWCVD deposited nanocrystalline silicon (nc-Si) films, Solid State Sciences, 11 (2009) 467-471.

[30] S. Veprek, F.A. Sarott, Z. Iqbal, Effect of grain boundaries on the Raman spectra, optical absorption, and elastic light scattering in nanometer-sized crystalline silicon, Physical Review B, 36 (1987) 3344-3350.

[31] R. Swanepoel, Determination of the thickness and optical constants of amorphous silicon, Journal of Physics E: Scientific Instruments, 16 (1983) 1214.

[32] S.R. Jadkar, J.V. Sali, A.M. Funde, N. Ali Bakr, P.B. Vidyasagar, R.R. Hawaldar, D.P. Amalnerkar, Deposition of hydrogenated amorphous silicon (a-Si:H) films by hot-wire chemical vapor deposition (HW-CVD) method: Role of substrate temperature, Solar Energy Materials and Solar Cells, 91 (2007) 714-720.

[33] M. Hideki, Catalytic Chemical Vapor Deposition (CTC–CVD) Method Producing High Quality Hydrogenated Amorphous Silicon, Japanese Journal of Applied Physics, 25 (1986) L949.

[34] D. Das, K. Bhattacharya, Characterization of the Si:H network during transformation from amorphous to micro- and nanocrystalline structures, Journal of Applied Physics, 100 (2006) 103701.

[35] B.-R. Wu, T.-H. Tsai, D.-S. Wuu, Hot-wire chemical vapor deposition of nanocrystalline silicon for ambipolar thin-film transistor applications, Applied Surface Science, 354 (2015) 216-220.

[36] A. Matsuda, Formation kinetics and control of microcrystallite in μc-Si:H from glow discharge plasma, Journal of Non-Crystalline Solids, 59-60 (1983) 767-774.

[37] A. Parashar, S. Kumar, J. Gope, C.M.S. Rauthan, S.A. Hashmi, P.N. Dixit, RF power density dependent phase formation in hydrogenated silicon films, Journal of Non-Crystalline Solids, 356 (2010) 1774-1778.

[38] A. Chowdhury, S. Mukhopadhyay, S. Ray, Effect of electrode separation on PECVD deposited nanocrystalline silicon thin film and solar cell properties, Solar Energy Materials and Solar Cells, 94 (2010) 1522-1527.

[39] W. Li, D. Xia, H. Wang, X. Zhao, Hydrogenated nanocrystalline silicon thin film prepared by RF-PECVD at high pressure, Journal of Non-Crystalline Solids, 356 (2010) 2552-2556.

[40] T.F.G. Muller, D. Knoesen, C. Arendse, R. Swanepoel, S. Halindintwali, C. Theron, Crystallization of HWCVD amorphous silicon thin films at elevated temperatures, Thin Solid Films, 501 (2006) 98-101.

[41] P. Gogoi, H.S. Jha, P. Agarwal, Variation of microstructure and transport properties with filament temperature of HWCVD prepared silicon thin films, Thin Solid Films, 519 (2011) 4506-4510.

Chapter 4

Laser Induced Selective Crystallization of Amorphous Silicon Thin Film for Device Applications

Crystallization kinetics in the hydrogenated amorphous silicon (a-Si:H) films has been a subject of considerable interest. As the device sizes are reduced and integrated circuits become more sophisticated, the ability of selectively affecting the individual elements of integrated circuits is gaining more and more practical values. In this context, laser irradiation is capable of selectively interacting with solids and is therefore a convenient method to alter the structure as compared to other methods such as HWCVD, rf-plasma enhanced chemical vapor deposition (rf-PECVD), radio frequency hollow electrode enhanced glow plasma (rf-HEEPT), electron cyclotron resonance and thermal annealing etc [1-13]. Laser annealing provides a means for fabrication of nanocrystalline (nc-Si) and microcrystalline silicon thin films [14-18] which are widely used in thin film transistors, solar cells and other optoelectronic devices [19-26]. Raman spectroscopy is one of the most sensitive and non-destructive techniques which make it possible to monitor the process of restructuring of silicon bonds in thin films upon laser treatment. In this chapter, detail studies on the continuous wave laser induced crystallization of hydrogenated amorphous silicon (a-Si:H) thin films using Raman Spectroscopy has been presented.

4.1 Measurement Details

Amorphous silicon thin films prepared with the variation of rf power (Series II) and hydrogen dilution (Series III) of silane using rf-PECVD technique have been used for these studies. The deposition parameters for these films are mentioned in detail in Table 2.2 & 2.3 of Chapter 2. To study the high intensity laser beam induced microstructural change in amorphous silicon thin films, the Raman measurements were performed. The films were irradiated with various laser power densities ranging from 127-445 kW/cm^2 for 2 mins each time on the spot size of ~1μm diameter of the sample surface using laser source of 488 nm. Whereas, in case of 632.8 nm laser source, the laser power density was varied in step from 68-687 kW/cm^2 on the spot size of ~1μm diameter of the sample surface for 2 mins each time. Raman spectra were recorded in the scanning range of 300-600 cm^{-1}, in as deposited state and after irradiating the films with high power laser beam. All the Raman spectra were recorded at low laser power density of 127 kW/cm^2 for 488 nm laser source whereas, in case of 632.8 nm laser source the spectra were recorded at 171 kW/cm^2. All Raman spectra were deconvoluted into peaks corresponding to a-Si, nc-Si and Si at grain boundaries to estimate total crystalline (X_c) and nanocrystalline (X_{nc}) volume fractions as discussed in Chapter 2.

4.2 Results and Discussion

Figures 4.1(a)-4.3(a) show the Raman spectra (at an excitation wavelength of 488 nm) of the as-deposited a-Si:H thin films of Series III (prepared at different H_2 dilution) and after the exposures with various laser power density. In the as deposited state (inset of Fig 4.1(a)-4.3(a)), the a-Si:H film prepared at low H_2 dilution of 50% exhibits a broad peak centered at 480 cm^{-1} which corresponds to the transverse optic mode (TO) of amorphous silicon with no nanocrystalline Si features. However, the a-Si:H films prepared at higher H_2 dilution of 62%

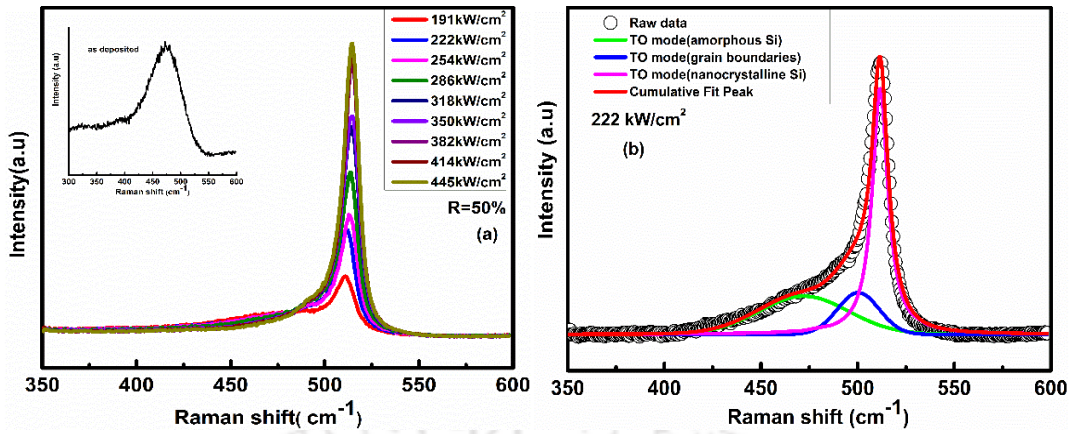

Figure 4.1: (a) Raman spectra at different Laser power density ([R]=50%), (b) Deconvoluted Raman spectra of the film after irradiation with laser power density 222 kW/cm^2.

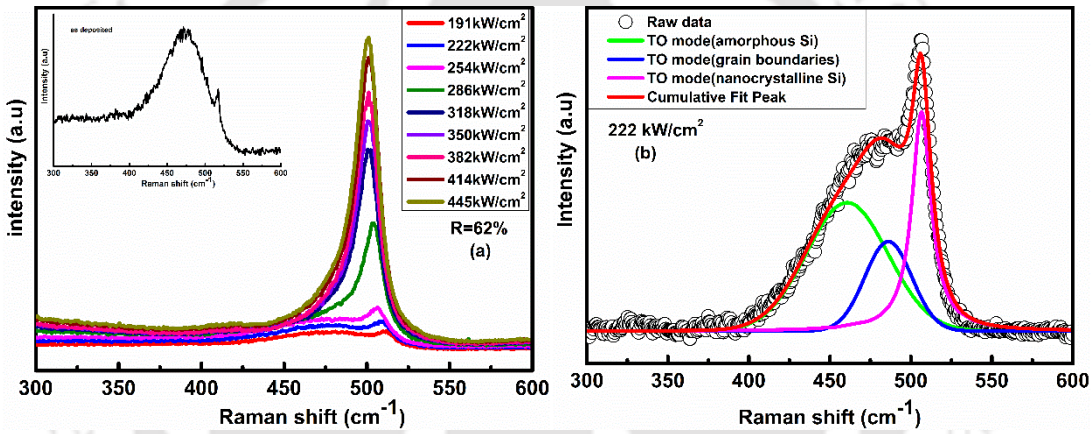

Figure 4.2: (a) Raman spectra at different Laser power density for the film prepared at ([R]=62%), (b) De-convoluted Raman spectra of the film after irradiation with laser power density 222 kW/cm^2.

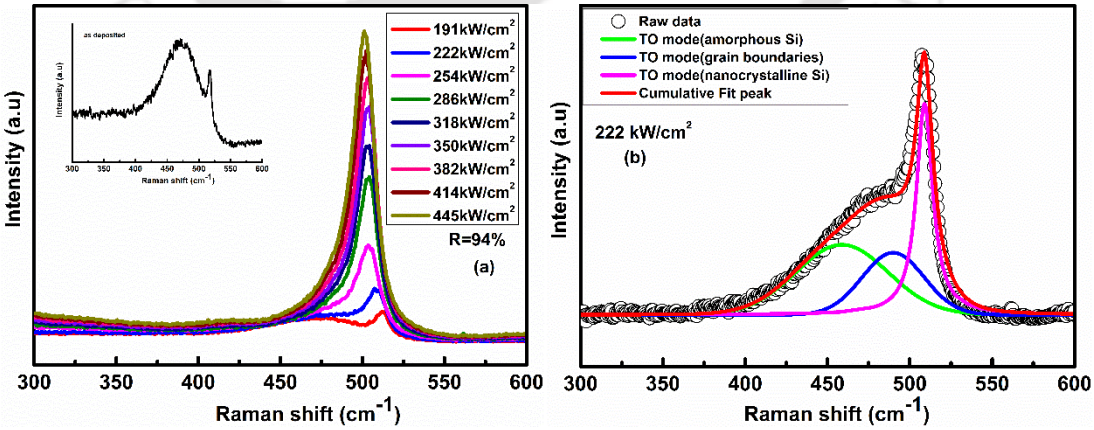

Figure 4.3: (a) Raman spectra at different Laser power density for the film prepared at [R]=94%, (b) De-convoluted Raman spectra of the film after irradiation with laser power density 222 kW/cm^2.

and 94% show a small hump at ~515 cm^{-1} superimposed on the broad peak centered at 480 cm^{-1}. After exposure to high intensity laser beam, the Raman peak shift gradually from 480 cm^{-1} to 515 cm^{-1} in all the films prepared at different H_2 dilution. The height of peak depends upon the intensity of the laser beam used during the exposure; peak intensity increases with increasing laser power density. In order to determine the total nanocrystalline (X_{nc}) and crystalline (X_c) volume fraction for the area of films which was exposed to high intensity laser beam, the Raman peaks were de-convoluted in three components: two Gaussian (480 cm^{-1} and 495 cm^{-1} corresponding to TO mode of a-Si:H and grain boundaries respectively) and one Lorentzian (511 cm^{-1} corresponding to nc-Si) [27, 28]. One such de-convoluted spectra (at laser power density of 222 kW/cm^2) for each of these films prepared at different H_2 dilution are shown in Fig. 4.1(b)-4.3(b). The integrated intensity for all the three peaks was considered and using Eq. 2.2 & 2.3 (as mentioned in chapter 2) the values of X_{nc}(%) and X_c(%) were estimated. Figure 4.4 (a-b) shows the X_c(%) and X_{nc}(%) values as a function of laser power density for all these films. With the increase in laser power density, X_{nc}(%) and X_c(%) increase almost linearly upto ~350 kW/cm^2 and after that it tend to saturate in all the films irrespective of the deposition parameters.

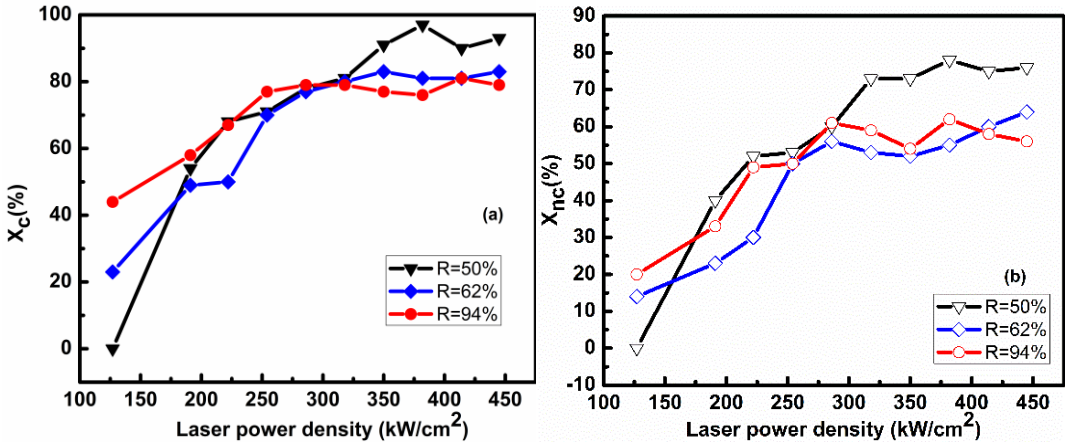

Figure 4.4: Variation of a) X_c(%) and b) X_{nc}(%) as a function of laser power density (488 nm laser source) for the films prepared at different [R].

Further in order to check whether the extent of crystallinity depends on the deposition parameters used during the growth of a-Si:H thin films, similar studies (using the same laser source of 488 nm) were conducted for a-Si:H films of Series II, prepared with the variation of rf power. Figure 4.5(a)-4.7(a) show the Raman spectra (at excitation wavelength 488 nm) of all the as-deposited a-Si:H thin film (prepared at different rf power) and after the exposure with various laser power density. All the films in the as-deposited state exhibit a broad peak centered at 480 cm^{-1} which corresponds to the TO mode of amorphous silicon with no nc-Si features, as shown in the inset of Fig 4.5(a)-4.7(a). Similar to our earlier observation, after exposure to high intensity laser beam, the Raman peak shifts from 480 cm^{-1} to 510 cm^{-1} in each spectra and the peak intensity increases with increase in laser power. Once again for the estimation of X_{nc}(%) and X_c(%), the Raman spectra were de-convoluted into three peaks two Gaussian and one Lorentzian. One such de-convoluted spectra (at laser power density of 222 kW/cm^2) for each of these films prepared at different rf power are shown in Fig. 4.5(b)-4.7(b). From Fig. 4.8(a, b), it was observed that at laser power density of 191 kW/cm^2, the film prepared at high rf power of 60W shows a significant change in X_c(%) and X_{nc}(%) as compared to films prepared at low rf power of 20W and 40W.

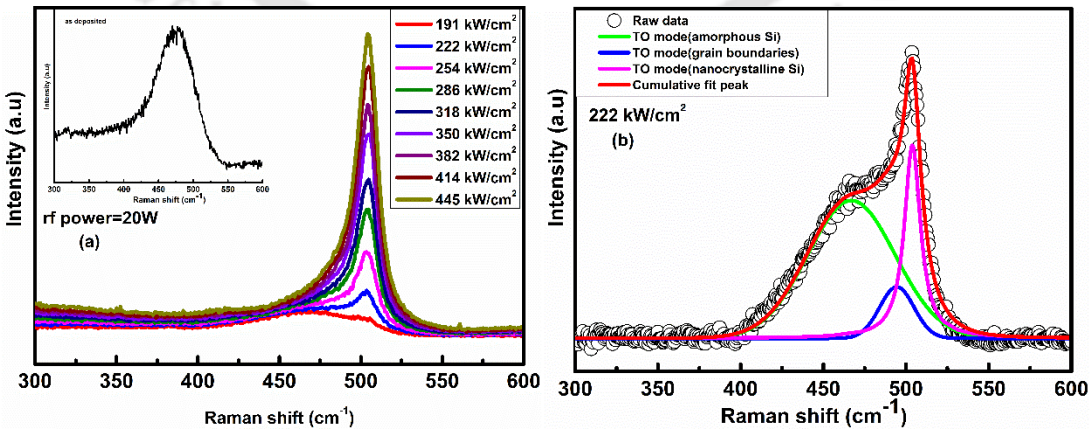

Figure 4.5: (a) Raman spectra at different laser power density (rf power=20W), (b) De-convoluted Raman spectra of the film after irradiation with laser power density 222 kW/cm^2.

However, with the further increase in laser power, X_{nc}(%) and X_c(%) increase linearly upto ~350 kW/cm^2 and after that it saturate as observed earlier. It may also be noted that the changes in X_c(%) and X_{nc}(%) are quite similar for both series of a-Si:H films; prepared with the variation of H_2 dilution of silane (Series III) as well as rf power (Series II).

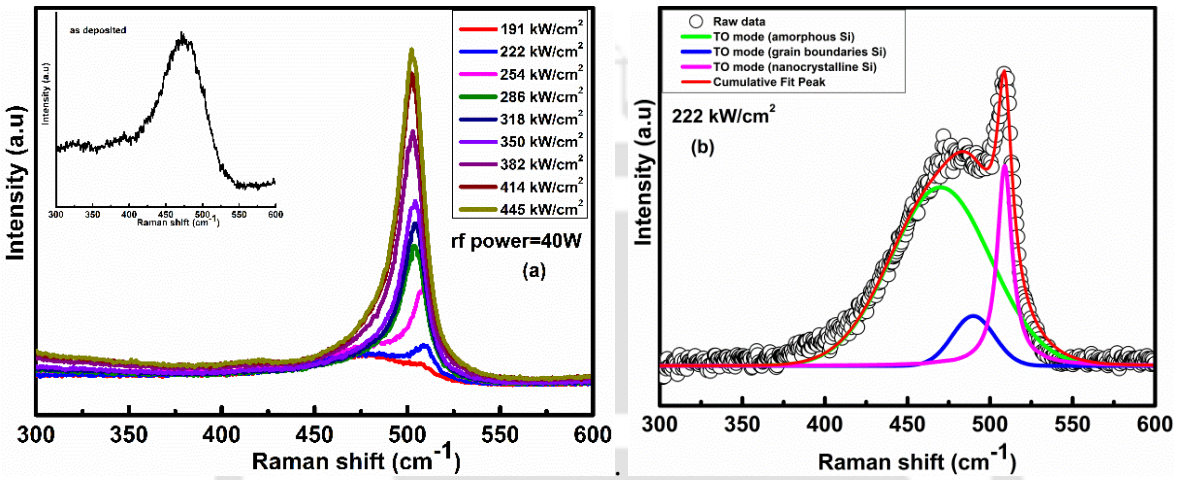

Figure 4.6: (a) Raman spectra at different laser power density (rf power=40W), (b) De-convoluted Raman spectra of the film after irradiation with laser power density 222 kW/cm^2.

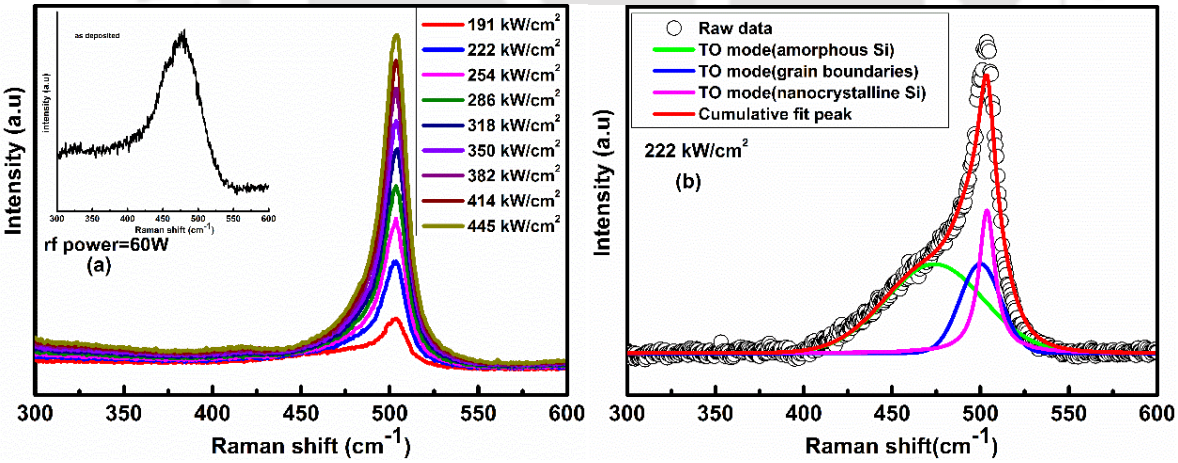

Figure 4.7: (a) Raman spectra at different laser power density (rf power=60W), (b) De-convoluted Raman spectra of the film after irradiation with laser power density 222 kW/cm^2.

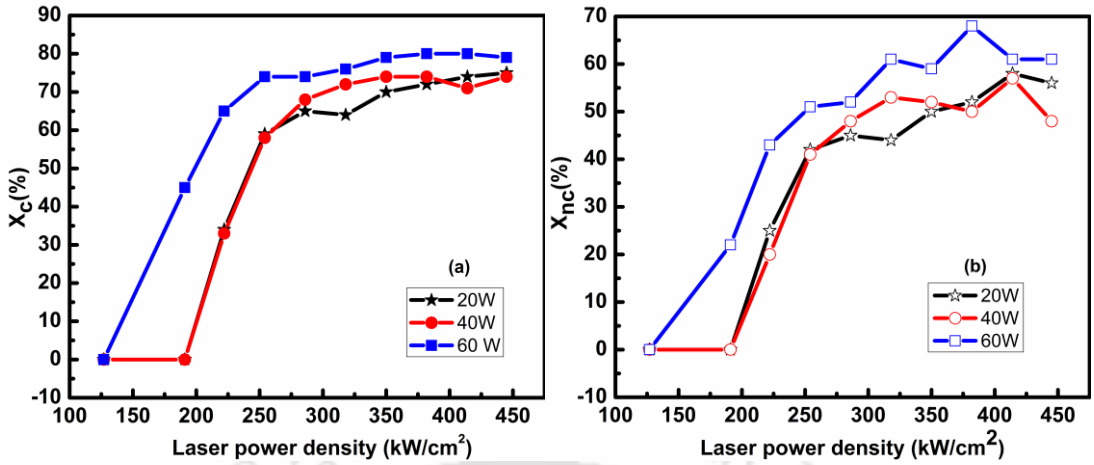

Figure 4.8: Variation of a) X_c(%) and b) X_{nc}(%) as a function of laser power density (488 nm laser source) for the film prepared at different rf-power.

Further, it is important to check whether the laser source of different wavelength exhibits similar effect. Therefore, once again Raman spectra were recorded using a different laser source of wavelength 632.8 nm after exposing the films with the laser power density ranging from 68-687 kW/cm^2. This measurements were conducted on the a-Si:H films of Series III (prepared with the variation of H_2 dilution of silane). Figure 4.9 (a-c) shows the Raman spectra recorded at an excitation wavelength 632.8 nm and after exposure to high laser power density. It was observed that at low power density, all films were amorphous in nature. However, when laser power density increases above 200 kW/cm^2, a shift in Raman peak from 480 cm^{-1} to 510 cm^{-1} was observed for all the films, indicating the partial crystallization similar to our earlier observation. For the estimation of X_{nc}(%) and X_c(%) the Raman peaks were deconvoluted into peak corresponding to amorphous silicon, grain boundaries and nanocrystalline silicon (Fig 4.10 (a,b)-4.12(a,b)). Figure 4.13(a, b) shows the variation X_{nc}(%) and X_c(%) as a function of laser power density for these films. With the increase in laser power density beyond 200 kW/cm^2 the nanocrystalline and total crystalline

volume fraction increases in all the films. For a given power density, the crystalline fraction for films deposited using different H_2 dilution are quite similar.

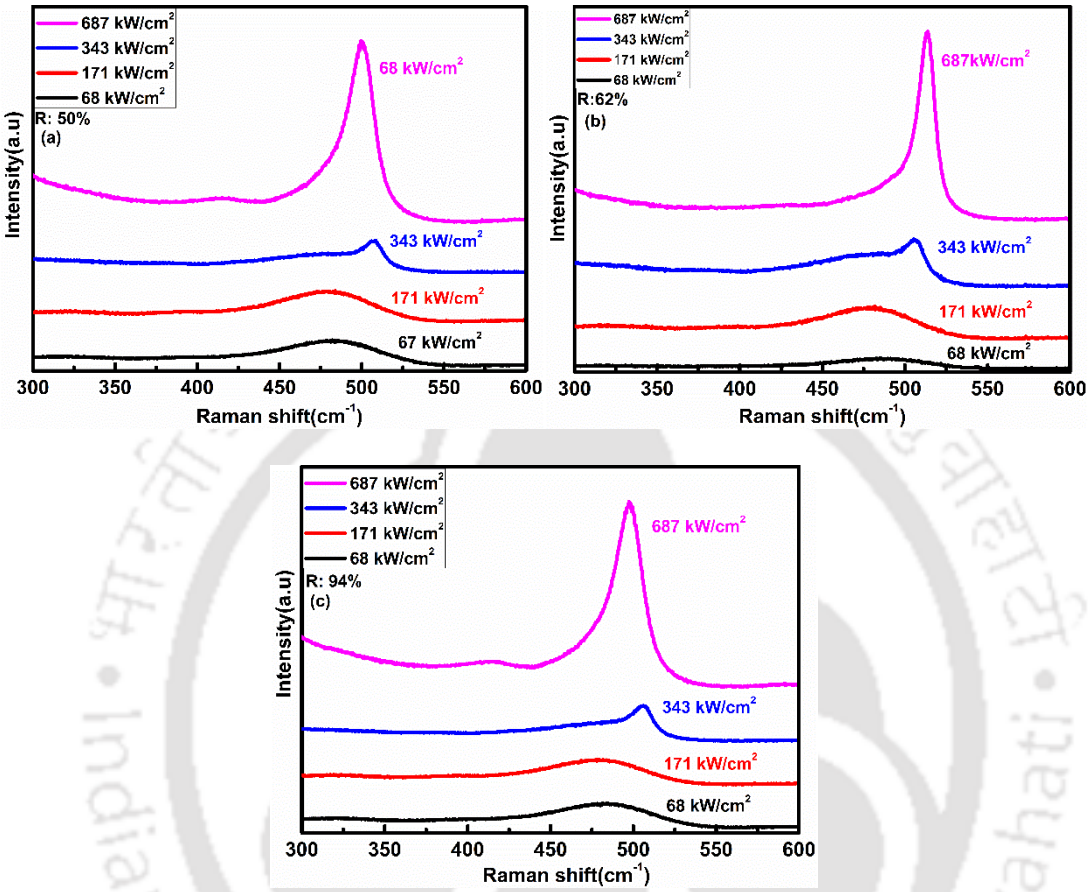

Figure 4.9: Raman spectra at different H_2 dilution a) 50 %, b) 62 %, c) 94 % and at different laser power density.

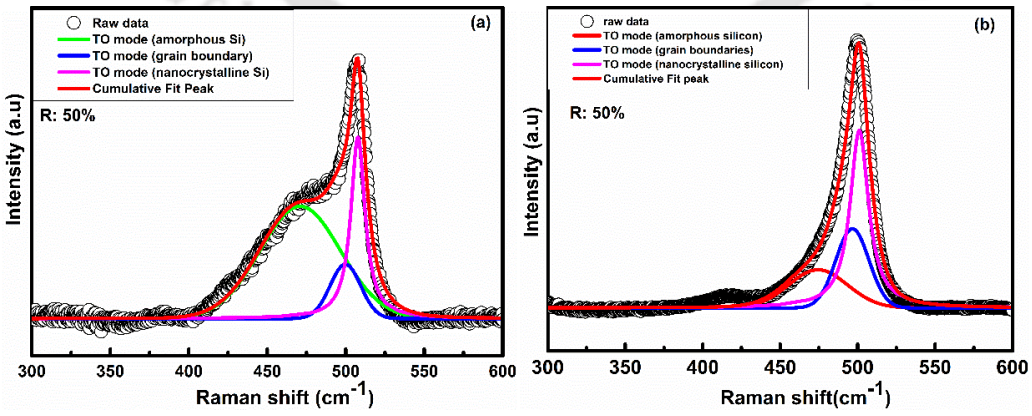

Figure 4.10: De-convoluted Raman spectra of the film (at [R]=50%) after irradiation with laser power density a) 343 kW/cm^2 and b) 687 kW/cm^2.

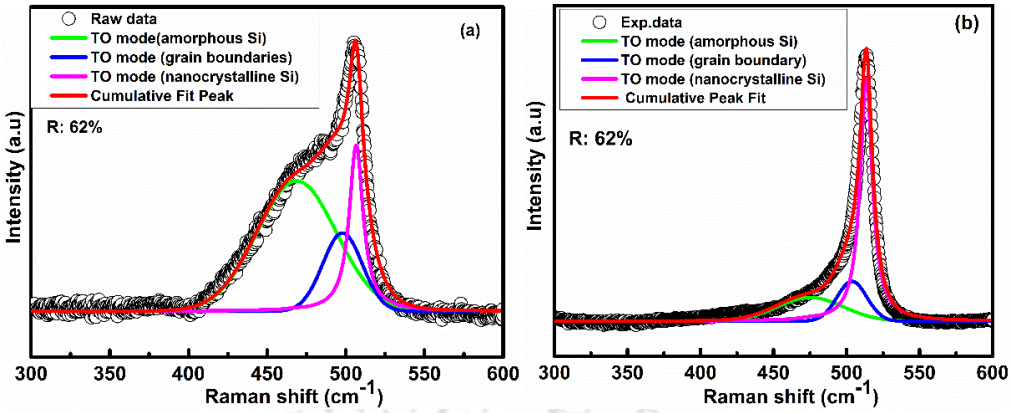

Figure 4.11: De-convoluted Raman spectra of the film (at [R]=62%) after irradiation with laser power density a) 343 kW/cm^2 and b) 687 kW/cm^2.

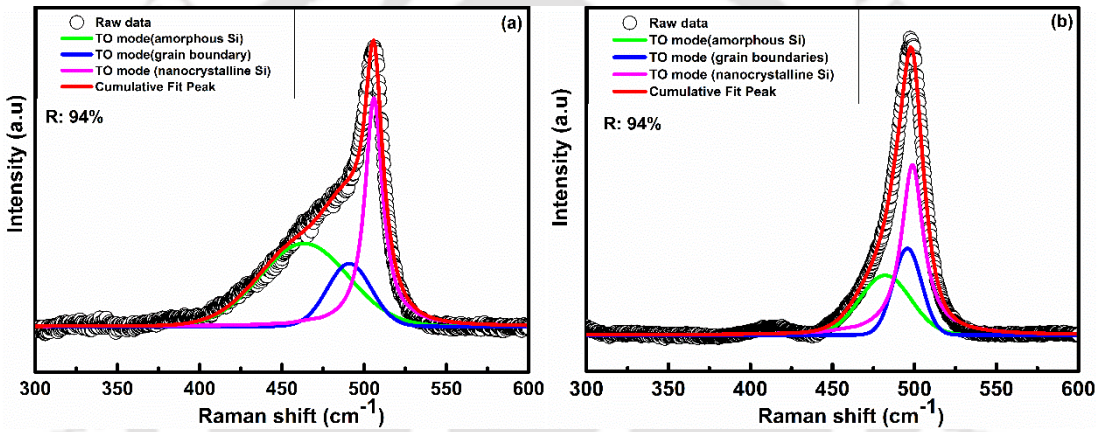

Figure 4.12: De-convoluted Raman spectra of the film (at [R]=94%) after irradiation with laser power density a) 343 kW/cm^2 and b) 687 kW/cm^2.

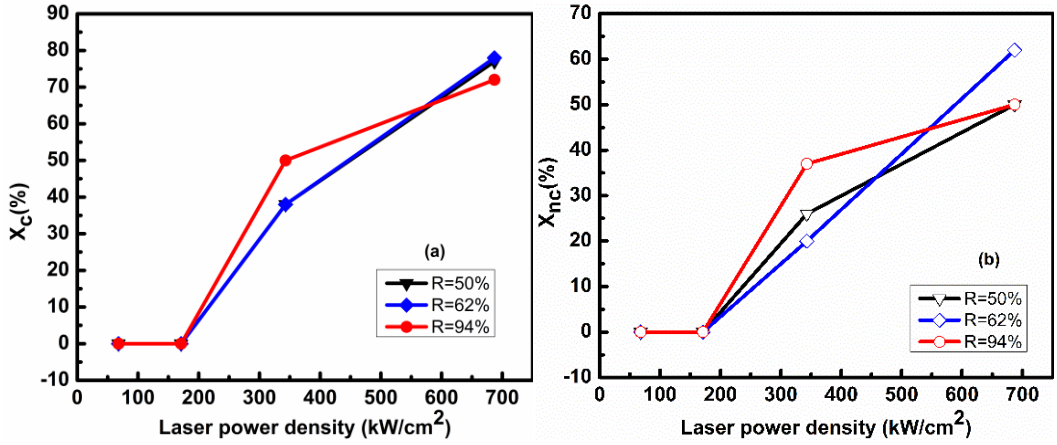

Figure 4.13: Variation of a) X_c(%)and b) X_{nc}(%) as a function of laser power density (632.8 nm laser source) for the films prepared at [R].

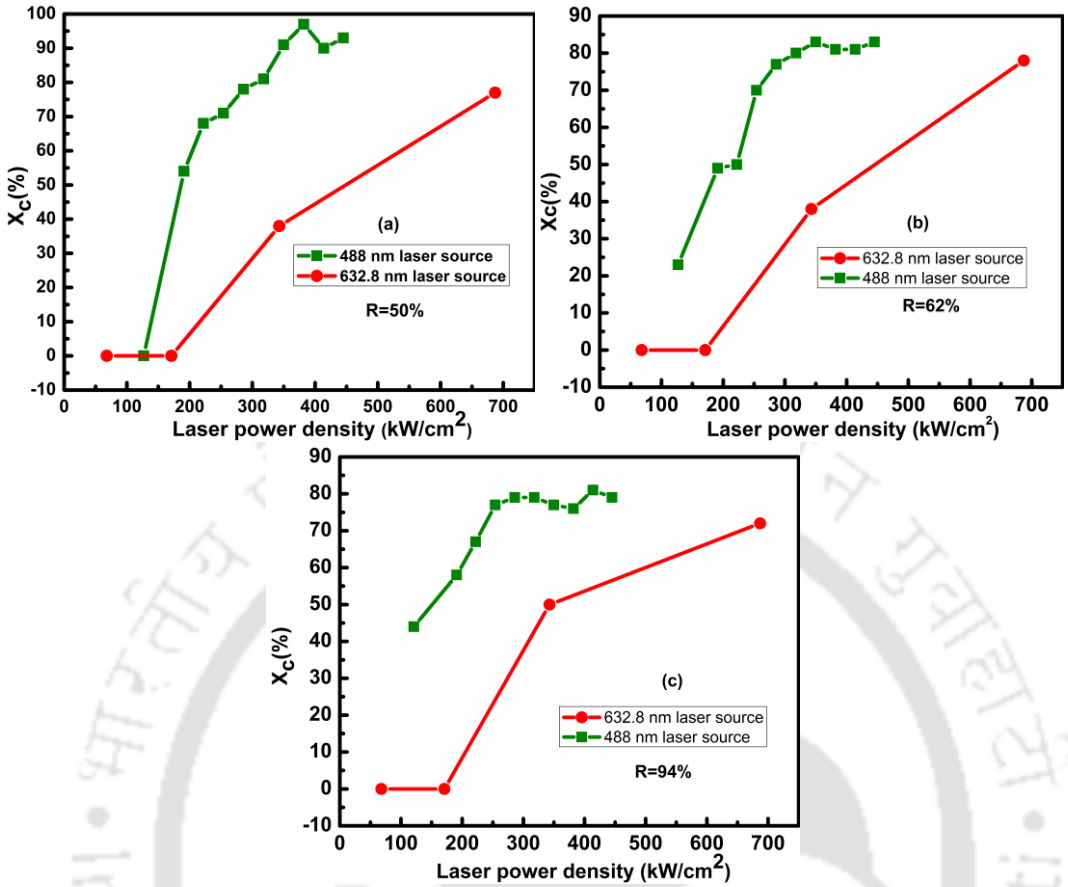

Figure 4.14: Variation of X_c (%) as a function of laser power density using two different lasersource (488 nm and 632.8 nm) for the film prepared at different [R]; a) 50%, b) 62% and c) 94%.

The above results indicate that the exposure to high intensity laser beam induces structural change in amorphous Si thin films and there is a change in the oscillator strength of Si-Si bonds, which is reflected as a change in position of Raman peak from 480 cm^{-1} to 515 cm^{-1} in all the films irrespective of deposition parameters as well as laser source of different wavelength. These results can be understood in terms of laser induced local heating of the films due to non-radiative recombination of photo generated e-h pair which increases the temperature of the films. The crystallization takes place due to local rapid thermal annealing of the films. Figure 4.14 (a-c) shows the total X_c vs laser power density for two different laser source for films prepared by variation of hydrogen dilution (Series III). It can be seen

that the extent of crystallization depends upon the energy of the photons from laser. Further, the films remain amorphous even for 200 kW/cm^2 of power density from 632.8 nm laser, whereas these were partially crystallized even at 127 kW/cm^2 power density from 488nm laser, though in later case (127 kW/cm^2, 488 nm) , the photon flux is much less as compared to former case (200 kW/cm^2 , 632.8 nm). Further it can be seen that the laser power density is nearly doubled in case of 632.8 nm laser source to achieve same crystalline volume fraction as compared to 488 nm laser source. In case of 632.8 nm laser, absorption coefficient ($\alpha=2.5\times10^4$ cm^{-1}) is low and light is absorbed slowly and deeper in the bulk rather than near the surface. In case of exposure to 488 nm photons, the absorption coefficient is high ($\alpha=1.8\times10^5$ cm^{-1}) and a large fraction of incident photons are absorbed within 10-20 nm depth from the surface. The heat generated, in case of 488nm light, is thus concentrated in a smaller volume of the film resulting in a large change in temperature, which induces the crystallinity. When the incident power density is increased beyond 200 kW/cm^2, even for 632.8 nm light source, the number of photon absorbed near the surface is sufficiently large to increase the local temperature and process of crystallization starts. Thus, above studies indicate that laser induced crystallization allow us to achieve a microstructural change in Si thin films at a selective area leaving behind the other region unchanged. These highly crystalline silicon films find important new application in various optoelectronic devices. These results also suggest that very low laser power density should be used for Raman measurements else it may induce a microstructural changes at local level and hence gives wrong results.

4.3 Conclusion

Phase transition from amorphous to nanocrystalline silicon was employed by laser radiation with the variation in laser power density using Raman spectroscopy. With the increase of laser power density, the crystallinity is induced in all amorphous silicon thin films irrespective of deposition parameter. The extent of crystallization depends upon the energy of the photon from laser, low energy beam requires high power density to achieve the same crystalline volume fraction as compared to high energy laser beam. Upon exposure to the high intensity laser beam, the incident radiation is absorbed in the film and the incident photon energy is transformed into heat. This results in an increase in temperature of the thin film which in turn induces the crystallinity in a-Si:H thin film. The area of the films which was not exposed to high intensity laser beam remains unchanged. This technique seems to be quite convenient method [29-31] as compared to other techniques to induce micro-structural changes in Si thin films at selective area for various device applications.

4.4 References

[1] P. Gogoi, P. Agarwal, Structural and optical studies on hot wire chemical vapour deposited hydrogenated silicon films at low substrate temperature, Solar Energy Materials and Solar Cells, 93 (2009) 199-205.

[2] S. Michard, M. Meier, B. Grootoonk, O. Astakhov, A. Gordijn, F. Finger, High deposition rate processes for the fabrication of microcrystalline silicon thin films, Materials Science and Engineering: B, 178 (2013) 691-694.

[3] C.-H. Lee, W.S. Wong, A. Sazonov, A. Nathan, Study of deposition temperature on high crystallinity nanocrystalline silicon thin films with in-situ hydrogen plasma-passivated grains, Thin Solid Films, 597 (2015) 151-157.

[4] R.C. Mani, I. Pavel, E.S. Aydil, Deposition of nanocrystalline silicon films at room temperature, Journal of Applied Physics, 102 (2007) 043305.

[5] T. Tabuchi, Y. Toyoshima, M. Takashiri, Effect of reducing impurity concentration of microcrystalline silicon thin films for solar cells using radio frequency hollow electrode enhanced glow plasma, Vacuum, 101 (2014) 125-129.

[6] B.-R. Wu, T.-H. Tsai, D.-S. Wuu, Hot-wire chemical vapor deposition of nanocrystalline silicon for ambipolar thin-film transistor applications, Applied Surface Science, 354 (2015) 216-220.

[7] B. Stannowski, J.K. Rath, R.E.I. Schropp, Thin-film transistors deposited by hot-wire chemical vapor deposition, Thin Solid Films, 430 (2003) 220-225.

[8] L.H. Teng, W.A. Anderson, Thin film transistors on nanocrystalline silicon directly deposited by a microwave plasma CVD, Solid-State Electronics, 48 (2004) 309-314.

[9] G.K. Giust, T.W. Sigmon, Laser-processed thin-film transistors fabricated from sputtered amorphous-silicon films, IEEE Transactions on Electron Devices, 47 (2000) 207-213.

[10] L. Khriachtchev, S. Novikov, J. Lahtinen, Thermal annealing of Si/SiO2 materials: Modification of structural and photoluminescence emission properties, Journal of Applied Physics, 92 (2002) 5856-5862.

[11] L. Khriachtchev, O. Kilpelä, S. Karirinne, J. Keränen, T. Lepistö, Substrate-dependent crystallization and enhancement of visible photoluminescence in thermal annealing of Si/SiO2 superlattices, Applied Physics Letters, 78 (2001) 323-325.

[12] W. Li, D. Xia, H. Wang, X. Zhao, Hydrogenated nanocrystalline silicon thin film prepared by RF-PECVD at high pressure, Journal of Non-Crystalline Solids, 356 (2010) 2552-2556.

[13] S. Samanta, D. Das, Nanocrystalline silicon thin films from SiH4 plasma diluted by H2 and He in RF-PECVD, Journal of Physics and Chemistry of Solids, 105 (2017) 90-98.

[14] Z. Cen, J. Xu, Y. Liu, W. Li, L. Xu, Z. Ma, X. Huang, K. Chen, Visible light emission from single layer Si nanodots fabricated by laser irradiation method, Applied Physics Letters, 89 (2006) 163107.

[15] L. Khriachtchev, M. Räsänen, S. Novikov, Continuous-wave laser annealing of free-standing Si/SiO2 superlattice: Modification of optical, structural, and light-emitting properties, Journal of Applied Physics, 100 (2006) 053502.

[16] E. Werwa, A.A. Seraphin, L.A. Chiu, C. Zhou, K.D. Kolenbrander, Synthesis and processing of silicon nanocrystallites using a pulsed laser ablation supersonic expansion method, Applied Physics Letters, 64 (1994) 1821-1823.

[17] A. Chimmalgi, C.P. Grigoropoulos, K. Komvopoulos, Surface nanostructuring by nano,femtosecond laser-assisted scanning force microscopy, Journal of Applied Physics, 97 (2005) 104319.

[18] B.V. Kamenev, H. Grebel, L. Tsybeskov, Laser-induced structural modifications in nanocrystalline silicon/amorphous silicon dioxide superlattices, Applied Physics Letters, 88 (2006) 143117.

[19] S.J. Angus, A.J. Ferguson, A.S. Dzurak, R.G. Clark, Gate-Defined Quantum Dots in Intrinsic Silicon, Nano Letters, 7 (2007) 2051.

[20] A. Fujiwara, H. Inokawa, K. Yamazaki, H. Namatsu, Y. Takahashi, N.M. Zimmerman, S.B. Martin, Single electron tunneling transistor with tunable barriers using silicon nanowire metal-oxide-semiconductor field-effect transistor, Applied Physics Letters, 88 (2006) 053121.

[21] S. Tiwari, F. Rana, H. Hanafi, A. Hartstein, E.F. Crabbé, K. Chan, A silicon nanocrystals based memory, Applied Physics Letters, 68 (1996) 1377-1379.

[22] Y.T. Tan, T. Kamiya, Z.A.K. Durrani, H. Ahmed, Room temperature nanocrystalline silicon single-electron transistors, Journal of Applied Physics, 94 (2003) 633-637.

[23] A. Saboundji, T. Mohammed-Brahim, G. Andrä, J. Bergmann, F. Falk, Thin film transistors on large single crystalline regions of silicon induced by cw laser crystallization, Journal of Non-Crystalline Solids, 338-340 (2004) 758-761.

[24] Y. Helen, R. Dassow, M. Nerding, K. Mourgues, F. Raoult, J.R. Köhler, T. Mohammed-Brahim, R. Rogel, O. Bonnaud, J.H. Werner, H.P. Strunk, High mobility thin film transistors by Nd:YVO4-laser crystallization, Thin Solid Films, 383 (2001) 143-146.

[25] N.K. Mudugamuwa, A.A.D.T. Adikaari, D.M.N.M. Dissanayake, V. Stolojan, S.R.P. Silva, Reversible increase of photocurrents in excimer laser-crystallized silicon solar cells, Solar Energy Materials and Solar Cells, 92 (2008) 1378-1381.

[26] J.S. Im, R.S. Sposili, Crystalline Si Films for Integrated Active-Matrix Liquid-Crystal Displays, MRS Bulletin, 21 (2013) 39-48.

[27] S. Veprek, F.A. Sarott, Z. Iqbal, Effect of grain boundaries on the Raman spectra, optical absorption, and elastic light scattering in nanometer-sized crystalline silicon, Physical Review B, 36 (1987) 3344-3350.

[28] D.V. Tsu, B.S. Chao, S.R. Ovshinsky, S. Guha, J. Yang, Effect of hydrogen dilution on the structure of amorphous silicon alloys, Applied Physics Letters, 71 (1997) 1317-1319.

[29] K. Shimizu, O. Sugiura, M. Matsumura, High-mobility poly-Si thin-film transistors fabricated by a novel excimer laser crystallization method, IEEE Transactions on Electron Devices, 40 (1993) 112-117.

[30] S. Kazuhiro, S. Osamu, M. Masakiyo, On-Chip Bottom-Gate Polysilicon and Amorphous Silicon Thin-Film Transistors Using Excimer Laser Annealing, Japanese Journal of Applied Physics, 29 (1990) L1775.

[31] K. Sera, F. Okumura, H. Uchida, S. Itoh, S. Kaneko, K. Hotta, High-performance TFTs fabricated by XeCl excimer laser annealing of hydrogenated amorphous-silicon film, IEEE Transactions on Electron Devices, 36 (1989) 2868-2872.

Chapter 5

Persistent Photoconductivity studies in a-Si:H/nc-Si:H superlattice structures

Persistent photoconductivity (PPC) is an interesting phenomenon observed in number of superlattice structures. In PPC, current does not fall back to initial dark value after switching OFF the illumination, instead it shows a slow exponential decay. The PPC has been observed in superlattice structures made of doped GaAs and differently doped a-Si:H *(npnp, nipi)* etc [1-3]. In doped GaAs superlattice structure PPC was observed at 4K [4], but in a-Si:H doped *npnp* structures, the PPC was not restricted to low temperature but was observed at room temperature and even at higher temperatures. The excess conductivity after turning the illumination OFF and its slow decay has also been reported for variety of compound semiconductors including CdS nanorods [5] [6], ZnCdSe [7], ZnCdSe and CdSSe[8] a-InSe alloys[9], ZnO nanowires [10] and $SrTiO_3$ single crystals [11], porous silicon [12] etc [13] [14] [15-19]. Several models have been proposed in order to understand the origin of PPC in these structures. Hundhausen et al. [20] has proposed that the observed PPC in *nipi* structure could be due to trapping of the carriers in accepter like (AX) centers or could be due to separation of charge carriers at the interface whereas, in case of compound semiconductors, it could be due to random local potential fluctuation arising due to compositional

inhomogenities. Therefore, in order to understand about the presence of defect states or interface states in the a-Si:H/nc-Si:H superlattice structures detailed studies on PPC has been conducted. Though the structural and optoelectronic properties of these structures were studied earlier, however to the best of our knowledge no one has reported the observation of PPC in these superlattice structures.

In this chapter, a detailed study on persistent photoconductivity (PPC) in a-Si:H/nc-Si:H superlattice structures (where none of the layer is doped) has been presented. The PPC decay time constant, its dependence on exposure time, electric field, the effect of number of periods and layer thickness in superlattice structures on PPC has been studied in detail. A mechanism responsible for the observed PPC effect has also been proposed.

5.1 Measurement Details

Single and multilayer/superlattice structures of a-Si:H and nc-Si:H thin films prepared using both rf-PECVD and HWCVD technique were used for the PPC studies. For the preparation of thick (≥50 nm) individual layers of a-Si:H and nc-Si:H films in these superlattice structures, HWCVD technique has been used. Whereas for the superlattice structures with thin (≤30 nm) individual layers, rf-PECVD technique has been used. Superlattice structures consisting of two (02) and five (05) periods of alternate layers of a-Si:H and nc-Si:H were prepared using HWCVD technique on corning 1737 glass substrate. One pair of each a-Si:H and nc-Si:H together is defined one periods. The 5 periods structure had a total thickness of 700 nm (keeping the individual layer thickness equal at 70 nm) and two different 2 periods superlattice structures had a total thickness of 280 nm (with individual layer thickness of 70 nm) and 700 nm (with individual layer thickness of 175 nm) respectively. In these structures, the bottom layer was a-Si:H and top layer was nc-Si:H. The deposition

parameters for single layer films are mentioned in detail in Table 2.1 of Chapter 2. Superlattice structures with thin nc-Si:H and a-Si:H were prepared using rf-PECVD. In these structures, the bottom and top layers were retained to be nc-Si:H and total number of layers were kept as 7 (4 nc-Si:H and 3 a-Si:H layers). Further, the thickness of a-Si:H layer was kept constant at 10 nm whereas, the thickness of nc-Si:H layer was varied from 5-30 nm. Another sample having 20 nm thick nc-Si:H layer with total number of layers as 11 (6 nc-Si:H and 5 a-Si:H layers) was also prepared to study the influence of number of interface on PPC. The deposition parameters for these films are mentioned in detail in Table 2.6 & 2.7 of Chapter 2.

The PPC measurements were conducted in co-planner geometry using silver paste as electrodes about 1 mm apart. To ensure the contact to all layers, the superlattice structures were scratched before making the electrodes. Keithley 2450 source meter has been used for the PPC measurements and 100W halogen lamp was used for illumination. Figure 5.1 shows the sample structure and electrode geometry used for these measurements.

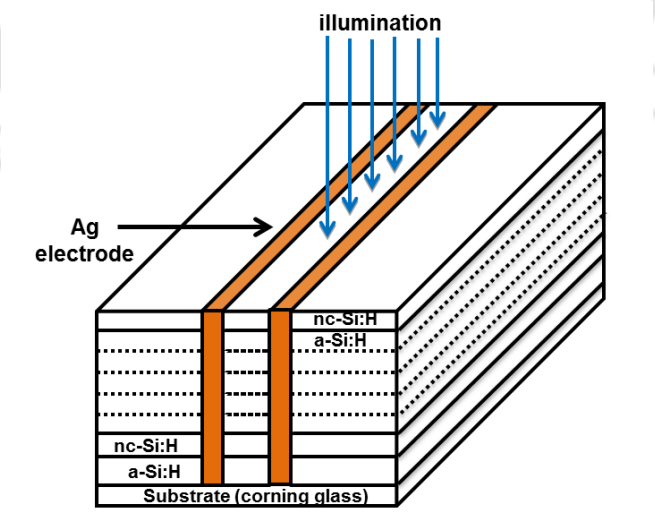

Figure 5.1: Schematic diagram of a-Si:H/nc-Si:H superlattice structure and electrode geometry (also shown in chapter 2).

5.2. Results and Discussion

5.2.1 PPC studies on thick individual layer of a-Si:H and nc-Si:H in a-Si:H/nc-Si:H superlattice structures prepared by HWCVD technique

Figure 5.2 (a) show the rise and decay of photo current of as deposited single layer a-Si:H and nc-Si:H thin films upon illumination and after the light was cut OFF. In case of single layer a-Si:H thin film, the photocurrent degrades under illumination in accordance with the well-known Staebler Wronski effect [21]. This is in contrast to the superlattice structure of 5 periods (Fig 5.2 (b)) where the photo current does not degrade under illumination instead the photo current initially rises fast and then slowly while the light is ON. Further, when light is turned OFF, current does not fall back to its dark value immediately, rather a slow exponential decay of current is observed. Even after a few hundred seconds of switching OFF the light, the dark current is slightly higher than its initial dark value. The slow decay part of the photocurrent after turning OFF the illumination is well described by single exponential decay function. It seems to follow the relation:

$$I = I_o \exp^{\frac{-t}{\tau}} \quad \ldots\ldots\ldots\ldots\ldots\ldots \quad 5.1$$

where I_o is the pre-exponential factor and τ is the decay time constant.

The PPC (%) is determined using relation as given below:

$$PPC(\%) = \frac{\Delta I_d}{I_d} \quad \ldots\ldots\ldots\ldots\ldots\ldots \quad 5.2$$

where, I_d is the dark current measured just before switching ON the illumination and ΔI_d is excess dark current after 180 sec of switching OFF the light.

Figure 5.3 (a, b) shows the rise and decay of the current at RT after annealing the 5 periods superlattice structures at two different temperatures; 70 ºC and 120 ºC, after exposure to

three different illumination duration of 30, 60 and 90 sec respectively. The dark current increases with the increase in annealing temperature, however PPC (%) decreases. The values of dark current, photo current, PPC and decay time constant for this structure, measured at RT, in as deposited states as well as after annealing at different temperature are listed in Table 5.1.

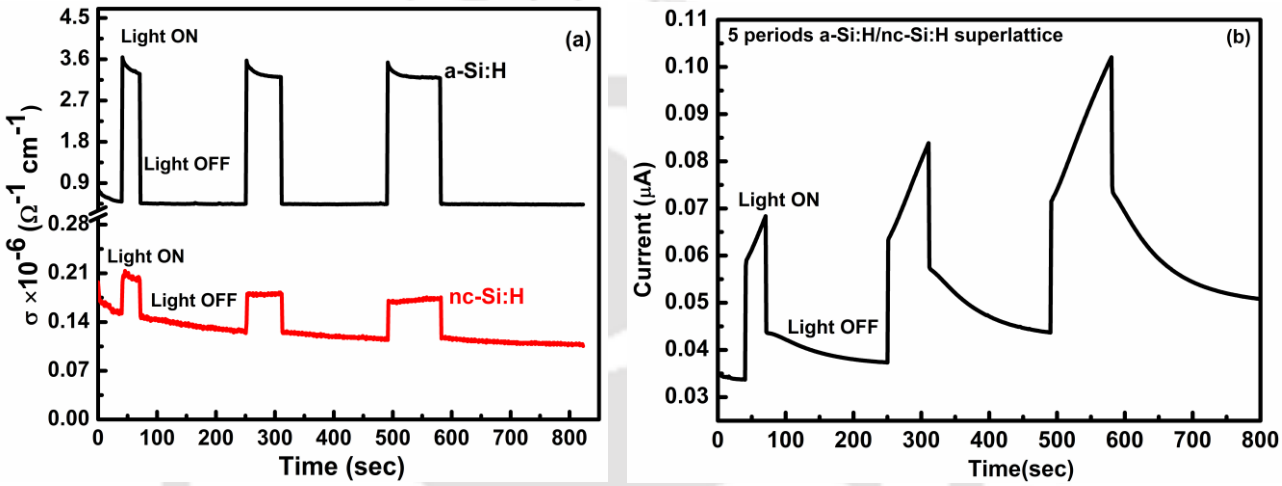

Figure 5.2: Rise and decay of photo conductivity of (a) single layer a-Si:H, nc-Si:H thin films and rise and decay of photo current of (b) 5 periods of a-Si:H/nc-Si:H superlattice.

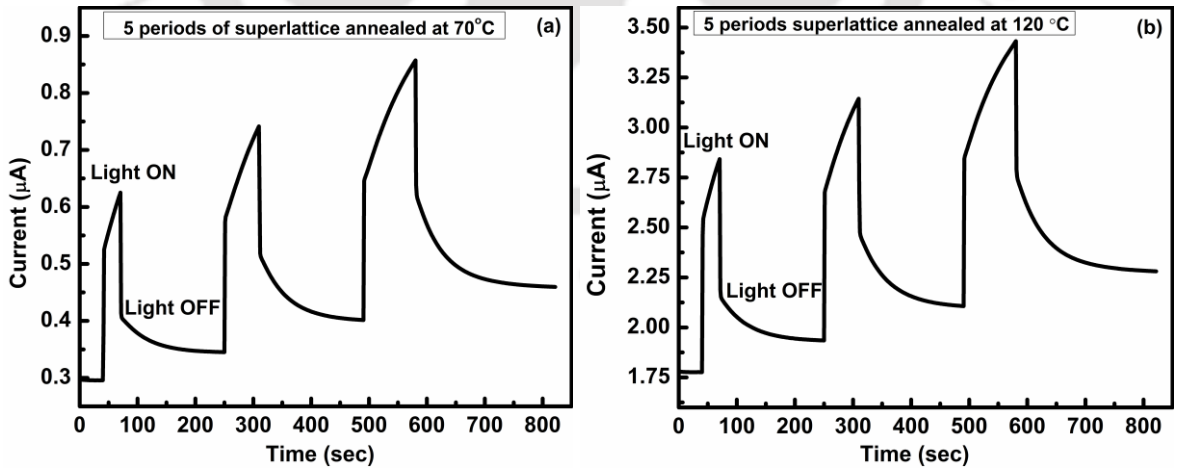

Figure 5.3: Rise and decay of photo current of 5 periods of superlattice structure annealed at (a) 70 ℃ and (b) 120 ℃ measured at RT.

Table 5.1: The values of dark current, photo current, PPC and the decay time constant of the thick individual superlattice structures prepared by HWCVD technique

Type (individual layer thickness)	Annealed temperature	I_{dark} (μA) at RT	I_{photo} (μA) at RT	I_{ppc} μA) at RT	PPC (%)	τ (sec)		
						Exposure Time		
						30 (sec)	60 (sec)	90 (sec)
5 periods (70 nm)	as deposited	0.03	0.06	0.04	33	91.20	80.54	76.14
	70 °C	0.29	0.52	0.35	20	45.96	45.95	46.01
	120 °C	1.77	2.45	1.93	9	47.03	47.31	47.75
2 periods (175 nm)	as deposited	0.13	0.32	0.15	15	44.20	42.70	41.80
2 periods (70 nm)	as deposited	0.053	0.220	0.059	11	69.29	67.19	64.77

The excess conductivity after turning the illumination OFF and its slow decay has also been reported for variety of materials [20, 22-24]. Several models have been proposed to understand the origin of PPC in semiconductors. In $Al_xGa_{1-x}As$/GaAs hetero-structure [23], two mechanism giving rise to PPC have been identified as: a) electron photo excitation from the donor like centers (DX) in highly doped $Al_xGa_{1-x}As$ layer and b) electron-hole generation in bulk GaAs layer with the charge separation at the interfaces. In case of doped a-Si:H based *n-p-n-p* structure, PPC is believed to be due to trapping of the carriers at the centers made by P-B complexes, which are in poor communication with the rest of the material [25]. Hundhausen et.al [20] suggested that PPC in *n-i-p-i* and *n-p-n-p* structures are caused by trapping of holes in acceptor like centers (AX) in the p-type regions which leave behind long lived electrons in n type region that contribute to an excess dark conductivity after illumination. Su et.al [26] claimed that dangling bonds are responsible for PPC in amorphous *p-n-p-n* structures. The PPC is believed to be either due to the presence of random local potential fluctuation arising as a result of compositional in-homogeneities

causing the photo generated electron hole pair to spatially separate before these recombine or due to the presence of DX centers, which capture electrons and re-emit these slowly resulting in excess conductivity even after the illumination is OFF. In present case, PPC is observed even after few hundred second of switching OFF the light, whereas single layer a-Si:H and nc-Si:H do not show any PPC. After each successive exposure, the relaxation time τ decreases for the as deposited sample but for annealed samples it was observed that, τ remains same for different exposure time (Table 5.1).

In our case, the role of P-B complex or AX or DX is ruled out as these superlattice structures are made without any doping. The trapping of photo generated charge carriers at the interface or the separation of carriers due to band bending caused by in-homogeneities thus appears to be more likely cause of the observed PPC. In order to understand the origin of the observed PPC, the Electric field dependence of photoconductivity (Fig 5.4 (a)) and PPC are also measured for the structure annealed at 120 °C. It is observed that the photo current varies linearly with applied field; however, the extent of PPC reduces with the increase in applied field as shown in Fig 5.4(b).

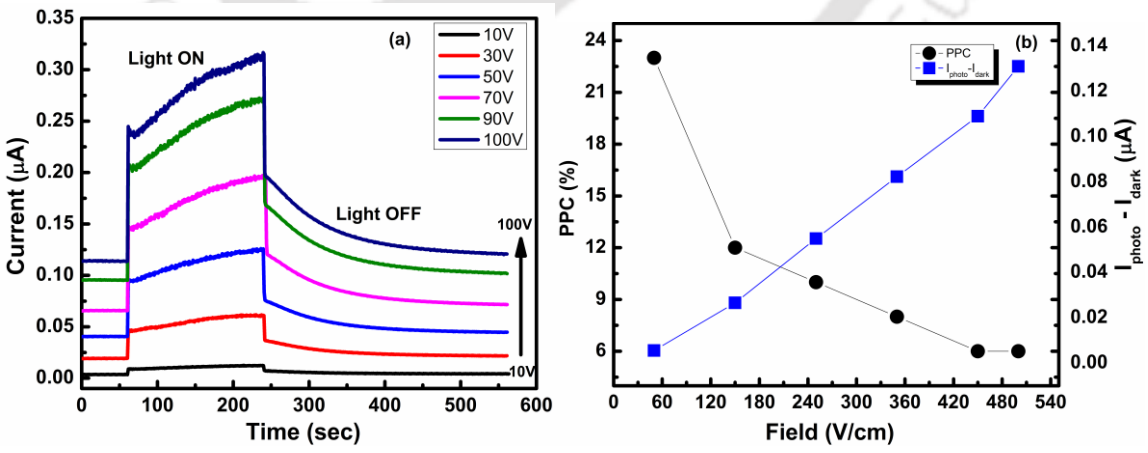

Figure 5.4: a) Rise and decay of the photo current with the variation of external applied field, b)Variation of PPC (%) and photo current with the change of external applied field in 5 periods superlattice structures.

In case of a-Si:H/nc-Si:H superlattice structures, two different band gaps of a-Si:H and nc-Si:H results in modulation of the band energies which is accompanied by built-in electric field that are expected to act strongly on mobile charge carriers and thus effect their recombination kinetics. Figure 5.5 shows the schematic band diagram of a-Si:H/nc-Si:H structure assuming the same electron affinity, however, different band gap and activation energy for the a-Si:H and nc-Si:H layers. The values of E_g and E_c-E_f are estimated from the transmission spectra and electrical conductivity measurements on single layer a-Si:H and nc-Si:H films. The value of E_g for a-Si:H and nc-Si:H was found to be 1.9 and 2.1 eV respectively as mentioned in Table 3.2 of chapter 3, whereas, the activation energy (E_c-E_f) for a-Si:H and nc-Si:H was found to be 0.48 eV and 0.52 eV respectively. In this picture, electrons in the nc-Si:H region, can move freely to the a-Si:H region, however, the holes in a-Si:H region are likely to be trapped in the interface states. When the light is shone, the photo generated carriers are generated, some of these carriers recombine instantaneously whereas, other drift towards the interfaces due to the field at the junction. When there is no externally applied field in lateral direction or this external field is low, the photo generated carriers move towards the depth due to the in-built field at the junction. Though the field at the a-Si:H/nc-Si:H junction is not as high as it is in case of pn junction (which is ~ 10^4 V/cm), this field is high enough to drag the carriers towards the depth at low externally applied field in the lateral direction (Fig 5.6). The electrons move towards the conduction band (CB) of different layers whereas, holes to valence band. Some of the electrons are trapped in the CB tails states or defect states in a-Si:H layers, whereas, the holes are trapped at the interface states as shown in the schematic band diagram Fig 5.5. Thus, the electrons and holes get physically separated preventing their recombination. When the light is OFF,

these trapped carriers are remitted to the extended states and recombine slowly resulting in slow exponential decay of the photo current. In presence of externally applied field, the photo generated carriers experience two fields, one towards the depth due to the in-built field at the junction and other, external field in the lateral direction. When external field is high, the carriers are dragged to the lateral direction instead of moving towards the depth resulting in decrease in PPC (%) as shown in Fig. 5.4 (b). The origin of PPC is understood in terms of competition between carriers transport in the lateral direction due to external field and along the depth due to band bending at a-Si:H/nc-Si:H interfaces. Carriers trapped in the interfaces states or the separations of carriers due to band bending are likely to be responsible for observed PPC.

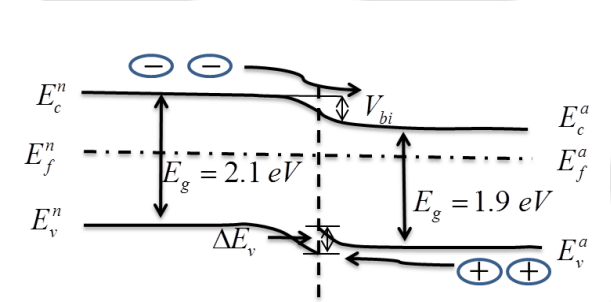

Figure 5.5: Schematic band diagram of a-Si:H/nc-Si:H superlattice structure

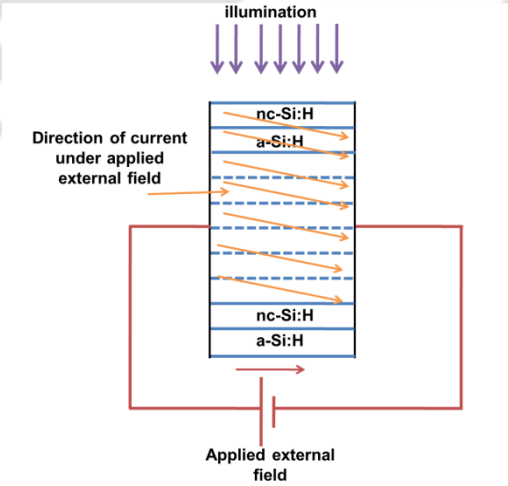

Figure 5.6: Direction of current under the applied external field in the superlattice structure.

In order to check, whether PPC (%) depend on the number of layers in these superlattice structures, more such structures with only 2 periods were fabricated keeping the total thickness constant at 700 nm. The effect of layer thickness on PPC (%) was also studied by preparing one more superlattice structure of 2 periods with individual layer thickness of 70 nm each; the total thickness of 280 nm. Figure 5.7 shows the rise and decay of the photo current (in as deposited samples) across both the superlattice structures of 2 periods with two different individual layer thicknesses (175 and 70 nm each). The values of dark current, photo current, PPC and decay time constant of these films are listed in Table 5.1.

It is observed that with the decrease in the number of periods from 5 to 2, PPC (%) decreased from 33% to 15% (Table 5.1). There is not much change in PPC (%) for the superlattice structure of 2 periods with individual layer thickness of 70 nm and 175 nm each, however the PPC (%) in both the 2 periods superlattice structures is lower as compared to 5 periods superlattice structure (Table 5.1). These results imply that when the numbers of period are more, the numbers of interface are more resulting in more trapping of charge carriers which further results in increase in PPC (%).

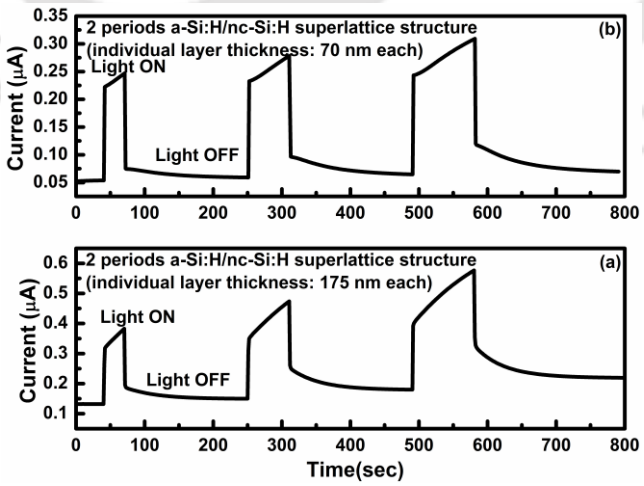

Figure 5.7: Rise and decay of photo current of 2 periods superlattice structures of individual layer thickness of (a) 175 nm each and (b) 70 nm each.

5.2.2 PPC studies on thin individual layer of a-Si:H and nc-Si:H in a-Si:H/nc-Si:H superlattice structures prepared by rf-PECVD technique

Figure 5.9 (a, b) show the rise and decay of photocurrent for the thin individual layers superlattice structures prepared using rf-PECVD technique. No PPC was observed for the single layer films (Fig 5.8) as well as superlattice structures of 7 layers (Fig 5.9 a) with nc-layer thickness in the range of 5-20 nm (with the total thickness of 50-110 nm). However, the superlattice structures with nc-Si:H layer thickness of 30 nm (total thickness of 150 nm) and the superlattice structure of 11 layers with nc-Si:H layer thickness of 20 nm (total thickness of 170 nm) show PPC illustrated by appreciable excess current when the light is turned OFF (Fig. 5.9 (b)). The values of dark current, photo current, PPC (%) and decay time constant for these films are listed in Table 5.2.

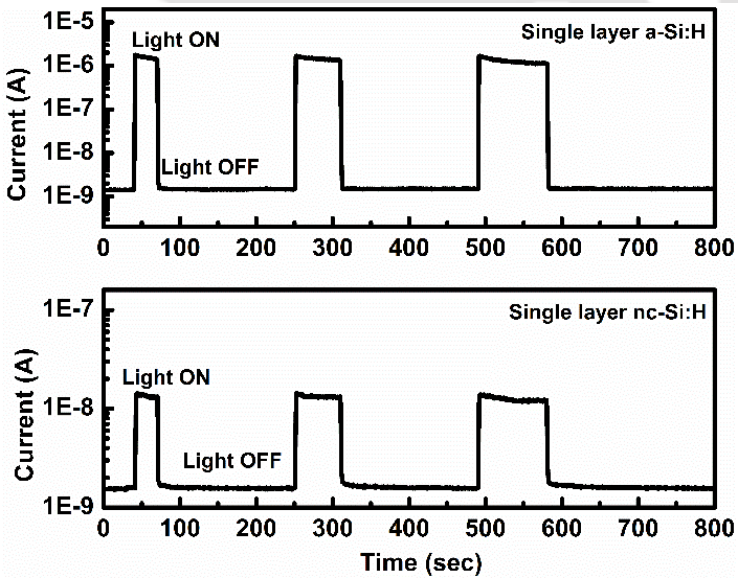

Figure 5.8: Rise and decay of the photo current across single layer of a-Si:H and nc-Si:H thin films.

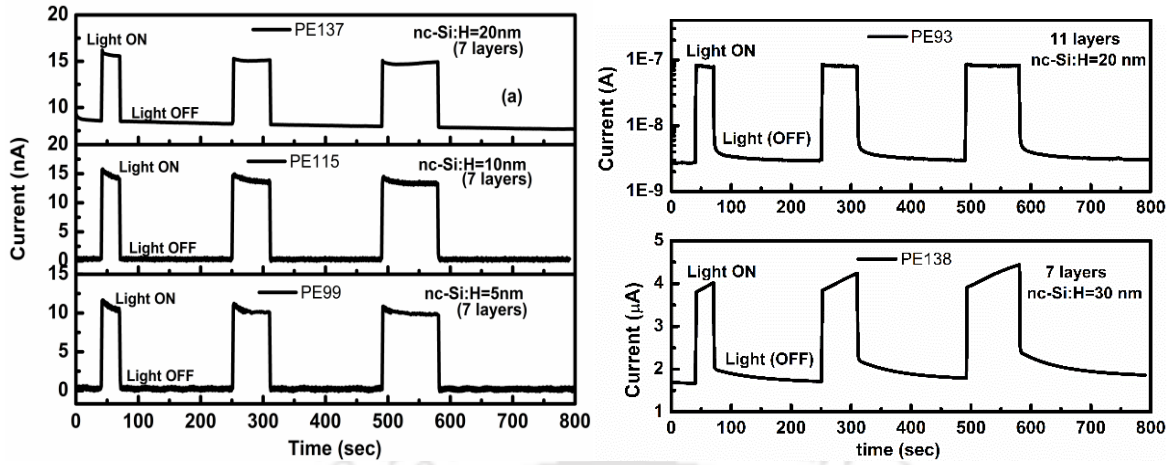

Figure 5.9: Rise and decay of the photo current in a-Si:H/nc-Si:H superlattice with nc-Si:H layer thickness of (a) 5 nm, 10 nm, 20 nm (7 layers) and (b) 30 nm (7 layers) and 20 nm (11 layers) structures.

Table 5.2: The values of dark current, photo current, PPC and the decay time constant of the thin superlattice structures prepared by rf-PECVD technique

Type (super lattice)	Annealed temperature	I_{dark} (μA) at RT	I_{photo} (μA) at RT	I_{ppc} μA) at RT	PPC (%)	τ (sec)		
						Exposure Time		
						30 (sec)	60 (sec)	90 (sec)
7 layer nc-Si:H: 30nm	as deposited	1.67	3.77	1.71	2	67.97	69.68	72.10
11 layer nc-Si:H:20 nm	as deposited	2.72×10^{-3}	8.22×10^{-3}	3.0×10^{-3}	10	21.24	23.00	26.24

It may be noted here that the observed PPC (%) in the present case is small compared to that of superlattice structures with thick sublayers of a-Si:H and nc-Si:H films prepared using HWCVD technique. However, with the increase in the number of layers from 7 (total thickness of 150 nm) to 11 (total thickness 170nm), the PPC (%) was found to increase similar to the superlattice structures prepared by HWCVD technique. It may also be noted that the 7 layer superlattice structures with total thickness of ≤ 110 nm do not show any

PPC. The absence of PPC for these superlattice structures with low total thickness as well as low individual layer thickness could be due to i) insufficient absorption of light (when the total thickness is low) resulting in very few photogenerated carriers and ii) due to possible tunneling of carriers between a-Si:H and nc-Si:H layers when the thickness of nc-Si:H is low (5-10 nm). As the layer thickness is increased, the band bending, depletion width and thickness of undepleted region is likely to change. This may not allow all the carriers to tunnel through and these may get trapped at the interface in between a-Si:H and nc-Si:H layers resulting in observed PPC. With increase in number of layers, the number of such interfaces as well as total thickness increases which result in the observed PPC for 11 layer structure with 20 nm thick nc-Si:H layers and no PPC for 7 layer structure with 20 nm thick nc-Si:H layers.

5.3 Conclusion

In summary, we have studied the PPC in undoped a-Si:H/nc-Si:H superlattice under different conditions. The photo current varies linearly with applied external field. However, the extent of PPC decreases with the increase in applied external field. PPC is observed only in layered structure and not in the individual single layer films. There is not much change in PPC (%) for the superlattice structure of 2 periods with individual layer thickness of 70 nm (total thickness of 280 nm) and 175 nm (total thickness of 700 nm) each, however the PPC (%) in both the 2 periods superlattice structures is lower as compared to 5 periods (total thickness of 700 nm) superlattice structure. These results imply that when the numbers of period are more, the numbers of interface are more resulting in more trapping of charge carriers and hence higher PPC (%). Similarly, for the thin superlattice structures as well, the PPC (%) was found to increase with the increase in the number of layers. However, for very

thin individual layer (≤10 nm) as well as low total thickness (≤110 nm) in these superlattice structures, there was no PPC and this could be due to insufficient absorption of light resulting in very few photogenerated carriers and also possible tunneling of the carrier between the thin layers of a-Si:H (10nm) and nc-Si:H (5-10nm) films. Thus, the origin of PPC is understood in terms of competition between carrier transport in the lateral direction due to external field and along the depth due to band bending at a-Si:H/nc-Si:H interfaces. Carriers trapped in the interfaces states and/or the separations of carriers due to band bending are likely to be responsible for observed PPC.

5.4 References

[1] G.H. Döhler, H. Künzel, K. Ploog, Tunable absorption coefficient in GaAs doping superlattices, Physical Review B, 25 (1982) 2616-2626.

[2] M. Hundhausen, L. Ley, R. Carius, Carrier Recombination Times in Amorphous-Silicon Doping Superlattices, Physical Review Letters, 53 (1984) 1598-1601.

[3] J. Kakalios, H. Fritzsche, Persistent Photoconductivity in Doping-Modulated Amorphous Semiconductors, Physical Review Letters, 53 (1984) 1602-1605.

[4] K. Ploog, G.H. Döhler, Compositional and doping superlattices in III-V semiconductors, Advances in Physics, 32 (1983) 285-359.

[5] G.S. Paul, P. Agarwal, Persistent photocurrent and decay studies in CdS nanorods thin films, Journal of Applied Physics, 106 (2009) 103705.

[6] D. Azulay, O. Millo, S. Silbert, I. Balberg, N. Naghavi, Where does photocurrent flow in polycrystalline CdS?, Applied Physics Letters, 86 (2005) 212102.

[7] J.Y. Lin, H.X. Jiang, Relaxation of stored charge carriers in a $Zn_{0.3}Cd_{0.7}Se$ mixed crystal, Physical Review B, 41 (1990) 5178-5187.

[8] H.X. Jiang, J.Y. Lin, Percolation transition of persistent photoconductivity in II-VI mixed crystals, Physical Review Letters, 64 (1990) 2547-2550.

[9] A.S. Maan, D.R. Goyal, A. Kumar, Steady-state photoconductivity and decay kinetics in thin films of a-In20Se80, Journal of Non-Crystalline Solids, 110 (1989) 53-60.

[10] D. Cammi, C. Ronning, Persistent Photoconductivity in ZnO Nanowires in Different Atmospheres, Advances in Condensed Matter Physics, 2014 (2014) 5.

[11] M.C. Tarun, F.A. Selim, M.D. McCluskey, Persistent Photoconductivity in Strontium Titanate, Physical Review Letters, 111 (2013) 187403.

[12] M.N. Islam, P.S. Dobal, H.D. Bist, S. Kumar, Light and thermally induced effects in porous silicon layers, Solid State Communications, 107 (1998) 43-46.

[13] H.J. Queisser, Nonexponential Relaxation of Conductance near Semiconductor Interfaces, Physical Review Letters, 54 (1985) 234-236.

[14] D.V. Lang, R.A. Logan, Large-Lattice-Relaxation Model for Persistent Photoconductivity in Compound Semiconductors, Physical Review Letters, 39 (1977) 635-639.

[15] D.V. Lang, R.A. Logan, M. Jaros, Trapping characteristics and a donor-complex (DX) model for the persistent-photoconductivity trapping center in Te-doped $Al_xGa_{1-x}As$, Physical Review B, 19 (1979) 1015-1030.

[16] H.J. Queisser, D.E. Theodorou, Decay kinetics of persistent photoconductivity in semiconductors, Physical Review B, 33 (1986) 4027-4033.

[17] M.T. Hirsch, J.A. Wolk, W. Walukiewicz, E.E. Haller, Persistent photoconductivity in n-type GaN, Applied Physics Letters, 71 (1997) 1098-1100.

[18] J.Z. Li, J.Y. Lin, H.X. Jiang, J.F. Geisz, S.R. Kurtz, Persistent photoconductivity in $Ga_{1-x}In_xN_yAs_{1-y}$, Applied Physics Letters, 75 (1999) 1899-1901.

[19] P.M. Mooney, Deep donor levels (DX centers) in III-V semiconductors, Journal of Applied Physics, 67 (1990) R1-R26.

[20] M. Hundhausen, L. Ley, Model for persistent photoconductivity in doping-modulated amorphous silicon superlattices, Physical Review B, 32 (1985) 6655-6662.

[21] D.L. Staebler, C.R. Wronski, Reversible conductivity changes in discharge-produced amorphous Si, Applied Physics Letters, 31 (1977) 292-294.

[22] S.-H. Choi, B.-S. Yoo, C. Lee, J. Jang, Doping and annealing effects on persistent photoconductivity in doping-modulated amorphous-silicon superlattices, Physical Review B, 36 (1987) 6479-6485.

[23] A. Kastalsky, J.C.M. Hwang, Study of persistent photoconductivity effect in n-type selectively doped AlGaAs/GaAs heterojunction, Solid State Communications, 51 (1984) 317-322.

[24] R.J. Freitas, K. Shimakawa, T. Wagner, The dynamics of photoinduced defect creation in amorphous chalcogenides: The origin of the stretched exponential function, Journal of Applied Physics, 115 (2014) 013704.

[25] S.C. Agarwal, S. Guha, Amorphous silicon doping superlattices, Journal of Non-Crystalline Solids, 77-78 (1985) 1097-1100.

[26] F.C. Su, S. Levine, P.E. Vanier, F.J. Kampas, Light-induced excess conductivity and the role of argon in the deposition of doping-modulated amorphous silicon superlattices, Applied Physics Letters, 47 (1985) 612-614.

Chapter 6

Density of states measurement in a-Si:H/nc-Si:H superlattice structures

Superlattice/Multilayer structures of hydrogenated amorphous (a-Si:H) and nanocrystalline (nc-Si:H) silicon exhibit interesting properties such as improved photosensitivity, enhanced carrier mobility and photonic and plasmonic enhancement etc. [1-7] as discussed in detail in Chapter 1. However, in multilayered electronic devices, the interface states between the sub layers may act as recombination centers, thereby having an important effect on controlling the transport mechanism and overall performance of these devices. In addition to these interface states, information about the density of localized states in the gap in semiconductors is essential for understanding and improving their optoelectronic properties because these states also act as recombination centers and traps. Lowering these states can have the dual effect of reducing recombination and facilitating a shift in the Fermi level by doping, illumination, etc.

Several methods have been used to determine the density of defect states, including field effect measurements [8-11], capacitance-voltage measurements [12,13], tunneling current measurements [14], isothermal capacitance transient spectroscopy [15], transient current spectroscopy [16], transient voltage spectroscopy [17] , deep level transient spectroscopy [18] and Space-charge limited current (SCLC) [19-26] etc. Of these measurements, Space-charge

limited current (SCLC) measurements are the simplest method for determining the DOS in amorphous and crystalline materials. SCLC has advantages compared with other methods such as transient current spectroscopy [16], photoconductivity measurements [27], and phase shift analysis of the modulated photocurrent [28] because these steady state measurement do not require any assumptions regarding the charge carrier emission times from traps. This method has been used extensively to obtain information about the deep traps in crystalline semiconductors [19-26]. In this method, the *I-V* characteristics of the samples are measured over a large range of electric field. These non-ohmic *I-V* characteristics are affected by the trap states in the materials and can be used to calculate the DOS. The measurements are performed using ohmic [19, 29] and Schottky junction [30] contacts.

In this chapter, density of states (DOS) studies across single layers and superlattice structures of a-Si:H and nc-Si:H thin films have been presented. The DOS in single layer a-Si:H and a-Si:H/nc-Si:H superlattice structures, fabricated using hot filament chemical vapour deposition (HWCVD) technique, have been deduced from space charge limited current (SCLC) measurements in sandwich geometry. We used a Schottky diode configuration, *ITO (Indium Tin Oxide)/a-Si:H/Ag* and *ITO{a-Si:H/nc-Si:H}$_n$/Ag*, for these measurements where *ITO/a-Si:H* acted as a Schottky junction whereas, *Ag/a-Si:H* and *Ag/nc-Si:H* acted as an ohmic junction. The *I-V* characteristics in the nonlinear region were used to estimate the DOS in single layer a-Si:H and a-Si:H/nc-Si:H superlattice structures. In single layer films, the injected charge from the metal to semiconductor (Ag to a-Si:H) was trapped in the DOS in the band gap, whereas in superlattice structures, the charge redistributed itself between the defect states in the band gap region as well as at the interface between the nc-Si:H and a-Si:H layers.

6.1 Measurement Details

Single layer a-Si:H and nc-Si:H films and superlattice structures with alternate layers of a-Si:H and nc-Si:H (with two and five layers of each type) prepared using HWCVD technique were used for DOS studies. Single layer films and superlattice structures fabricated on Corning 1737 glass substrate was used to obtain transport measurements in coplanar geometry, whereas the films on ITO-coated glass substrate were used to acquire SCLC measurements in sandwich geometry. In the superlattice structures, the individual layer thickness was kept constant at 70 nm each, with the total thickness of 280 nm and 700 nm for 2 periods and 5 periods superlattice structures respectively. Two and five layers of each a-Si:H and nc-Si:H may be defined as two and five periods. In these superlattice structures, the bottom layer was a-Si:H and topmost layer was nc-Si:H. The deposition parameters for the single layer films and individual layer thickness in the superlattice structures are mentioned in detail in Table 2.1 & 2.5 of Chapter 2.

SCLC measurements were performed in sandwich geometry using silver paste as the top electrode and ITO as the bottom electrode. I-V measurements were performed using a Keithley 2450 source meter. A schematic of the electrode geometry used to perform the SCLC measurements across superlattice structure is shown in Fig. 6.1. It has been reported earlier that SCLC measurements have been performed for *n-i-n* [29], Schottky diode [30] and *p-i-n* diode structures. In the Schottky diode configuration, both the charge carriers, i.e., electron and holes, contribute to SCLC, whereas in the n-i-n structures (the preferred structure for SCLC measurements), the n layer inject electrons into the insulator and block the holes, thus only the electrons contribute to SCLC. However, it has been reported that there is only a small difference in DOS obtained in both structures, therefore in the present work, the Schottky diode configuration has been used for these studies.

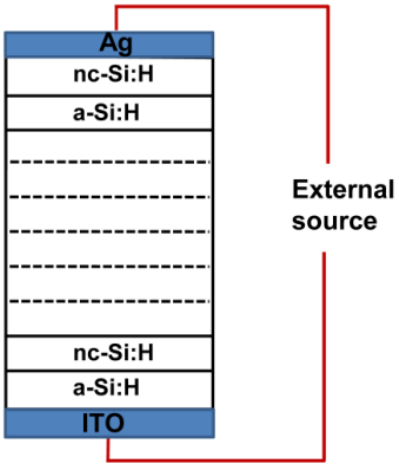

Figure 6.1: Schematic of the electrode geometry used to perform SCLC measurements in a-Si:H/nc-Si:H superlattice structures (also shown in chapter 2)

6.2 Theory

Den Boer's step by step [29] method is considered as the simplest method for estimating the DOS because in this case, the spatial variation in DOS is neglected. When the voltage difference changes from V_1 to V_2, the shift in the Fermi energy level $\left(E_{fn}\right)$ is given as follows:

$$\Delta E_{fn} = kT \ln\left(\frac{I_2 V_1}{I_1 V_2}\right) \ldots\ldots\ldots\ldots\ldots\ldots (6.1)$$

In the nonlinear region of *I-V*, the charge density Q_t injected into the trap states is related to the change in voltage $\Delta V = \left(V_2 - V_1\right)$ as follows:

$$Q_t = \frac{\varepsilon_s \chi \Delta V}{d} = qd \int_{E_{fn}}^{E_{fn}+\Delta E_{fn}} g(E)dE = qdg(E)\Delta E_{fn} \ldots\ldots\ldots\ldots (6.2)$$

The factor χ accounts for the non-uniformity of the space charge and is taken as a constant (χ = 2), ε_s is the semiconductor permittivity (ε_s = 105.31 × 10^{-12} Fm^{-1}; dielectric constant of silicon = 11.9), q is the electronic charge, d is the thickness of the film, and $g(E)$ is the DOS distribution in the a-Si:H film around the Fermi level.

For a sufficiently small ΔV, $g(E)$ can be assumed to be constant between E_{fn} and $E_{fn}+\Delta E_{fn}$. From Eq. (6.2), the DOS is given by,

$$g(E)=\frac{\chi\varepsilon_s\Delta V}{qd^2\Delta E_{fn}} \qquad \ldots\ldots\ldots\ldots (6.3)$$

Using the values of ΔV and ΔE_{fn}, the distribution of the DOS can be estimated using Eq. (6.3).

6.3 Results and Discussion

In density of states studies, the SCLC measurements was carried out on single layer a-Si:H and a-Si:H/nc-Si:H superlattice structures in sandwiched geometry. Figure 6.2 (a, b) and 6.3 (a, b) show the dark *I-V* curves in sandwich geometry for single as well as superlattice structures at room temperature (RT) after annealing it at 150 ºC. Amorphous silicon films show an asymmetric nonlinear *I-V* curve (Fig 6.2 (a)), where in forward bias condition, the current increase exponentially with the applied field, with a diode ideality factor being ~2. Whereas, in the nc-Si:H film, the variation of current is linear and symmetric with the applied field (Fig 6.2(b)). The conductivity of a-Si:H and nc-Si:H was found to be 4.3×10^{-9} $\Omega^{-1}cm^{-1}$ and 1.1×10^{-5} $\Omega^{-1}cm^{-1}$ respectively in sandwich geometry (Electric field $<1\times10^4$ V/cm); the dark conductivity of nc-Si:H films at 300 K is more than 3 order of magnitude higher as compared to a-Si:H films under forward bias condition. Figure 6.3 (a, b) show the dark *I-V* characteristics of a-Si:H/nc-Si:H (2 and 5 periods) superlattice structures at RT after annealing these films at 150 ºC. *I-V* curve across the superlattice structures were also found to be asymmetric and non-linear similar to a-Si:H film with the diode ideality factor being ~2 and current having same order of magnitude as that for single layer a-Si:H film.

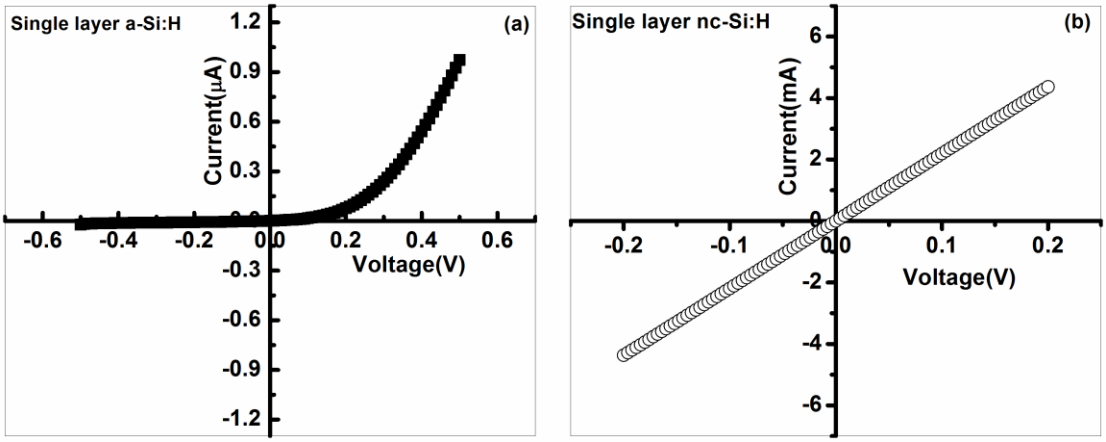

Figure 6.2: I-V across single layer ***(a)*** *a-Si:H and* ***(b)*** *nc-Si:H in sandwich geometry.*

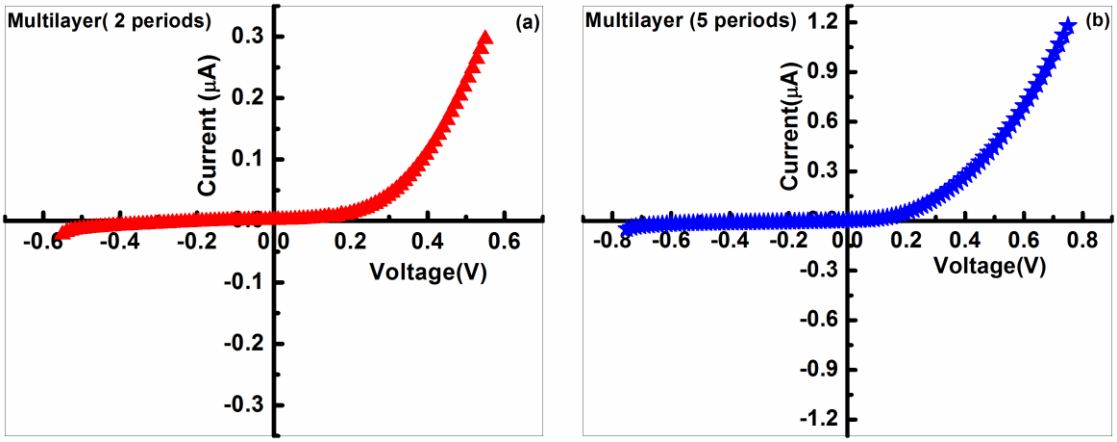

Figure 6.3: I-V across total a-Si:H/nc-Si:H (a) 2 periods and (b) 5 periods superlattice structures in sandwich geometry.

Since the conductivity of a-Si:H, is much less compared to nc-Si:H film and the thickness of both a-Si:H and nc-Si:H were kept same in these superlattice structures, therefore, it can be assumed that the entire voltage is dropped across a-Si:H layers. Now we can reconstruct the equivalent *I-V* curve for one pair of a-Si:H/nc-Si:H structure in both the superlattice structures, where voltage is half and one fifth of the total voltage drop across the entire structure of 2 periods and 5 periods superlattice structures respectively, whereas the current is same as earlier since the layers are in series. Figure 6.4 (a) shows the only forward bias *I-V* curve in log–log scale for the single layer a-Si:H, whereas Fig. 6.4 (b,c) are reconstructed *I-V* plot for single pair

of a-Si:H/nc-Si:H in superlattice structure for both the samples (2 and 5 periods). It was observed that *I-V* curve obey the power law i.e $I \alpha V^m$, with different values of exponent in different regions of the curve. The value of m for different region is shown in Fig. 6.4 (a-c). In the low field region, where the current is Schottky limited, the exponent is less than 1. Further for electric field >10^4 V/cm, the current increases sharply with the exponent greater than 2.0, which could be due to the onset of Space charge limited conduction in these structures.

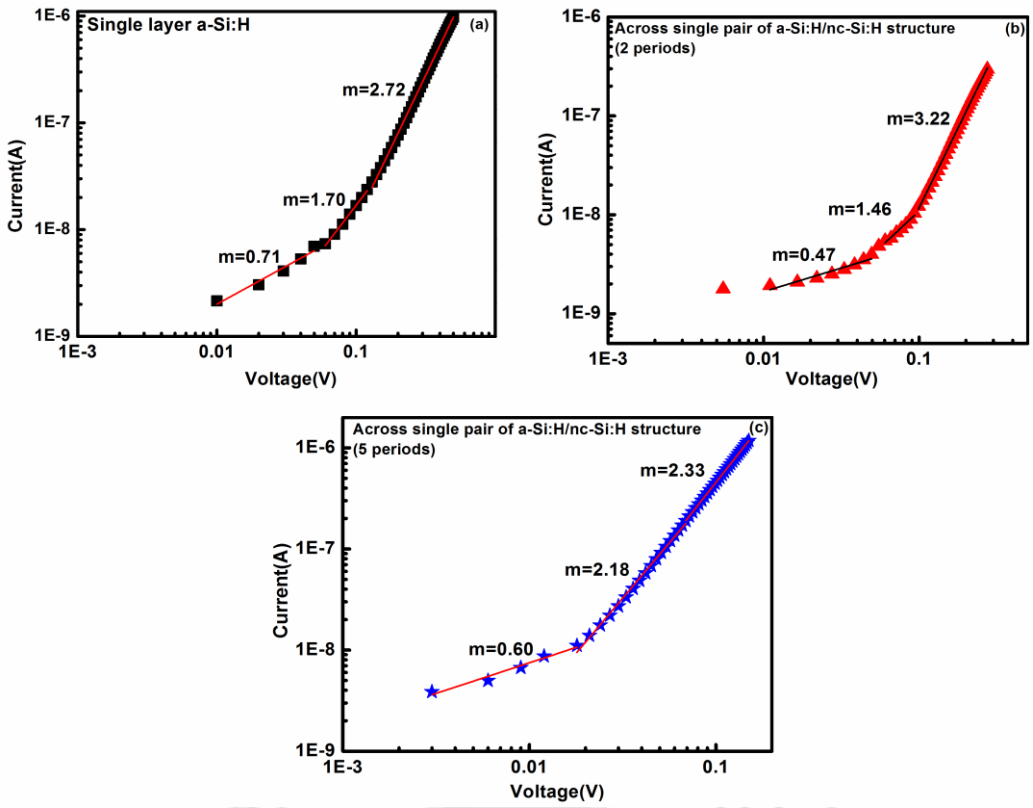

Figure 6.4: I-V across (a) single layer a-Si:H film, (b) 2 periods and (c) 5 periods superlattice structures (across single pair of a-Si:H/nc-Si:H).

The region with $m > 2$ of *I-V* characteristics were used for the estimation of shift in Fermi level using Eq. 6.1 and Density of states using Eq. 6.3. For the estimation of DOS as a function of shift in Fermi energy, the initial field (>1×10^4 V/cm) was kept constant for the given samples. The variation of DOS with the change in ΔE_{fn} is shown in Fig. 6.5 (a) for both single as well as

superlattice structures. It is observed that DOS is high for the superlattice structures than that for single layer a-Si:H film. Further, DOS does not depend on ΔE_{fn} for single layer a-Si:H film, however, a little variation with ΔE_{fn} is observed for superlattice structures. The average value of DOS over the entire range of ΔE_{fn} is also estimated from the slope of ΔV verse ΔE_{fn} (Fig. 6.5 (b)) using Eq. 6.3 and the values of *g(E)* are mentioned in Fig 6.5 (b). It is observed that ΔV verse ΔE_{fn} curves overlap for both superlattice structures irrespective of number of layers. It has also been observed that the DOS obtained across superlattice structures of both the periods (2 and 5) is almost same and is higher by a factor of 5 as compared to single layer a-Si:H film.

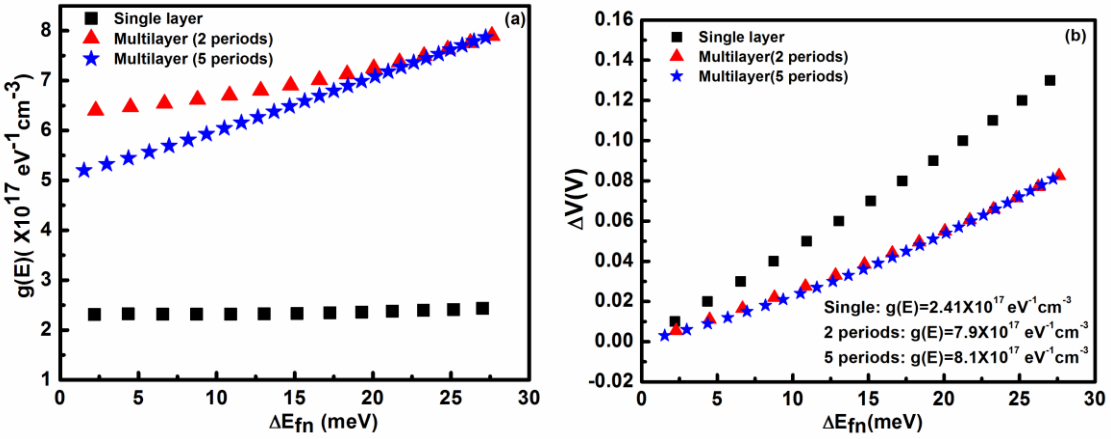

Figure 6.5: (a) Variation of DOS and (b) ΔV verse ΔE_f across single, 2 periods and 5 periods superlattice structures (across single pair of a-Si:H/nc-Si:H).

In our case, the DOS obtained across a-Si:H film was ~10^{17} $eV^{-1}cm^{-3}$, typical of a-Si:H samples, however for both the superlattice structures it was ~10^{18} $eV^{-1}cm^{-3}$. It may, therefore be assumed that the observed difference in DOS in case of single layer and superlattice films (Fig. 6.5(a)) might arise due to the presence of interface states between a-Si:H and nc-Si:H layers in these superlattice structures. These interface states were also found to be responsible for observed PPC in these superlattice structures as discussed in our previous chapter 5. The rise and decay of the photo current (in coplanar geometry) for these superlattice structures are shown in Fig 5.7 (b) (2 periods) and Fig 5.2 (b) (5 periods) of Chapter 5.

In order to understand the higher DOS in superlattice structure, the equivalent band diagram was considered knowing the bandgap and activation energy of single layer a-Si:H and nc-Si:H films. Figure 6.6 shows the band diagram of a-Si:H/nc-Si:H superlattice structure with ITO as the base electrode and Ag as the top electrode. In a-Si:H/nc-Si:H superlattice structure, the difference in band gaps of nc-Si:H and a-Si:H results in band bending giving rise to a built-in electric field at the interface. This built-in field influences the charge transport across the interface and affect the carrier recombination kinetics. The junction at ITO/a-Si:H interface, which is found to be rectifying in our case, also results in built-in electric field under no bias condition. In absence of any bias, the current density from semiconductor to ITO $\left(J_{sc;ITO}\right)$ must be equal and opposite of current density from ITO to semiconductor $\left(J_{ITO;sc}\right)$. Under the influence of external bias, which forward biases the ITO semiconductor (ITO/a-Si:H) contact, the bands in the a-Si:H side are raised in energy relative to those of ITO and the electric field at this junction decreases, therefore the charge carriers are able to cross the barrier without any obstacles, resulting in increase in $J_{ITO;sc}$ under the applied field. If we further increase the external voltage, the bands at the ITO semiconductor junction as well as a-Si:H and nc-Si:H interface approach to become flat and thus the carrier (electrons) from nc-Si:H layer (highly conducting) to a-Si:H (low conducting) could easily tunnel towards ITO. In this process some of the electrons get trapped in the bulk density of states of a-Si:H as well as the interface states between a-Si:H and nc-Si:H. This could be the reason behind the higher value of DOS in the superlattice structures as compared to single layer a-Si:H film which is estimated assuming no trapping of charge carriers at the interface.

The conjecture that the excess DOS in superlattice structures is due to the interface state between nc-Si:H and a-Si:H gets further support from the observed PPC in these superlattice structures

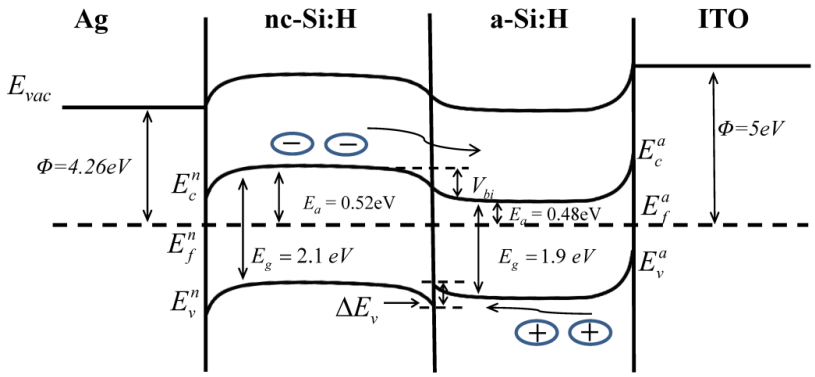

Figure 6.6: Schematic band diagram of Ag/nc-Si:H/a-Si:H/ITO superlattice structure. The value of bandgap and activation energies are obtained from transmission spectroscopy and conductivity measurements respectively. The electron affinity of Si is taken as 4.05eV.

[31] which has been understood in terms of carrier trapping at the interface states, PPC (%) is found to increase with increase in number of interface states in these superlattice structures as discussed in detail in Chapter 5. In case of SCLC measurements, the DOS for superlattice structures does not depend upon the number of layers in the given structure as these are calculated for a single pair of nc-Si:H/a-Si:H layers. Further these values are different than those for single layer a-Si:H films as no such interface states exist in case of single layer film. The results show that the existence of the interface states in these superlattice structures could be the reason behind the observed PPC as well as the higher DOS in these a-Si:H/nc-Si:H superlattice structures.

6.4 Conclusion

In this study, the DOS in HWCVD-deposited single layer a-Si:H and a-Si:H/nc-Si:H superlattice structures were determined from SCLC measurements carried out in sandwich geometry. The DOS of a-Si:H in superlattice structures was higher compared with that in single layer a-Si:H for the same shift in ΔE_{fn} . In single layer film, the charge injected from the metal to the

semiconductor were trapped in the DOS in the band gap, whereas for superlattice structures, the charge redistributed itself between the DOS in the band gap region and at the interface states between the different layers of superlattice structures. The higher DOS in superlattice structures could be attributed to interface states between a-Si:H and nc-Si:H, which may also change the local electric field at the junction under no-bias conditions. Carriers trapped at the interface states were also responsible for the observed PPC in these superlattice structures.

6.5 References

[1] K.H. Jun, K.S. Lim, Enhanced vertical photo-sensitivity in μc-Si:H/a-Si:H superlattices, Journal of Non-Crystalline Solids, 261 (2000) 268-272.

[2] V.L. Dalal, A. Madhavan, Alternative designs for nanocrystalline silicon solar cells, Journal of Non-Crystalline Solids, 354 (2008) 2403-2406.

[3] J. Dresner, Transistor having a superlattice, U. S Patent DOI (1987) 4,697,197

[4] C. Battaglia, J. Escarré, K. Söderström, L. Erni, L. Ding, G. Bugnon, A. Billet, M. Boccard, L. Barraud, S. De Wolf, F.-J. Haug, M. Despeisse, C. Ballif, Nanoimprint Lithography for High-Efficiency Thin-Film Silicon Solar Cells, Nano Letters, 11 (2011) 661-665.

[5] B. Curtin, R. Biswas, V. Dalal, Photonic crystal based back reflectors for light management and enhanced absorption in amorphous silicon solar cells, Applied Physics Letters, 95 (2009) 231102.

[6] O. Isabella, J. Krč, M. Zeman, Modulated surface textures for enhanced light trapping in thin-film silicon solar cells, Applied Physics Letters, 97 (2010) 101106.

[7] S. Pattnaik, N. Chakravarty, R. Biswas, V. Dalal, D. Slafer, Nano-photonic and nano-plasmonic enhancements in thin film silicon solar cells, Solar Energy Materials and Solar Cells, 129 (2014) 115-123.

[8] A. Madan, P.G. Le Comber, W.E. Spear, Investigation of the density of localized states in a-Si using the field effect technique, Journal of Non-Crystalline Solids, 20 (1976) 239-257.

[9] G.W. Neudeck, A.K. Malhotra, Field effect conductance modulation in vacuum−evaporated amorphous silicon films, Journal of Applied Physics, 46 (1975) 239-246.

[10] N.B. Goodman, H. Fritzsche, H. Ozaki, Determination of the density of states of a-Si:H using the field effect, Journal of Non-Crystalline Solids, 35–36, Part 1 (1980) 599-604.

[11] W.E. Spear, P.G. Le Comber, Investigation of the localised state distribution in amorphous Si films, Journal of Non-Crystalline Solids, 8-10 (1972) 727-738.

[12] T. Tiedje, C.R. Wronski, B. Abeles, J.M. Cebulka, Electron transport in hydrogenated amorphous silicon: drift mobility and junction capacitance, Solar Cells, 2 (1980) 301-318.

[13] M. Hirose, T. Suzuki, G.H. Döhler, Electronic density of states in discharge-produced amorphous silicon, Applied Physics Letters, 34 (1979) 234-236.

[14] I. Balberg, D.E. Carlson, Tunneling in Hydrogenated Amorphous Silicon, Physical Review Letters, 43 (1979) 58-61.

[15] Y.T. H. Okushi, S. Yamasaki, H. Oheda, K. Tanaka, Isothermal capacitance transient spectroscopy: its application to the study of gap sates of a-Si:H, J. Phys. Colloques, 42 (1981) C4-613-C614-616.

[16] J. Beichler, H. Mell, K. Weber, Density of gap-states in N-type and P-type A-Si:H, Journal of Non-Crystalline Solids, 59-60 (1983) 257-260.

[17] N.M. Johnson, Deep-level distributions in hydrogenated amorphous silicon, Journal of Non-Crystalline Solids, 59–60, Part 1 (1983) 265-268.

[18] D.V.L. J.D. Cohen, J.P. Harbison, A.M. Sergent, Study of light induced changes in a-Si:H by detailed computer modelling of admittance and DLTS, J. Phys. Colloques 42 (1981) C4-371-C374-374.

[19] E. Bhattacharya, S. Guha, K.V. Krishna, D.R. Bapat, Space-charge limited conduction in n+nn+ amorphous hydrogenated silicon films, Journal of Applied Physics, 53 (1982) 6285-6288.

[20] H.S. Soh, C. Lee, J. Jang, M.Y. Jung, S.S. Yoo, Determination of the density of states at the Fermi level of hydrogenated amorphous silicon in thin-film transistor structure by space charge limited current measurement, Applied Physics Letters, 63 (1993) 779-781.

[21] M. Lamri Zeggar, M. Messaoudi, M.S. Aida, N. Attaf, Gap states density measurement in copper oxide thin films, Materials Science in Semiconductor Processing, 45 (2016) 32-35.

[22] S.B. Husain, M. Zulfequar, M.A. Majeed Khan, M. Husain, Study of density of localized states in a-GaxSe100−x alloys using SCLC measurements, Current Applied Physics, 4 (2004) 445-451.

[23] H. Mahmoud Saad, S. El-Sayed, G. Ahmed Amin, K. Kamal Tahoon, M. Abd El-Rahman, Space charge limited currents and traps distribution in Ag–As–Te thin films glasses, Materials Science in Semiconductor Processing, 12 (2009) 193-197.

[24] A. Bozhko, M. Shupegin, T. Takagi, Space-charge-limited current in hydrogenated amorphous carbon films containing silicon and oxygen, Diamond and Related Materials, 11 (2002) 1753-1759.

[25] S. Guessasma, M. Chahdi, The Study of the density of localised gap states in amorphous silicon material using Space Charge Limited Currents technique, Materials Science in Semiconductor Processing, 7 (2004) 411-417.

[26] Z. Çaldıran, M. Şinoforoğlu, Ö. Metin, Ş. Aydoğan, K. Meral, Space charge limited current mechanism (SCLC) in the graphene oxide Fe_3O_4 nanocomposites/n-Si heterojunctions, Journal of Alloys and Compounds, 631 (2015) 261-265.

[27] C.R. Wronski, R.E. Daniel, Photoconductivity, trapping, and recombination in discharge-produced, hydrogenated amorphous silicon, Physical Review B, 23 (1981) 794-804.

[28] O. Hidetoshi, Y. Satoshi, Y. Toshihiko, M. Akihisa, O. Hideyo, T. Kazunobu, Gap States Distribution of Undoped a-Si: H Determined with Phase-Shift Analysis of the Modulated Photocurrent, Japanese Journal of Applied Physics, 21 (1982) L440.

[29] W.D. Boer, Determination of midgap density of states in a-Si:H using space charge limited current measurements, J. Phys. Colloques 42 (1981) C4-451-C454-454.

[30] A.L. S. Ashok, S.J. Fonash, , Evidence of space charge limited current in amorphous silicon schottky diodes, IEEE Electron Devices Lett. , 1 (1980) 200-202.

[31] A. Yadav, P. Agarwal, Persistent photoconductivity studies in a-Si:H/nc-Si:H thin film superlattices, Superlattices and Microstructures, 85 (2015) 776-783.

Chapter 7

Tunable visible photoluminescence in a-Si:H/nc-Si:H superlattices

Silicon is the firmly established material for semiconductor devices and circuits. There is great interest in integrating opto-electronic and micro-photonic functionalities into the silicon-based platform, which has faced challenges due to the indirect nature of the silicon band gap. For this reason allotropes of silicon and nano-structured Si have been widely investigated during the last few years, as it offer an enhancement in the optical properties compared to bulk Si [1-11], and a pathway to obtain a direct band gap. The modification of c-Si structure environment is expected to induce a more efficient luminescence than is found in indirect gap bulk c-Si, and also shift the emission from 1.1 eV into the desired visible region [6] [12, 13], a key goal in optoelectronics. Various methods have been employed to produce ultra-fine silicon nanocrystals such as low pressure chemical vapour deposition [14], laser ablation [15, 16], electrochemical anodization[5], rf-magnetron sputtering [6] [17], rf-PECVD [18], microwave CVD[12], gas phase synthesis[19] etc.

The synthesis of Si nanocrystals with controlled size and density was later introduced by synthesizing superlattice films of: amorphous silicon oxide (a-SiO)/SiO_2 [20],

nanocrystalline-Si (nc-Si)/SiO_2 [21], a-Si/SiO_2 [22], Si/SiO_2 [23] with varying stoichiometry followed by subsequent processing. In a-Si/SiO_2 superlattice structures, researchers have succeded in recrystallization of a-Si by annealing it at very high temperature of 1050 °C in an ambient environment in order to passivate the dangling bonds [24]. However, SiO_2 is generally not considered to be a good candidate for device application due to its large band offset with respect to silicon. A superlattice structure with lower band offset such as a-Si:H/nc-Si:H is desirable to increase carrier mobility [25]. Large photocurrent enhancement is reported in these a-Si:H/nc-Si:H superlattice structures [26]. The optical absorption enhancement, from photonic and plasmonic effects, has also been reported by several groups in the nano-structured a-Si:H and nc-Si:H thin films [27-29]. In addition to the studies on electrical transport properties in a-Si:H/nc-Si:H superlattice structures as discussed in the previous chapters, it is of great interest to study and tailor the optical properties of these superlattice structures by controlling the structural morphology.

In this chapter, we present our studies on tunable visible photoluminescence in a-Si:H/nc-Si:H superlattice structures without any post deposition processing such as annealing at high temperature, and find strong evidence of nanocrystal quantum size effects. The size of the nanocrystals could be easily tuned by varying the thickness of the nc-Si:H layers. We also observe long wavelength photoluminescence from interfacial states that leads to persistent photconductivity in these a-Si:H/nc-Si:H superlattice structures.

7.1 Measurement Details

Novel Si nanocrystals with controlled size were synthesized using nc-Si:H/a-Si:H superlattice structures. Superlattice structures with thin individual layers of nc-Si:H and a-Si:H were prepared using rf-PECVD. In these structures, the bottom and top layers were

retained to be nc-Si:H and total number of layers were kept as 7 (4 nc-Si:H and 3 a-Si:H layers). The thickness of a-Si:H layer was kept constant at 10 nm whereas, the thickness of nc-Si:H layer was varied from 5-30 nm. Another sample having 20 nm thick nc-Si:H layer with total number of layers as 11 (6 nc-Si:H and 5 a-Si:H layers) was also prepared to study the influence of the number of interface and the total thickness on photoluminescence. Figure 7.1 shows the schematic diagram of these superlattice structure. The a-Si:H and nc-Si:H thin films were prepared with the variation of hydrogen dilution [R] of silane while keeping all the other deposition parameters fixed. Hydrogen dilution [R] was varied from 55% to 96% for a-Si:H and nc-Si:H films respectively. The other deposition parameters for these films are mentioned in detail in Table 2.6 & 2.7 of Chapter 2. The deposition time for the desired thickness of individual layer was estimated from the deposition rate of corresponding single layer films.

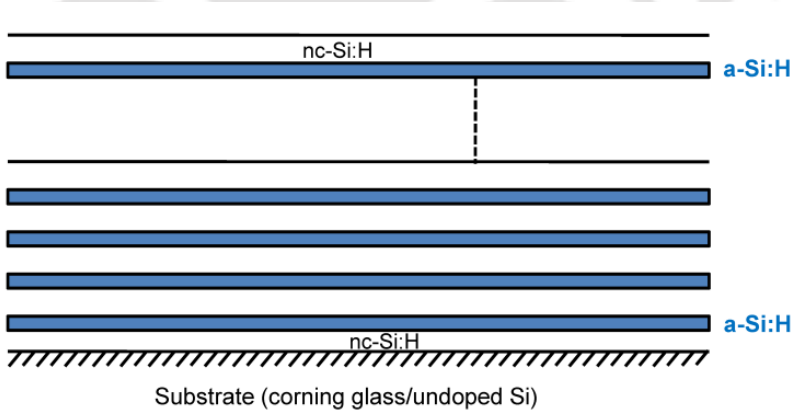

Figure 7.1: Schematic of a-Si:H/nc-Si:H superlattice structures (the thickness of nc-Si:H layer was varied in different samples).

X-ray diffraction (XRD) and transmission electron microscope (TEM) were used to examine the crystallographic orientation of single layer films. Further the samples were characterized by micro Raman spectroscopy for structural study. The band gap of single layer a-Si:H and

nc-Si:H were estimated using Tauc plot from UV-Vis–NIR transmission spectra and the thickness of films were measured using surface profilometer of single layer films. Electrical characterizations were done on these films using Ag paste as electrodes in coplaner geometry. Keithley 2450 source meter was used for electrical measurements and 100 W halogen lamp was used for illumination. A standard set-up was used for photoluminesence (PL) measurements with which PL spectra were recorded using a diode pumped solid state (DPSS) laser at an excitation wavelength of 405 nm and at laser power of 30 mW.

7.2 Results and Discussion

Figure 7.2 shows the XRD pattern of the single layer a-Si:H and nc-Si:H thin film recorded using CuKα radiation (λ= 1.54 Å) in the scanning range from 15º to 70º. XRD studies suggest that the films prepared at low [R] are amorphous in nature with broad peak around 28°, while nanocrystallinity develops for higher [R] as sharp peaks corresponding to (111), (220) and (311) planes of crystalline silicon appears. Figure 7.3 (a), shows the Raman spectra of single layer films prepared at different [R] at excitation wavelength of 488 nm. At low [R], broad peak centered at 480 cm^{-1} corresponds to the transverse optic mode (TO) of amorphous silicon whereas at higher [R], sharp peak near about 520 cm^{-1} corresponding to TO mode of phonon vibration of c-Si appears. Total crystalline volume fraction (X_c) and nanocrystalline volume fraction (X_{nc}) were calculated after deconvoluting the Raman spectra for nc-Si:H film, as shown in Fig 7.3 (b), into peaks corresponding to TO modes of a-Si:H (480 cm^{-1}), grain boundaries (504 cm^{-1}) and nc-Si (517 cm^{-1}) [30]. The values of X_c(%) and X_{nc}(%) were estimated using Eq. 2.2 & 2.3 (as mentioned in Chapter 2) and were found to be 63% and 46% respectively .

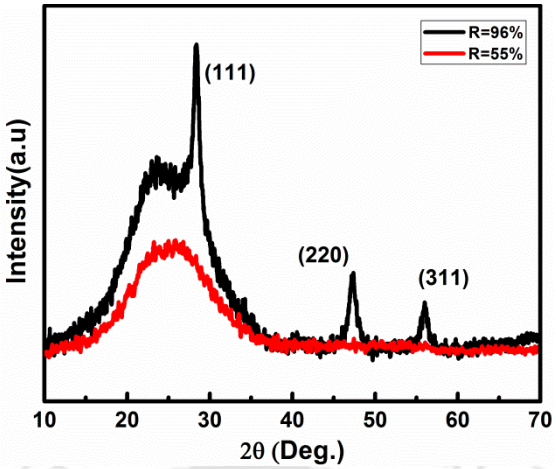

Figure 7.2: The XRD pattern of single layer a-Si:H and nc-Si:H thin films with different [R].

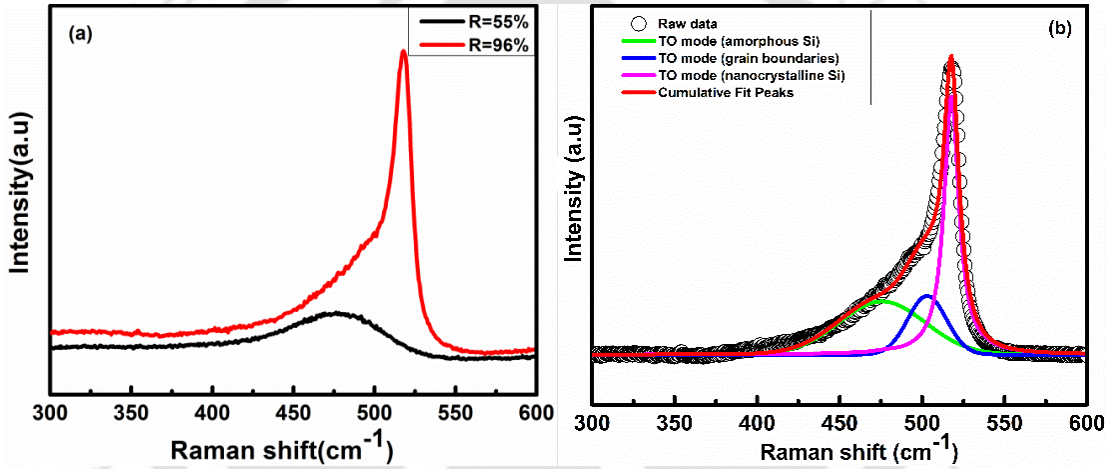

Figure 7.3: (a) Raman spectra of single layer a-Si:H and nc-Si:H thin films with different [R], (b) Deconvoluted Raman spectra of single layer of nc-Si:H prepared at [R]=96%.

Figure 7.4 (a) and 7.4 (b) show the selected area diffraction (SAD) pattern of single layer a-Si:H and nc-Si:H thin films respectively. The diffused ring confirms the amorphous nature at low [R] while at high [R], the appearance of bright spots on the sharp rings is an indication of the formation of nanocrystalline silicon as also observed in XRD. From the conductivity measurement at room temperature, it was observed that the films prepared at low [R] show high photo sensitivity of an order of 4 in magnitude, whereas, the films prepared at higher [R] show low photo sensitivity of ~1 order in magnitude which is the

characteristic features of amorphous and nanocrystalline silicon thin films [31]. The optical band gap was estimated from UV-Vis-NIR transmission spectra of thick single layer a-Si:H (110 nm) and nc-Si:H (95 nm) and was found to be 1.8 and 2.1 eV respectively.

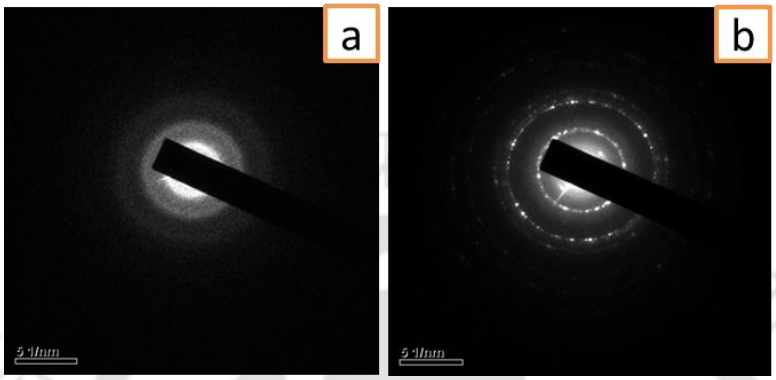

Figure 7.4: SAD pattern of (a) a-Si:H and (b) nc-Si:H single layer thin films.

The PL spectra (Fig. 7.5) of the superlattice films on both glass and silicon substrate were measured with an excitation wavelength of 405 nm. The PL spectra of the single layer a-Si:H (10 nm) and nc-Si:H (5 nm) thin films are shown in Fig. 7.6. No photoluminescence was observed for thin as well as thick single layer films of a-Si:H and nc-Si:H.

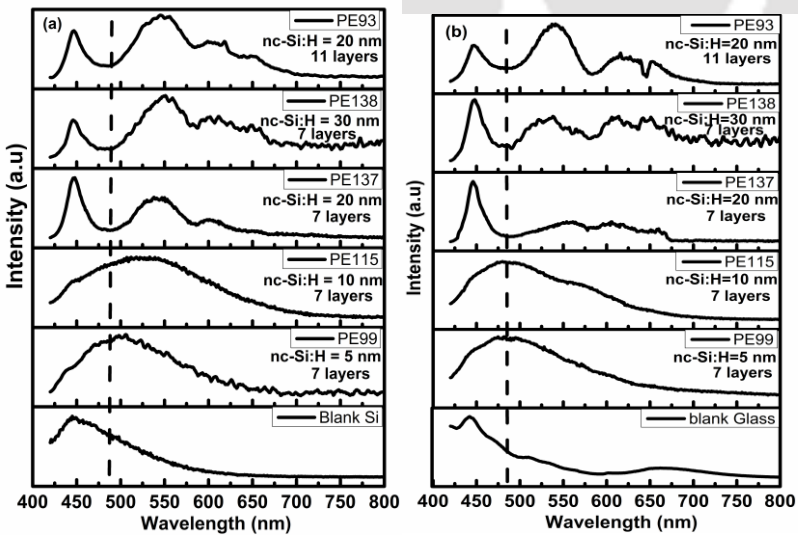

Figure 7.5: PL spectra of a-Si:H/nc-Si:H superlattice structures on (a) Silicon and (b) glass substrates

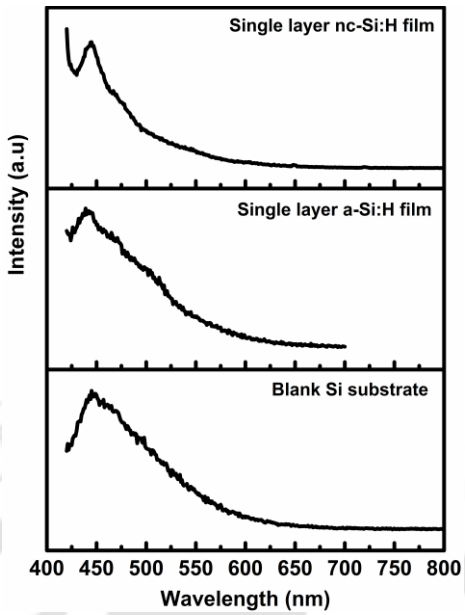

Figure 7.6: PL spectra of single layer a-Si:H and nc-Si:H thin films on silicon substrate and blank Si substrate

The PL emission spectra of superlattice strcutures (Fig. 7.5) is characterized by several broad and distinct peaks in the energy range (1.9-2.5 eV- between 410 and 700 nm). The PL peak at ~445 nm (2.78 eV), corresponding to the band gap of SiO_2, was observed for all the single layer films (Fig. 7.6), superlattice structures (Fig.7.5), as well as blank glass and silicon substrates, and is due to PL from a native SiO_2 layer on the surface.

A broad peak in PL spectra (between 500-550 nm) is observed for the superlattice structures with low thickness (5 and 10 nm) of nc-Si:H layers (Fig. 7.5). As the nc-Si:H layer thickness is increased to 20 nm and more, several distinguishable peaks in PL spectra were observed. Further the PL peaks were deconvoluted into a number of distinct peaks keeping the ~2.78 eV peak position fixed for these structures on both the substrates. The deconvoluted PL spectra for these structures on Si and glass substrates are shown in Fig 7.7-7.10. The values of peak position, maximum intensity and FWHM of these structures after deconvolution are listed in Table 7.1. The positions of the different peaks on the two substrates are nearly

same, suggesting the origin of PL peaks on Silicon and Glass substrates to be same, though the relative intensity of different peaks slightly vary on the two substrates. In all spectra, two peaks at around 2.25 eV and 2.06 eV are observed irrespective of the thickness of the nc-Si:H layer. In addition, a peak at 2.58-2.48 eV is observed for the structures with low thickness (5 and 10 nm) of nc-Si:H layer, whereas when the thickness of nc-Si:H layer is increased to 20 nm and above, the peak near 2.48 eV disappeared and an additional peak at ~1.90 eV is evolved. In all these structures, the highest energy peak is also the most intense.

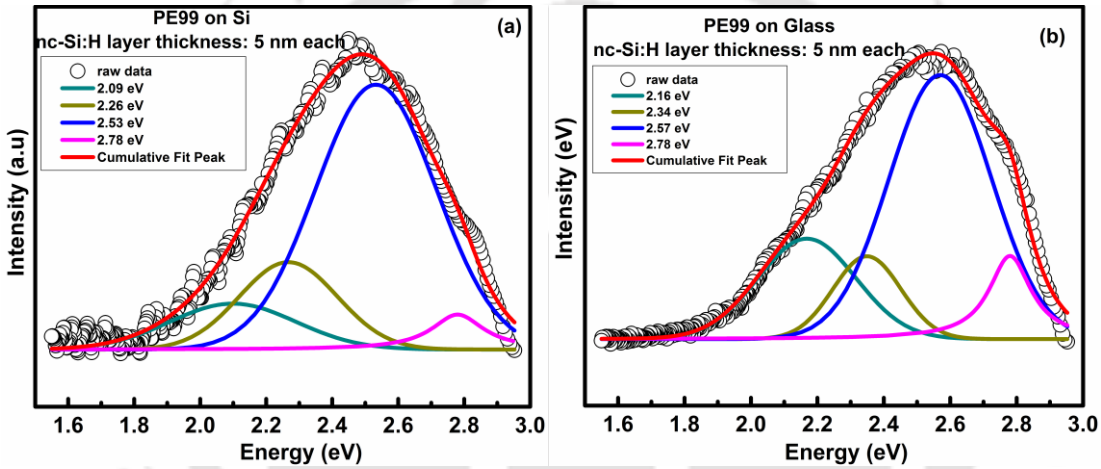

Figure 7.7: The de-convoluted PL spectra of superlattice structure films (nc-Si:H layer thickness of 5 nm) with peak position on (a) Si and (b) glass substrates.

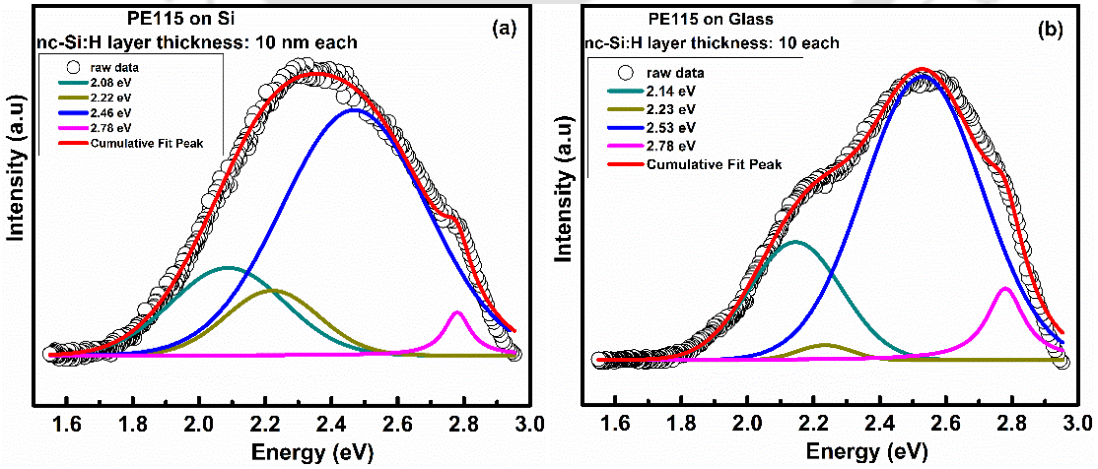

Figure 7.8: The de-convoluted PL spectra of superlattice structure films (nc-Si:H layer thickness of 10 nm) with peak position on (a) Si and (b) glass substrates.

These observation indicate that the photoluminscence in these structures might be arising due to confinement of Si nanocrystals in nc-Si:H layer between the adjacent a-Si:H layers; as the thickness of nc-Si:H layer is increased, the PL peak is evolved at lower energy or longer wavelength.

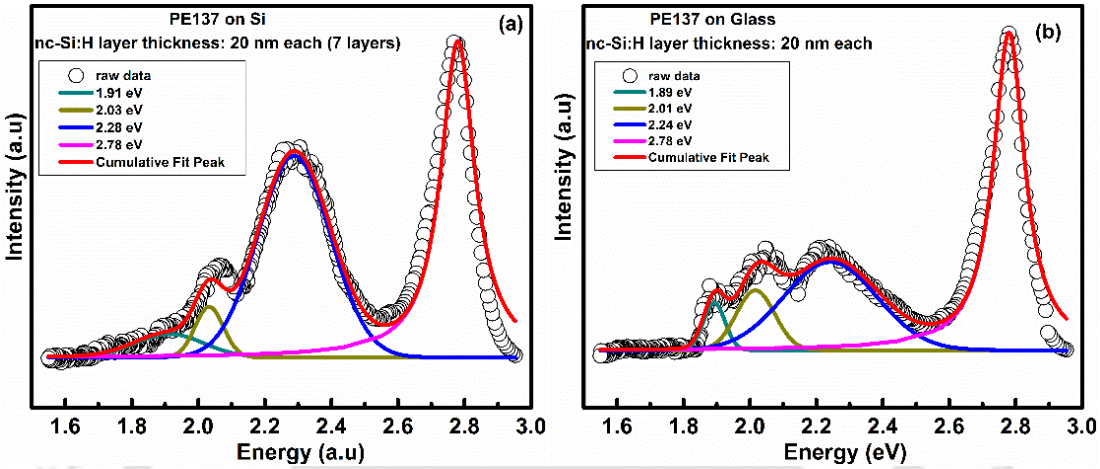

Figure 7.9: The de-convoluted PL spectra of superlattice structure films (nc-Si:H layer thickness of 20 nm) with peak position on (a) Si and (b) glass substrates.

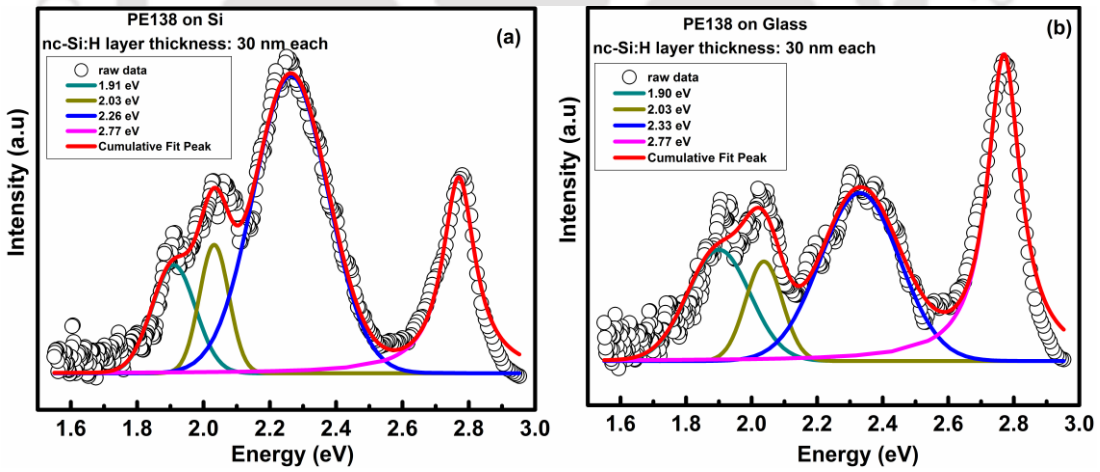

Figure 7.10: The de-convoluted PL spectra of superlattice structure films (nc-Si:H layer thickness of 30 nm) with peak position on (a) Si and (b) glass substrates.

A close examination of the position of the different peaks in PL spectra (Table 7.1) indicates that with the increase in nc-Si:H layer thickness, the most intense PL peak shifts towards

lower energy for both the substrates. To ascertain that the position of most intense peak depends upon the total thickness of the films or only on the nc-Si:H layer thickness, another superlattice structure was prepared with 20 nm thick nc-Si:H layer, however in this structure the number of layer had been increased from 7 to 11 layers (sample no. PE93 as mentioned in Table 2.7 of Chapter 2). Interestingly, the peak position in PL spectra for both 7 and 11 layers structures remain almost same on both substrates, irrespective of the total thickness of the structures.

Table 7.1: The PL peak position, FWHM and peak intensity of superlattice structures on glass and Si substrates.

Sample no.	**On Si substrate**			**On Glass substrate**		
	Peak Position (eV)	FWHM (eV)	Max ht. (a.u.)	Peak Position (eV)	FWHM (eV)	Max ht. (a.u.)
PE99 nc-Si:H=5 nm (7 layer)	2.78	0.19	153	2.78	0.15	11244
	2.53	0.43	1158	2.57	0.36	35718
	2.26	0.35	382	2.34	0.24	11206
	2.09	0.44	200	2.16	0.34	13583
PE115 nc-Si:H=10 nm (7 layer)	2.78	0.09	2145	2.78	0.13	8085
	2.46	0.51	12271	2.53	0.42	31969
	2.22	0.33	3243	2.23	0.19	1688
	2.08	0.40	4378	2.14	0.32	13319
PE137/PE93 nc-Si:H=20 nm (7 layers/11 layers)	2.78/2.78	0.12/0.13	15738/4649	2.78/2.78	0.11/0.19	13827/13445
	2.28/2.27	0.25/0.29	10019/6079	2.24/2.30	0.33/0.23	3837/23007
	2.03/2.03	0.10/0.09	2512/2094	2.01/2.01	0.13/0.10	2602/9718
	1.91/1.91	0.24/0.16	1161/1832	1.89/1.89	0.07/0.15	2059/6673
PE138 nc-Si:H=30 nm (7 layers)	2.77	0.11	537	2.77	0.12	694
	2.26	0.26	815	2.33	0.28	380
	2.03	0.10	352	2.03	0.13	225
	1.91	0.15	296	1.90	0.22	251

Nanocrystalline Si is composed of small crystallites of silicon embedded in an amorphous a-Si:H matrix [32, 33]. Thus by synthesizing nc-Si:H (thickness d nm)/a-Si:H superlattices with varying nc-Si:H thickness, we have the ability to tune the size of the nano-crystals. Since the direct imaging of the individual nano-crystals is difficult, therefore, the size of Si

nanocrystals was estimated from shift of the Raman peak w.r.t c-Si peak at 520 cm^{-1}(using Equ. as mentioned in section of chapter 2) for the single layer nc-Si:H films of different (5-30 nm) thicknesses. The size of the nanocrystallites estimated from Raman shift are found to be 3.35, 4.44, 6.26 and 8.88 nm for nc-Si:H layer thickness 5, 10, 20 and 30 nm respectively. There is a systematic increase in size of nanocrystallites with increase in thickness of nc-Si:H layer in these structures. For quantum size effects to dominate, the energy of the PL peak should vary as d^{-2} or the wavelength as d^2 [34]. We plot the wavelength corresponding to the maximum intensity peak in PL spectra as a function of d^2 (Fig. 7.11), where d is the size of Si nanocrystallites as estimated from Raman spectra. We observe that for these superlattice structures, on both glass as well as c-Si substrates, wavelength λ, of maximum energy peaks, varies nearly linearly with d^2 for the low nc-Si:H layer ($\leq$20 nm) thickness (Fig 7.11). However, as the nc-Si:H layer thickness is increased beyond 20 nm, the PL wavelength does not follow the linear relation. This observation suggests that for the low nc-Si:H layer thickness (5-20 nm) the origin of the peak at ~500 nm is likely to be due to the quantum confinement of the electronic wavefunctions within the nanocrystal of diameter~d. These observations are also supported by a blue shift in absorption edge of single layers of a-Si:H and nc-Si:H films when the thickness is reduced (Fig 7.12). The results in the present experiments thus are consistent with quantum confinement effects for the low thickness of nc-Si:H layers. However, for the higher nc-Si:H layer thickness, λ deviates from the linear relation with d^2. Therefore, the origin of emission peaks at lower energy (higher wavelength) for thick nc-Si:H layer need to be studied further. Since both single layer a-Si:H and nc-Si:H, thick as well as thin films do not show any PL at room temperature though it is observed for superlattice structures, it is interesting to

consider if the interfaces between the sublayers of a-Si:H and nc-Si:H in these superlattice structures play any role on the observed photoluminescence.

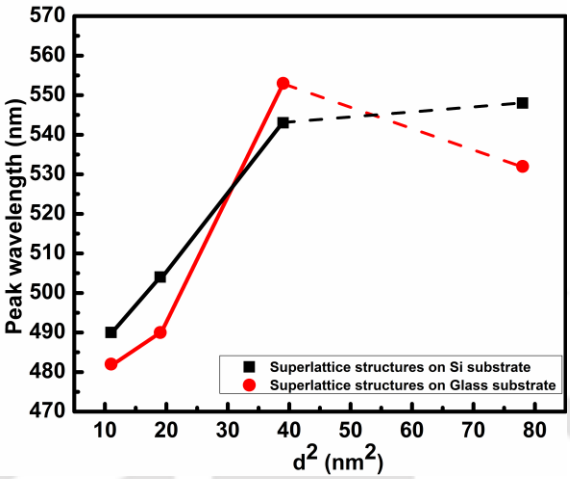

Figure 7.11: PL peak position λ Vs d^2 on silicon and corning glass substrate.

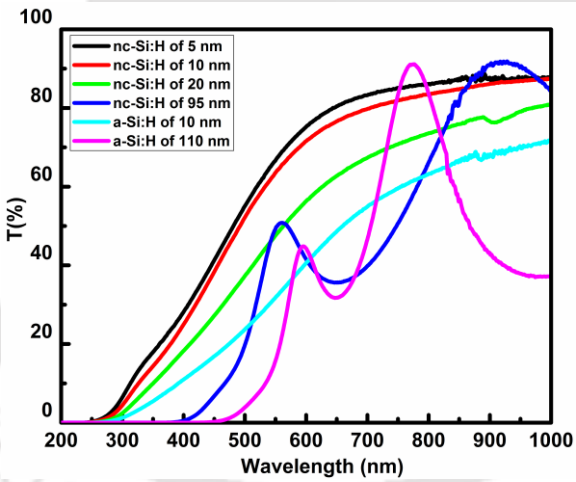

Figure 7.12: UV-Vis-NIR transmission spectra of single layer a-Si:H and nc-Si:H thin films.

In these a-Si:H/nc-Si:H superlattice structures, the different bandgaps of a-Si:H and nc-Si:H results in band bending at the interface and therefore the optoelectronic properties of a-Si:H/nc-Si:H superlattice structures are quite different than that of single layer a-Si:H and nc-Si:H thin films; the a-Si:H/nc-Si:H superlattice structures have shown persistent photoconductivity (PPC) [35], whereas single layer films do not show any PPC as discussed

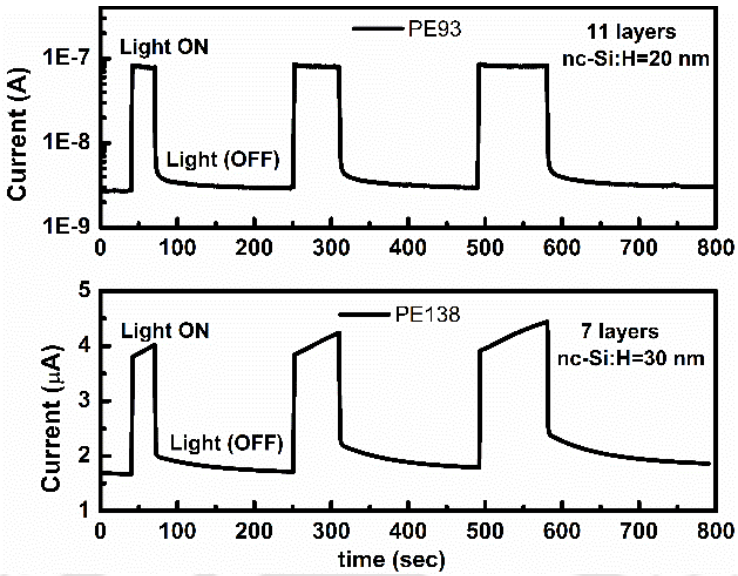

Figure 7.13: Rise and decay of the photo current in a-Si:H/nc-Si:H superlattice with nc-Si:H layer thickness of 30 nm (7 layers) and 20 nm (11 layers) structures (also shown in chapter 5).

in detail in Chapter 5. As discussed in Chapter 5 (Fig 5.9), PPC has been observed in these a-Si:H/nc-Si:H superlattice structures when the nc-Si layer thickness is 20 nm or more (Fig. 7.13), whereas structures with thin nc-Si layer (<20 nm) do not show any PPC. The origin of PPC in these superlattice structures has been understood as trapping of the charge carriers at the interfaces between the sublayers of a-Si:H and nc-Si:H films. Interestingly, the low energy PL peaks, at 1.91 eV, is also observed for these structures only, which is in between the bandgaps of a-Si:H (1.8 eV) and nc-Si:H (2.1 eV) as measured on thick films. These observations suggest that the observed photoluminescence at the low energy range (for higher nc-Si:H (≥20 nm) layer thickness) in these superlattice structures; could be due to energy released during the recombination of the trapped carriers at the interface which also give rise to PPC. When nc-Si:H layer is less, the photogenrated carriers are able to tunnel through the band bending region and are not trapped in the interface states; hence these structures neither show a PPC nor any PL signature is observed at low energies.

7.3 Conclusion

We have fabricated nc-Si:H/a-Si:H superlattice structures with varying thickness (d) of the nanocrystalline Si layers. Since nc-Si:H consists of nanocrystals of Si embedded in an amorphous matrix, the size of the nanocrystals could be tuned by varying the thickness of the nc-Si:H layers. This is confirmed by photoluminescence measurements which reveal a strong feature at shorter wavelength (~500-550 nm) in which the PL wavelength scales as the square of the size of Si nanocrystals; d^2, for small nc-layer thickness of 5-20 nm, strongly indicating quantum size effects.

As the nc-layer thickness increased beyond 20 nm, additional low energy peak (1.9 eV) in PL spectra is observed. This low energy emission seems to be due to the radiative recombination via the interface states in between the sublayers of a-Si:H and nc-Si:H in these superlattice structures, which were also found to be responsible for the observed persistent photconductivity in these structures. The superlattices of nanocrystalline and amorphous materials offer a unique pathway for synthesizing nanocrystals with controlled sizes and photonic signatures.

7.4 References

[1] W.L. Wilson, P.F. Szajowski, L.E. Brus, Quantum Confinement in Size-Selected, Surface-Oxidized Silicon Nanocrystals, Science (New York, N.Y.), 262 (1993) 1242-1244.

[2] V. Lehmann, U. Gösele, Porous silicon formation: A quantum wire effect, Applied Physics Letters, 58 (1991) 856-858.

[3] O. Yukio, T. Keiji, T. Fumitaka, M. Hiroaki, K. Kenji, Visible Photoluminescence from Si Microcrystals Embedded in SiO_2 Glass Films, Japanese Journal of Applied Physics, 31 (1992) L365.

[4] S. Furukawa, N. Matsumoto, Effects of polysilane formation on the optical and electrical properties of binary Si:H alloys, Physical Review B, 31 (1985) 2114-2120.

[5] L.T. Canham, Silicon quantum wire array fabrication by electrochemical and chemical dissolution of wafers, Applied Physics Letters, 57 (1990) 1046-1048.

[6] S. Furukawa, T. Miyasato, Quantum size effects on the optical band gap of microcrystalline Si:H, Physical Review B, 38 (1988) 5726-5729.

[7] D.C. Hannah, J. Yang, N.J. Kramer, G.C. Schatz, U.R. Kortshagen, R.D. Schaller, Ultrafast Photoluminescence in Quantum-Confined Silicon Nanocrystals Arises from an Amorphous Surface Layer, ACS Photonics, 1 (2014) 960-967.

[8] E. Steveler, H. Rinnert, M. Vergnat, Low-temperature photoluminescence properties of Nd-doped silicon oxide thin films containing silicon nanocrystals, Journal of Luminescence, 183 (2017) 311-314.

[9] S.F. Ahmed, D. Banerjee, M.K. Mitra, K.K. Chattopadhyay, Visible photoluminescence from silicon-incorporated diamond like carbon films synthesized via direct current PECVD technique, Journal of Luminescence, 131 (2011) 2352-2358.

[10] A. Momeni, M.H. Mahdieh, Photoluminescence analysis of colloidal silicon nanoparticles in ethanol produced by double-pulse ns laser ablation, Journal of Luminescence, 176 (2016) 136-143.

[11] C.-H. Cho, J.-W. Kang, I.-K. Park, S.-J. Park, Enhanced quantum confinement in tensile-strained silicon nanocrystals embedded in silicon nitride, Current Applied Physics, 17 (2017) 1616-1621.

[12] H. Takagi, H. Ogawa, Y. Yamazaki, A. Ishizaki, T. Nakagiri, Quantum size effects on photoluminescence in ultrafine Si particles, Applied Physics Letters, 56 (1990) 2379-2380.

[13] J.H. Shim, S. Im, N.H. Cho, Nanostructural features of ncSiH thin films prepared by PECVD, Applied Surface Science, 234 (2004) 268-273.

[14] A. Nakajima, Y. Sugita, K. Kawamura, H. Tomita, N. Yokoyama, Microstructure and optical absorption properties of Si nanocrystals fabricated with low-pressure chemical-vapor deposition, Journal of Applied Physics, 80 (1996) 4006-4011.

[15] L.N. Dinh, L.L. Chase, M. Balooch, L.J. Terminello, F. Wooten, Photoluminescence of oxidized silicon nanoclusters deposited on the basal plane of graphite, Applied Physics Letters, 65 (1994) 3111-3113.

[16] E. Werwa, A.A. Seraphin, L.A. Chiu, C. Zhou, K.D. Kolenbrander, Synthesis and processing of silicon nanocrystallites using a pulsed laser ablation supersonic expansion method, Applied Physics Letters, 64 (1994) 1821-1823.

[17] Y.-H. So, S. Huang, G. Conibeer, M.A. Green, Formation and photoluminescence of Si nanocrystals in controlled multilayer structure comprising of Si-rich nitride and ultrathin silicon nitride barrier layers, Thin Solid Films, 519 (2011) 5408-5412.

[18] F. Iacona, G. Franzò, C. Spinella, Correlation between luminescence and structural properties of Si nanocrystals, Journal of Applied Physics, 87 (2000) 1295-1303.

[19] D. Zhang, R.M. Kolbas, P.D. Milewski, D.J. Lichtenwalner, A.I. Kingon, J.M. Zavada, Light emission from thermally oxidized silicon nanoparticles, Applied Physics Letters, 65 (1994) 2684-2686.

[20] M. Zacharias, J. Heitmann, R. Scholz, U. Kahler, M. Schmidt, J. Bläsing, Size-controlled highly luminescent silicon nanocrystals: A SiO/SiO_2 superlattice approach, Applied Physics Letters, 80 (2002) 661-663.

[21] P. Photopoulos, A.G. Nassiopoulou, D.N. Kouvatsos, A. Travlos, Photo- and electroluminescence from nanocrystalline silicon single and multilayer structures, Materials Science and Engineering: B, 69 (2000) 345-349.

[22] L. Tsybeskov, K.D. Hirschman, S.P. Duttagupta, M. Zacharias, P.M. Fauchet, J.P. McCaffrey, D.J. Lockwood, Nanocrystalline-silicon superlattice produced by controlled recrystallization, Applied Physics Letters, 72 (1998) 43-45.

[23] D.J. Lockwood, Z.H. Lu, J.M. Baribeau, Quantum Confined Luminescence in Si/SiO_2 Superlattices, Physical Review Letters, 76 (1996) 539-541.

[24] M. Zacharias, L. Tsybeskov, K.D. Hirschman, P.M. Fauchet, J. Bläsing, P. Kohlert, P. Veit, Nanocrystalline silicon superlattices: fabrication and characterization, Journal of Non-Crystalline Solids, 227 (1998) 1132-1136.

[25] J.Dresner, Transistor having a superlattice, U.S Patent, 4, 697,197 (1987).

[26] S. Pattnaik, N. Chakravarty, R. Biswas, V. Dalal, D. Slafer, Nano-photonic and nano-plasmonic enhancements in thin film silicon solar cells, Solar Energy Materials and Solar Cells, 129 (2014) 115-123.

[27] O. Isabella, J. Krč, M. Zeman, Modulated surface textures for enhanced light trapping in thin-film silicon solar cells, Applied Physics Letters, 97 (2010) 101106.

[28] B. Curtin, R. Biswas, V. Dalal, Photonic crystal based back reflectors for light management and enhanced absorption in amorphous silicon solar cells, Applied Physics Letters, 95 (2009) 231102.

[29] C. Battaglia, J. Escarré, K. Söderström, L. Erni, L. Ding, G. Bugnon, A. Billet, M. Boccard, L. Barraud, S. De Wolf, F.-J. Haug, M. Despeisse, C. Ballif, Nanoimprint Lithography for High-Efficiency Thin-Film Silicon Solar Cells, Nano Letters, 11 (2011) 661-665.

[30] S. Veprek, F.A. Sarott, Z. Iqbal, Effect of grain boundaries on the Raman spectra, optical absorption, and elastic light scattering in nanometer-sized crystalline silicon, Physical Review B, 36 (1987) 3344-3350.

[31] P. Gogoi, H.S. Jha, P. Agarwal, Variation of microstructure and transport properties with filament temperature of HWCVD prepared silicon thin films, Thin Solid Films, 519 (2011) 4506-4510.

[32] B.C. Pan, R. Biswas, Structure and simulation of hydrogenated nanocrystalline silicon, Journal of Applied Physics, 96 (2004) 6247-6252.

[33] B.C. Pan, R. Biswas, Simulation of hydrogen evolution from nano-crystalline silicon, Journal of Non-Crystalline Solids, 333 (2004) 44-47.

[34] L.E. Brus, Electron–electron and electron-hole interactions in small semiconductor crystallites: The size dependence of the lowest excited electronic state, The Journal of Chemical Physics, 80 (1984) 4403-4409.

[35] A. Yadav, P. Agarwal, Persistent photoconductivity studies in a-Si:H/nc-Si:H thin film superlattices, Superlattices and Microstructures, 85 (2015) 776-783.

Chapter 8

Summary, Conclusion and Future Scope

This chapter summarizes the work reported in the present thesis on the growth and properties of a-Si:H, nc-Si:H and a-Si:H/nc-Si:H superlattice structures prepared using both rf-PECVD and HWCVD techniques. During the thesis work, four different series of samples were prepared by varying one deposition parameter at a time, while keeping all the other deposition parameter constant. Si thin films were prepared with the variation of H_2 dilution of SiH_4, rf power, substrate temperature. From the optimized deposition parameter using both the techniques, a-Si:H/nc-Si:H superlattice structures were fabricated. The motivation of the present thesis work was to study the role of the interface states in a-Si:H/nc-Si:H superlattice structures on the optoelectronic properties of these structures. Keeping that in mind, *IV* measurements were conducted in both, coplanar as well as transverse, geometries as the electrical transport in these structures is anisotropic. Room temperature persistent photoconductivity (PPC) in coplaner geometry has been observed in these a-Si:H/nc-Si:H superlattice structures. Whereas, transverse geometry has been used for the estimation of density of localised states (DOS) in single as well as superlattice structures of a-Si:H and nc-Si:H thin films using space charge current limited (SCLC) measurements. Fabrication of these superlattice structures also helped in controlling the size of Si nanocrystallists in

amorphous matrix, which resulted in visible photoluminescence at room temperature in these superlattice structures without any post deposition processing. Laser induced selective crystallization of amorphous silicon thin films were also studied using Raman spectroscopy.

Our investigations and studies resulted in the following conclusions:

- Silicon thin films ranging from amorphous to nanocrystalline can be prepared with the variation in deposition parameters using both HWCVD and rf-PECVD techniques.
- High H_2 dilution of Silane during catalytic dissociation of Silane in HWCVD technique results in the formation of nc-Si whereas low H_2 dilution results in the formation of a-Si thin films.
- In order to obtain nanocrystalline silicon films using rf-PECVD techniques, high rf-power ($\geq$ 60W) with high H_2 dilution ($\geq$ 95%) of SiH_4 is required, whereas the films prepared at low H_2 dilution and low rf-power are all amorphous in nature.
- Phase transition from amorphous to nanocrystalline silicon can be achieved by exposure to high intensity laser radiation. The size of nanocrystallites and the extent of crystallization depends upon the power density of laser as well as the energy of the incident photons. With the increase in laser power density, the crystallinity is induced in all amorphous silicon thin films irrespective of deposition parameters. Low energy (632.8nm) beam requires high power density to achieve the same crystalline volume fraction as compared to high energy (488nm) laser beam. The area of the films which was not exposed to high laser power intensity remained amorphous in nature.
- The exposure to high intensity laser seems to be quite convenient method to selectively induce a microstructural change in Si thin films for device applications.

- The PPC studies across single and (a-Si/nc-Si:H) superlattice structures confirm the presence of interface states in between the sub layers of a-Si:H and nc-Si:H thin film in these superlattice structures. Carriers trapped at these interfaces states and/or the separations of carriers due to band bending are likely to be responsible for observed slow exponential decay of the photocurrent (PPC) in the these superlattice structures.

- The presence of these interface in the superlattice structures also resulted in higher DOS (~10^{18} $eV^{-1}cm^{-3}$) as compared to single layer a-Si:H (~10^{17} $eV^{-1}cm^{-3}$) thin films for the same shift in ΔE_{fn}.

- The *IV* measurements in both coplanar and transverse geometry confirms the presence of interface states in a-Si/nc-Si:H superlattice structures which play a major role in tuning the optoelectronic properties of these superlattice structures.

- The observed room temperature visible photoluminescence (at higher energy~2.5 eV) in these a-Si:H/nc-Si:H superlattice structures for the thin nc-Si layer (5-20 nm) show the confinement of Si nanocrystallites in between the thin layer of a-Si:H (10 nm) film; the evidence of quantum confinement effect. The photoluminescence peak at lower energy (~1.9 eV) is attributed to the radiative recombination of charge carriers via interface states in between the sub layers of a-Si and nc-Si in these superlattice structures.

- Nanocrystalline-amorphous superlattices offer a unique pathway for synthesizing nanocrystals with controlled sizes and photonic signatures.

8.1 Scope for Future work

Some of the future research scopes based on the present thesis work are as follows:

- Though, we are able to fabricate the a-Si:H/nc-Si:H superlattice structures successfully using both the techniques (HWCVD and rf-PECVD), which show interesting phenomenon such as PPC and visible photoluminescence at room temperature without any post deposition processing. The presence of these interface states in between the sub layers of a-Si:H and nc-Si:H can deteriorate the device performance. Therefore, more tuning on the morphology and structure need to be done in order to have clean interfaces which may results in improvement in device performance.
- It has been reported that a few seconds exposure to hydrogen plasma results in reduction of interface or defect states between different layers in a-Si:H based thin films (n-i-p and p-i-n) and heterojunction solar cells and makes a clean junction. It will be interesting to see the influence of hydrogen plasma treatment on the optoelectronic properties of these superlattice structures.

- The growth model of nanocrystalline silicon is very unique. The grains tend to grow into conical fashion and after certain thickness leads to the formation of grain boundaries which act as recombination center for single junction solar cells. Thus the prevention of the formation of grain boundaries is critical in the process of enhancing the efficiency of the solar cell. These a-Si:H/nc-Si:H superlattice structures may help in the reduction of this effect by restricting the grain growth to certain thickness using the thin layer of a-Si:H in between nc-Si films. These superlattice structures with tunable optoelectronic properties could be very useful for various device applications.

LIST OF PUBLICATIONS

Referred Journals/Conference Proceedings

1. **Asha Yadav** and Pratima Agarwal**, "**Persistent photoconductivity studies in a-Si:H/nc-Si:H thin film superlattices", *Superlattices and Microstructures, 85(2015) 776.*
2. **Asha Yadav** and Pratima Agarwal**, "**Density of states measurements in a-Si:H and a-Si:H/nc-Si:H multilayer structures prepared by HWCVD technique", *Material Science and Semiconductor Processing, 61(2017)5-10.*
3. **Asha Yadav** and Pratima Agarwal, "Laser Induced Selective Crystallization of Amorphous Silicon Thin Film for Device Applications*", Materialstoday PROCEEDINGS 4(2017)12722-12725.*
4. **Asha Yadav**, Pilik Basumatary and Pratima Agarwal, "Growth of a-Si:H and nc-Si:H thin films at high deposition rate by HWCVD technique". *(accepted in Springer Proc.).*
5. **Asha Yadav**, Juhi Kumari and Pratima Agarwal, "Role of interface states on electron transport in a-Si:H/nc-Si:H multilayer structures". (*accepted in AIP Conf. Proc.)*
6. **Asha Yadav,** Pratima Agarwal and Rana Biswas, "Quantum size effects and tunable visible photoluminescence in a-Si:H/nc-Si:H superlattices". *(under preparation)*

Papers presented in conferences (National/International)

1. **Asha Yadav**, Mukesh Singh and Pratima Agarwal, "a-Si:H/nc-Si:H thin film super lattice by Hot Wire Chemical Vapor Deposition", *International conference on Recent Advances in Nanoscience and Technology'2014 (ICRANN 2014), Jawaharlal Nehru University, New Delhi, 15-16th Dec 2014* .

2. **Asha Yadav**, Mukesh Singh and Pratima Agarwal, "Influence of hydrogen dilution on structural, electrical and optical properties of silicon thin films by HWCVD technique", *National Conference on transport properties in low dimension system'2014* (*TransLES 2014), IASST Guwahati, 11-13th Dec 2014.*
3. **Asha Yadav** and Pratima Agarwal, "Optoelectronic properties of silicon thin films for solar cell application: Influence of hydrogen dilution", *Frontier Energy Research with Industry Academia Partnership'2015 (FERIAP 2015), Centre for Energy, IIT Guwahati, 21-22nd March 2015.*
4. **Asha Yadav** and Pratima Agarwal, "Persistent photoconductivity studies in a-Si:H/nc-Si:H thin films super lattice", *International Conference on Amorphous and Nanocrystalline Semiconductors'2015 (ICANS26 2015), Aachen, Germany, 13-18thSep 2015.*
5. **Asha Yadav,** Venkanna Kanneboina and Pratima Agarwal, "Comparative studies of microstructure of silicon thin films by Raman spectroscopy and electrical transport measurements", *International Workshop on the Physics of Semiconductor Devices'2015 (IWPSD 2015), IISc Bangalore, 7-10th Dec 2015.*
6. **Asha Yadav**, Pilik Basumatary and Pratima Agarwal, "Research Activities in solar energy lab", *Research Conclave'16, IIT Guwahati, 18-20th March 2016.* **(Selected for best poster award)**
7. **Asha Yadav** and Pratima Agarwal, **"**Visible Photoluminescence in nc-Si:H/a-Si:H superlattice structures prepared by rf-PECVD technique", *National Conference on Recent Advances in Nanoscience and Nanotechnology'2016 (NCRANNT 2016), NEHU Shillong, 8-9th Sep 2016.*

8. **Asha Yadav** and Pratima Agarwal, "Laser Induced Selective Crystallization of Amorphous Silicon Thin Film for Device Applications", *International Conference on Solar Energy Photovoltaic'2016 (ICSEP 2016), KIIT Bhubaneswar, 17-19th Dec 2016.*
9. **Asha Yadav**, Pilik Basumatary and Pratima Agarwal, "Growth of a-Si:H and nc-Si:H thin films at high deposition rate by HWCVD technique ", *International Conference on Energy Options for Tomorrow: Technology to Sustainability'2017 (ICEOT 2017), The Neotia University, Kolkata, 17-19th April'2017.* **(Selected for best poster award)**
10. **Asha Yadav** and Pratima Agarwal, "Influence of Laser intensity on microstructure of Si thin films in Laser Raman scattering studies", *International Conference on Sophisticated Instruments in Modern Research'2017 (ICSIMR 2017), CIF, IIT Guwahati, Guwahati, 30th June-1st July'2017.*
11. **Asha Yadav** and Pratima Agarwal, "Persistent photoconductivity and space charge limited conduction in a-Si:H/nc-Si:H: Role of interface states", *International Conference on Thin Films'2017 (ICTF 2017), NPL, New Delhi, 14th-17th Nov, 2017.* **(Selected for best oral presentation award)**
12. **Asha Yadav**, Juhi Kumari and Pratima Agarwal, "Role of interface states on electron transport in a-Si:H/nc-Si:H multilayer structures", *International Conference on Condensed Matter and Applied Physics'2017 (ICC 2017), Govt. Engineering Collage, Bikaner, Rajasthan, 24th -25th Nov, 2017.*
13. **Asha Yadav,** Pratima Agarwal and Rana Biswas, "Tunable visible photoluminescence in a-Si:H/nc-Si:H superlattice structures", *National Workshop on FLUORESCENCE and RAMAN spectroscopy'2017 (FCS 2017), Dept. of Biotechnology, IIT Guwahati, 17-21st Dec, 2017.*

14. **Asha Yadav,** Pratima Agarwal and Rana Biswas, "Quantum size effects and tunable visible photoluminescence in a-Si:H/nc-Si:H superlattices", *Research Conclave'2018, IIT Guwahati, 8-11th March, 2018*. **(Selected for best poster award)**